UNIVERSITÀ
DEGLI STUDI
DI BRESCIA

UNIVERSITÀ DEGLI STUDI DI BRESCIA

DOTTORATO DI RICERCA IN INGEGNERIA
DELL'INFORMAZIONE

IN COTUTELA CON L'UNIVERSITÉ DE LIMOGES

Nonlinear Propagation in Multimode Optical Fiber Amplifiers

Dottorando: Mesay Addisu Jima

Tutor: Prof. Daniele Modotto

Relatore: Prof. Stefan Wabnitz

Stefan Wabnitz

Directeur de thèse: Dr. Vincent Couderc

Correlatrice: Prof. Annamaria Cucinotta

Annamaria Cucinotta

Coordinatore: Prof. Costantino De Angelis

XXXIII ciclo

Settore Scientifico Disciplinare: ING-INF/02

UNIVERSITÀ DEGLI STUDI DI BRESCIA

Abstract

Department of Information Engineering

Doctor of Philosophy

Nonlinear Propagation in Multimode Optical Fiber Amplifiers

by Mesay Addisu

The current long-haul transmission and worldwide complex interconnection of network infrastructure is based on single mode optical fiber which transports information in the form of light pulses. Single mode fibers have low attenuation and dispersion rate as all energy is confined to a single mode and no energy is lost into the cladding. As a result, single mode fibre is suitable for long distance transmission whereas multimode fibre, is mainly used for short distance communication. In addition, single mode fiber delivers diffraction limited high beam quality, guides only Gaussian like field distributions and allows high coupling efficiency. However, due to its core diameter size single mode fiber could not satisfy the future huge communication bandwidth demand, and it is not suitable for very high power fiber amplifiers and lasers.

Multimode optical fibers are designed to carry several modes, due to their large core radius. In principle, graded index active multimode fibers could be used for high power fiber amplifiers and fiber lasers. In addition, ytterbium doped multimode fibers are used to overcome the current bandwidth deficit of single mode fibers, through the techniques of spatial mode division multiplexing. Nowadays, high beam quality fiber amplifiers and lasers are required for different applications. However, multimode interferences that result in degradation of beam quality are the main problem for developing high power fiber lasers and fiber amplifiers. So, the question is how to overcome these constraints and use multimode fibers (step-index or graded-index) for these and other applications. The most feasible approach is to convert the Kerr nonlinearity from being a problem to an opportunity for beam cleaning. We performed a numerical study by solving coupled mode equations to investigate this phenomena further. By increasing the input signal power, we observed the transfer of energy from the high order modes to the fundamental mode, due to nonlinear and non-uniform gain coupling along the course of propagation. As a result, the fundamental mode experienced higher gain due to the exchange of power with the other high order modes, and beam cleaning is demonstrated.

Furthermore, to explore the nonlinear propagation in doped multimode fibers, we implemented a 3D NLSE in the presence of saturated gain, Kerr nonlinearity and disorder. Our numerical simulations reveal that by increasing the input signal power, the speckled beam reshapes itself after a certain fiber distance, into a clean beam close to single mode operation due to the laser gain and Kerr nonlinearity. The spatial beam self-cleaning phenomenon is further confirmed by examining the beam width at the end of the fiber length, which has reduced diameter than at the beginning of the fiber. Analysis of our results show that numerical simulations agree well with preliminary experimental results.

Sommario

L'attuale trasmissione a lungo raggio e la complessa interconnessione mondiale dell'infrastruttura di rete si basa su fibra ottica monomodale che trasporta le informazioni sotto forma di impulsi luminosi. Le fibre monomodali hanno un basso coefficiente di attenuazione e la loro dispersione è contenuta poiché tutta l'energia è confinata in un unico modo. Di conseguenza, la fibra monomodale è adatta per la trasmissione a lunga distanza mentre la fibra multimodale viene utilizzata principalmente per la comunicazione a breve distanza. Inoltre, la fibra monomodale fornisce un'elevata qualità del fascio in uscita la cui distribuzione di campo trasverso è di tipo gaussiano. Tuttavia, la fibra monomodale non è in grado di soddisfare l'enorme domanda futura di larghezza di banda di comunicazione e non è adatta per amplificatori e laser in fibra ad altissima potenza.

Le fibre ottiche multimodali sono progettate per supportare la propagazione di un larghissimo numero di modi, grazie all'ampio raggio del nucleo. In linea di principio, le fibre multimodali attive con un profilo trasverso dell'indice di rifrazione di tipo parabolico (graded-index), grazie alla loro bassa dispersione intermodale, potrebbero essere utilizzate per amplificatori e laser in fibra. Inoltre, le fibre multimodali drogate con itterbio (e quindi attive) potrebbero trovare applicazione per superare l'attuale deficit di banda delle fibre monomodali attraverso le tecniche di multiplexing a divisione di modo spaziale. Oggigiorno, amplificatori e laser in fibra di alta qualità sono necessari per diverse applicazioni. Tuttavia, le interferenze multimodali che provocano il degrado della qualità del profilo trasverso del campo, che dopo una brevissima distanza non è più gaussiano, sono il problema principale per lo sviluppo delle applicazioni. Quindi, la domanda è come superare questi vincoli e utilizzare fibre multimodali (step-index o graded-index) negli amplificatori, nei laser e nei sistemi di trasmissione.

L'approccio più fattibile è convertire la non linearità Kerr da problema a opportunità per la ripulitura del fascio (beam cleaning). Nel mio lavoro di tesi ho eseguito uno studio numerico approfondito di questo problema risolvendo le equazioni modali accoppiate. All'aumentare della potenza in ingresso (o del guadagno della fibra attiva), si osserva il trasferimento di energia dai modi di ordine elevato al modo fondamentale, causato dall'accoppiamento non lineare o dalla distribuzione non uniforme del guadagno. Quando il modo fondamentale può beneficiare di un guadagno maggiore, anche a causa dello scambio di potenza con i modi di ordine elevato, si raggiunge la ripulitura del fascio (che è ben visibile all'uscita della fibra).

Inoltre, per esplorare la propagazione non lineare nelle fibre multimodali drogate, ho implementato un solutore per un'equazione 3D NLSE che include guadagno (anche tenendo conto della saturazione), non linearità Kerr ed una perturbazione nel profilo d'indice del nucleo che porta all'accoppiamento tra i modi. Le simulazioni numeriche rivelano che, aumentando la potenza del segnale in ingresso, il fascio si rimodella passando dal tipico profilo speckled, con una caotica distribuzione di picchi e minimi di intensità dovuti all'interferenza tra i modi, ad un fascio ripulito. Il fenomeno dell'auto-ripulitura (self-cleaning) del fascio spaziale è ulteriormente confermato dall'esame della larghezza del fascio all'estremità della fibra e si sottolinea come i risultati delle simulazioni numeriche concordino bene con i risultati sperimentali preliminari.

Acknowledgements

First and foremost, I would like to offer my sincere gratitude to my research supervisors, Prof. Daniele Modotto, Prof. Stefan Wabnitz, Dr. Vincent Couderc and Prof. Annamaria Cucinotta for providing me unwavering support throughout my PhD study. I would like to thank Prof. Stefan Wabnitz to whom I explained my research ambitions at the beginning, and who warmly welcomed and introduced me to his brilliant research team. I highly appreciate all the valuable advices and numerous discussions received from my mentor Prof. Daniele Modotto throughout my study period, I am really grateful. I would like to thank Dr. Alessandro Tonello for his guidance, encouragement and time to discuss my progress, follow ups and making my stay at university of Limoges and XLIM research institute smooth, I am really indebted, thank you Alessandro. My sincere gratitude also goes to Dr. Vincent Couderc who made it easy for my PhD study at university of Limoges and XLIM research institute. I am greatly indebted to Prof. Annamaria Cucinotta for arranging and supporting me during my stay at university of Parma. A warm thank you also goes to Prof. Federica Poli and Prof. Stefano Selleri for introducing me to the powerful simulation tools to study ytterbium-doped fiber amplifiers at university of Parma. I am very thankful as well for the research teams at XLIM and university of Brescia, particularly Dr. Alioune Niang and Dr. Katarzyna Krupa. My sincere gratitude also extends to the community of Brescia university mainly to the department of Information Engineering, I am very grateful for all the support, thank you.

Finally, my deep and sincere gratitude goes to my dearest wife Feben Teferi, for her unparalleled love, understanding and continuous support to complete my research work. It was not a straight ride, and it could have been more difficult without your support, I am really indebted, thank you so much. I would like to thank all our family for their accompaniments and encouragements.

Contents

List of Figures

List of Abbreviations

3D NLSE	3 Dimensional Nonlinear Schrödinger Equation
ASE	Amplified Spontaneous Emission
CME	Coupled Mode Equations
CW	Continuous Wave
dBW	Decibel Watt
DGD	Different Group Dispersion
DSP	Digital Signal Processing
DWDM	Dense Wavelength Division Multiplexing
EDFA	Erbium Doped Fiber Amplifiers
FEM	Finite Element Method
FM	Fundamental Mode
FWHM	Full Width at Half Maximum
FWM	Four Wave Mixing
GIMF	Graded Index Multimode Fiber
GMMNLSE	Generalized Multimode Nonlinear Schrödinger Equation
GRIN	Graded Index
HG	Hermite–Gaussian
HOM	High Order Mode
LG	Laguerre-Gaussian
LIDAR	Light Detection and Ranging
LP	Linearly Polarized
MDM	Mode Division Multiplexing
MIMO	Multiple Input Multiple Output
MMF	Multimode Fiber
SDM	Spatial Division Multiplexing
SMF	Single Mode Fiber
SPM	Self Phase Modulation
XPM	Cross Phase Modulation
Yb	Ytterbium
YDFA	Ytterbium Doped Fiber Amplifiers

Chapter 1

Introduction

The roots of optical fiber communications is retraced back to 1854, when John Tyndall demonstrated to the Royal Society that light could be guided along a curved stream of water, and proved that light signals can be bent by total internal reflection [26]. In 1960s the very best bulk optical glasses at the time exhibited an attenuation of 10^3dB/km. The problem was an attenuation of 20 dB/km or lower is required for practical communications. By 1970 the scientists at Corning overcame this challenge and created an optical fiber with an attenuation of 17 dB/km.

Ever since their birth, fiber optic communication systems revolutionized the telecom-industry, and built today's intercontinental communication network backbone. Nowadays optical fiber based technologies has entered nearly all fields of optics. Some of the current optical fiber applications include: efficient light sources like fiber lasers, supercontinuum sources, optical sensors, and fiber-based imaging techniques. The existing fiber architectures are ranging from conventional step-index, graded-index, to sophisticated micro-structured designs like multicore or photonic-crystal fibers.

For many fiber applications an important feature is the high beam quality delivered from so called single-mode fibers, where only a Gaussian-like field distribution is guided, allowing for high coupling efficiencies and nearly diffraction limited output beams. However, in the last decade, multimode fibers which support a certain number of higher-order transverse eigenfunctions, called modes, were frequently applied in the field of high-power fiber lasers and fiber optical communications, to overcome nonlinear limitations. In the latter field, the parallelization of independent data channels in multimode fibers offers a promising solution to ensure a further increase in data capacity per single fiber [7]. In contrast, for the development of high power fiber lasers and amplifiers, unwanted multimode interferences are currently the main limiting factor [23] due to an associated degradation of the spatial beam quality.

Today, the growth rate of traffic capacity is astonishing. In other words, the communication capacity is progressively increasing per year, and has achieved more than 100 Tbit/s in a system using the existing multiplexing technologies over standard fibre systems employing single mode fibres. These transmission technologies using single-mode fibers are currently facing a capacity crunch. The limits are imposed, on the first hand by received optical signal-to-noise ratio, established by Shannon theorem [57] [13] and, on the other side, by the fiber nonlinear transmission impairments [14] under the effect of the Kerr process and the increase of the launched input power. It exists a large demand of high speed data rate because of the approaching of the full capacity in the existing infrastructures. Transmitting information in an optical fibre at higher bit rate is physically difficult because the optical signal is impaired by several factors. The need for increased capacity of the network is still the major challenge, and is difficult to achieve using standard single mode fibre.

A newly proposed technique, exploiting a multimode fibre to increase the capacity is one of the existing solutions. Recent work has indicated that the use of multimode fibres has become attractive in networks as they can propagate simultaneously up to 100 modes and more, realising optical fibres with an increased capacity [63].

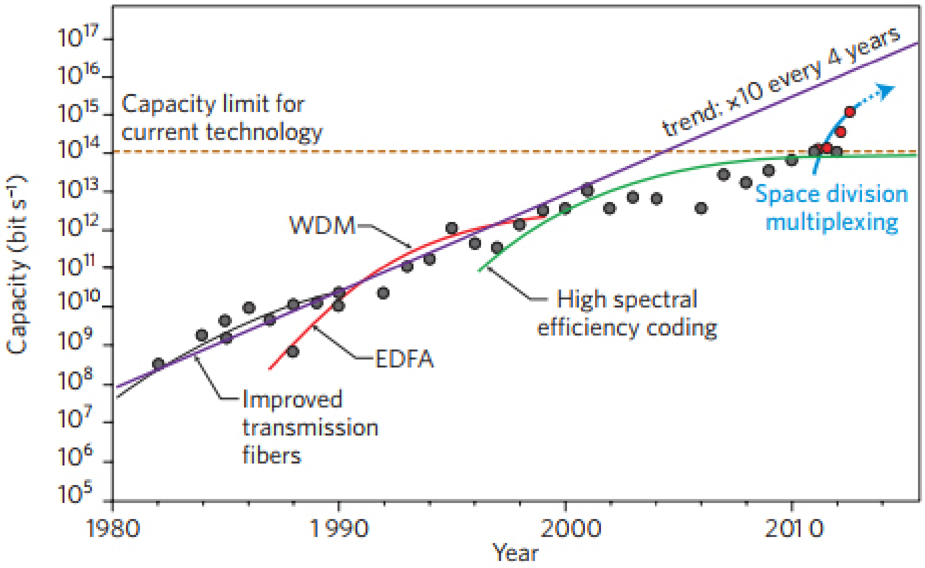

Figure 1.1: Evolution of transmission capacity in optical fibres as documented by experimental demonstrations [52].

To cope with an increasing bandwidth problems, the use of wavelength multiplexing techniques, with first wavelength division multiplexing and then dense wavelength division multiplexing (DWDM), is implemented. Hence many relevant techniques have been developed to obtain such higher bandwidths. However, DWDM implementations, which are suitable for long haul fibre connection, tend to be too costly for data centre applications and so alternative methods for more cost effective solutions and increasing short haul bandwidths are actively being sought.

We need new multiplexing technologies as a new path for utilising and increasing the transmission capacity by making use of a last option that is space [31], which is known as space (spatial) division multiplexing (SDM) in new optical fibres, the concept introduced by Paul Facq and et al.[10]. This multiplexing technology, employed in SDM systems, can obviously support the multiple numbers of mode channels, and optical amplifiers operating with optical connectors and space-(de)multiplexers (S-MUX, S-DEMUX) used with multimode fibres. The SDM approach aims to increase the capacity by the number of modes (i.e. a mode division multiplexing (MDM)) or the number of spatial input channels in which there are great advantages over the existing approaches, i.e. time or wavelength, promising the potential for a reduction in cost and providing more energy efficiency per bit transmitted.

Including mode-division multiplexing as a subset of SDM and using a new optical fibre that has high power tolerance and suppresses undesired optical nonlinear effects, a multimode fibre (MMF) can be used to map signal channels onto different transmission modes. This is now being thought as a new way of increasing the capacity by using the multiple numbers of modes, channels, and cores. It is available to be implemented in either free space (by multiple beams) or guided media. However, there is the need to overcome the major limitation of bandwidth that is brought about by modal dispersion in a MMF and the critical issue of modal crosstalk that has required digital signal processing (DSP) techniques to compensate for unwanted linear distortion and multiple input multiple output (MIMO) techniques, as employed in wireless communication, at the receiver to equalise the signal . At the receiver end, the different group dispersion (DGD) affects the original signal so that it cannot maintain its shape which will eventually result in more difficulties for the DSP-MIMO equaliser. Therefore, it is necessary to minimise the distortion by measuring each mode coherently across the beam and sending these modes to the DSP-MIMO that can unscramble the signal and equalise the group delay and hence be able to reconstruct the input field. These are the reasons why today researches have been intensively investigating SDM along with the new transmission fibre types to maximise the capacity and mitigate nonlinear optical effects.

1.1 Research Motivation

Optical fibers provide the backbone of today's global communication networks, and enable compact, low cost light sources for a variety of industrial and biomedical applications. In most of these and other applications, single mode fibers are used. Replacing single mode fibers with multimode fibers leads to a dramatic growth of transmission capacity, and a substantial increase of average power and pulse energy from fiber lasers (amplifiers).

Multimode fiber has a relatively larger core diameter than single mode fiber, that allows multiple modes of light to go through at a given time. Graded index multimode optical fibers are explored to overcome the current capacity crunch of single-mode fibers. In single-mode fiber, it requires adding more and more single-mode fibers to satisfy this demand which is expensive. The promising solution to this potential bandwidth problem is utilizing multimode fibers which enhances the capacity of optical communication systems through the technique of spatial or mode division multiplexing due to its large core size [15] [52]. Furthermore, multimode fibers are being explored as a means of adding new degrees of freedom to optical technologies such as telecommunications, fiber lasers, imaging and measurement. Multimode interferences which results in degradation of spacial beam quality currently are the main problem, for developing high power fiber lasers and amplifiers.

Due to spatial dispersion and resulting mode interference, multimode fibers suffer from an inherent randomization of the spatial transverse beam profile, resulting in a beam scrambling in a complex speckled pattern. On the other hand, high beam quality simultaneously with high power fiber amplifiers are required for different applications. The main question is how to overcome these constraints and use multimode fibers. The best approach is to convert the problem of Kerr nonlinearity to an opportunity through beam cleaning phenomenon.

My research activity explores the techniques to suppress the effect of high order modes that creates inter-modal interferences, in multimode fiber by using parabolic and ring dopant profiles. Along the course of propagation in active multimode fiber there is exchange of power from the high order modes to fundamental mode, via mode coupling due to the nonlinearity and the non uniform gain distribution. As a result, the fundamental mode experiences higher gain or amplification due to exchange of power from the high order modes. To study this complex activity in multimode fiber, we implemented the coupled mode equation and the 3D NLSE (3 Dimensional Nonlinear Schrödinger Equation) in the presence of gain from the rare-earth dopant and Kerr nonlinearity along the fiber length. Furthermore, the effects of disorder and gain saturation are explored to understand how beam cleaning operation can be obtained by exploiting the wide opportunities of doped GRIN (graded-index) multimode fibers.

To investigate the beam propagation and amplification in active multimode fiber we began from considering a small number of guided modes. We used rate and propagation equations with different configurations of pumping schemes; forward, backward, both forward and backward pumping. Then, we moved on considering a large number of modes with complex coupled mode equations and 3D NLSE's. Though multimode fiber amplifiers are the current research topics, most of the studies so far are based on passive multimode fibers and the research papers based on active multimode fibers are mostly experimental to the best of my knowledge. Powerful numerical simulations tools, taking into account the physical effects will be investigated in our research. Furthermore, the computational efficiency and similarity of our modelling tools with respect to experimental results are explored in our research activity.

1.2 Outline of the Dissertation

This research dissertation is organized under a total of seven chapters. The first chapter is dedicated to the background of the study behind multimode fibers and the motivations for the thesis work. In the second chapter graded-index multimode fibers are introduced and their properties, like self-imaging, will be thoroughly investigated. Hermite and Laguerre-Gaussian spatial mode profiles and their corresponding propagation constants with the underlying mathematical equations are presented. In addition, mode expansion, 3D NLSE and coupled mode equations which will be used further in the up-coming chapters are introduced in chapter 2.

Chapter 3 deals about modelling ytterbium-doped fiber amplifiers with limited number of modes and uniform active medium distribution in the fiber core. Solving wave equations using Comsol Multi-physics and modelling multimode fiber amplifiers are introduced. The basic rate and propagation equations are applied to understand the evolution of pump and signal powers along the fiber length. The power of the fundamental mode is varied with respect to the high order modes to investigate the gain competition among the spatial modes in multimode fiber amplifiers.

Chapter 4 is basically an extension of chapter 3, signal and pump intensities are used to determine excited and ground state populations for core and cladding pumping schemes. Forward, backward and combination of both pumping configurations are thoroughly studied for continuous wave input signal. Saturation intensity for continuous wave input and saturation fluence for pulsed input laser signals are formulated and numerically investigated. Local saturation in self-imaging input signal propagation is examined and numerical results are presented. Generally speaking the goal is how to obtain high power fiber amplifiers and fiber lasers which are used for different applications in communications, military domain, welding industry, imaging or others. The technique to maximize the gain of fiber amplifiers by optimizing parameters and using our modelling equation is also discussed in chapter 4.

Moving on, in chapter 5, mode coupling in unperturbed multimode fibers is thoroughly investigated numerically. The coupling factors in this chapter are gain and Kerr nonlinearity. Coupled mode equations due to these factors is developed using modal expansion approach. In addition to uniform gain distribution, parabolic and ring dopant profiles are investigated and numerical results under different situations are discussed and presented.

Chapter 6 explores propagation of modes in active perturbed multimode fibers. Here the perturbation factor is caused by random disorder, which is externally applied, though multimode fibers are manufactured to be resistant against bends or other external factors. In addition to gain and Kerr nonlinerity discussed in chapter 5, effects of gain saturation and disorder are analysed in detail in this chapter. 3D NLSE is used to study the propagation of modal powers and beam self-cleaning phenomenon. Furthermore, the 3D NLSE equation is extended to include the pump power, excited state populations to explore the propagation of modal power in active multimode tapered fibers. The beam self-cleaning is rigorously examined by including and then excluding pump power in the propagation equation.

Finally, conclusions of the whole thesis work and about the possible future extensions are discussed in chapter 7.

Chapter 2

Graded Index Multimode Fibers

In the first section of this chapter, we will introduce one of the most commonly used type of fiber: the graded-index (GRIN) fiber. Next we will explore the modal expansion approach used to study the self-imaging property in GRIN multimode fibers, the 3D non-linear Schroedinger equation; and then the self-imaging behaviour, which results from multimode interferences will be examined in detail accordingly.

There are many types of multimode fibers, each offering unique properties and advantages for different applications. Based on the number of modes supported and the core diameter we define single mode and multimode fibers. Similarly, depending on refractive index profile we have graded index and step index fibers. In this chapter, we will examine graded-index (GRIN) multimode fibers (MMF) in depth. Graded-index multimode fiber (GRIN MMF) uses a parabolic refractive index profiling inside the core to compensate for the different path lengths of the modes, according to an approach based on ray optics. Graded-index fiber offers hundreds of times more bandwidth than step index fiber, in addition for reducing the effect of dispersion, and providing unique important feature for self-imaging phenomenon. Graded-index fiber is made with a range of materials in the core which are chosen to minimize modal dispersion caused by different path lengths of different modes being transmitted along the fiber. The core index profile of graded-index fiber is curved, nearly parabolic to be exact, with lower refractive index glass on the outer region of the core. Index of refraction is related to the speed of light in the fiber, n = c/v, so a higher index of refraction indicates that light travels at a slower speed (v) relative to the speed of light in a vacuum (c). When the light propagates into a lower index of refraction material in the outer region of the core, its speeds is higher compared to the speed at the center of the core. By carefully designing and manufacturing the fiber, you can get the average speed of a higher-order mode approximately the same as the modes going straight down the fiber, reducing modal dispersion which is an important feature of graded-index multimode fibers.

2.1 Graded-index Fibers

Graded index fibers do not have a constant refractive index in the core as step-index fibers, but a decreasing core index from its maximum value n_1 at the center to the lower cladding index n_2 [4]. Radial distance dependent refractive index of a graded-index multimode fiber is given by:

$$n^2(r) = \begin{cases} n_1^2(1 - 2\Delta(\frac{r}{a})^\alpha), & 0 \le r \le a \\ n_2, & r > a \end{cases} \tag{2.1}$$

where a is core radius, $r^2 = x^2 + y^2$ is radial distance, $\Delta = \frac{n_1^2 - n_2^2}{2n_1^2}$ is relative refractive index difference and α is the profile parameter which give the characteristics refractive index profile of the fiber core. For parabolic profile $\alpha = 2$ and for triangular profile $\alpha = 1$. In step-index fiber, instead, the refractive index is constant throughout the core, and it doesn't vary with the radial distance.

$$n(r) = \begin{cases} n_1, & r \leq a \\ n_2, & r > a \end{cases} \tag{2.2}$$

In GRIN fiber the modes cluster into nearly degenerate groups (modes having similar propagation constant), and modes that belong to the same group have a minimal modal dispersion between one another. For this reason, the modal dispersion in graded-index fibers is the minimum possible [65]. Graded-index fibers are commonly used in fiber-optic communications to reduce modal dispersion, as the group velocities of all modes are nearly identical at the design wavelength [44]. Moreover, GRIN fibers exhibit another unique property that makes them very attractive for multimode interference applications, where the propagation constants of their modes are equally spaced [4]. As a result, their self-imaging lengths can be very short, even less than 1mm. Hence, its possible to make extremely short (submillimeter) practical multimodal interference.

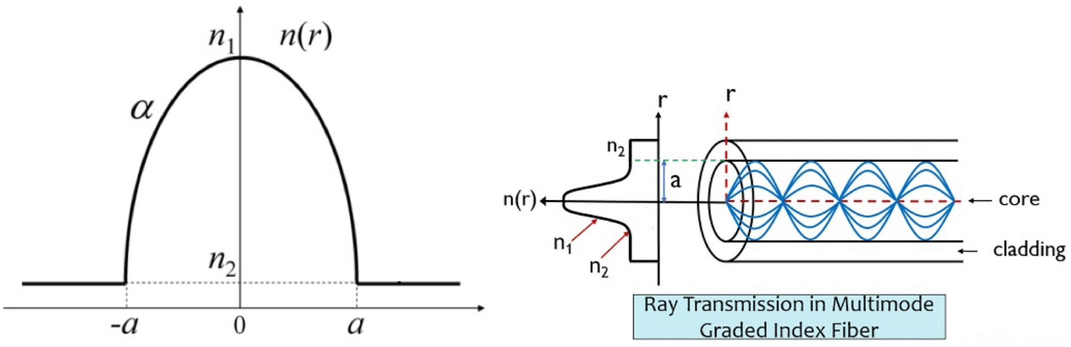

(a) **(b)**

Figure 2.1: Refractive index profile of graded-index fiber, and mode propagation phenomena inside GRIN MMF [55].

The modes of GRIN fibers are obtained by solving the Helmholtz equation [6].

$$\nabla^2 \psi_{mn}(x, y) + n^2(x, y) k_0^2 \, \psi_{mn}(x, y) = 0 \tag{2.3}$$

where $k_0 = \frac{2\pi}{\lambda}$ is the wavenumber, λ being the vacuum wavelength of the monochromatic source, r = (x, y) denotes the position in the transverse plane, and ∇^2 is the corresponding transverse Laplacian. In the weakly guiding approximation ($\Delta << 1$), both the electric and magnetic fields of all modes lie in a plane transverse to the fiber's axis ($E_z = H_z = 0$), and the modes are denoted as LP_{mn} (linearly polarized modes) , where m and n are two integers used for labeling different modes. Their modal distribution $\psi_{mn}(x, y)$ and propagation constants β_{mn} are known, but have different forms depending on whether the Helmholtz equation (2.3) is solved using Cartesian or cylindrical coordinates. Laguerre-Gaussian (LG) and Hermite-Gausssian (HG) modes are obtained when equation (2.3) is solved in cylindrical (r, ϕ, z) and Cartesian (x, y, z) coordinates, respectively. Figure 2.2 shows Hermite-Gaussian and Laguerre-Gaussian intensity profile of modes.

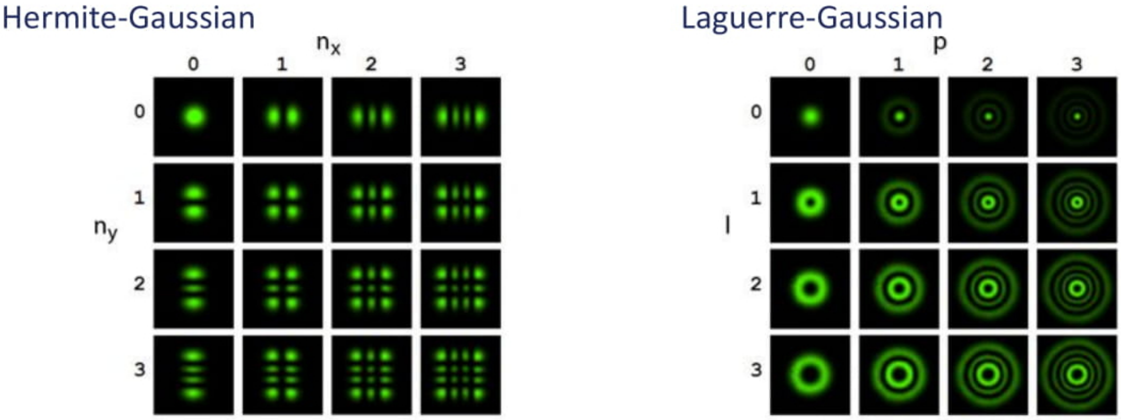

Figure 2.2: Hermite and Laguerre-Gaussian modes intensity profile

At the waist plane z = 0, the field distribution of an arbitrary Laguerre-Gaussian beam is expressed as follows [70] [11]:

$$\psi_{lp}(r,\phi) = \mathrm{E}_0 \exp\left(\frac{-r^2}{w_0^2}\right) L_p^{(l)}\left(\frac{2r^2}{w_0^2}\right) \exp(-il\phi) \tag{2.4}$$

where E_0 is normalized amplitude, l and p are the mode indices, w_0 is the waist of the fundamental Gaussian beam, $\mathrm{L}_p^{(l)}(x)$ is the generalized Laguerre function given by equation (2.5):

$$L_p^{(l)}(x) = \sum_{i=0}^{p}(-1)^i \frac{\Gamma(p+l+1)}{\Gamma(p-i+1)\Gamma(i+l+1)} \frac{x^i}{i!} \tag{2.5}$$

where Γ is Gamma function. Using equation(2.5) the first few Laguerre polynomial functions are given as follows [18]:

$$\begin{aligned} L_0^{(l)}(x) &= 1 \\ L_1^{(l)}(x) &= l+1-x \\ L_2^{(l)}(x) &= \frac{1}{2}(l+2)(l+1)-(l+2)x+\frac{1}{2}x^2 \end{aligned} \tag{2.6}$$

The corresponding propagation constant in cylindrical coordinates is also given by equation (2.7) [18].

$$\beta_{lp} = k_0 n_1 \left[1 - \frac{2(2p+l-1)}{k_0 n_1}\sqrt{\frac{2\Delta}{a^2}}\right]^{\frac{1}{2}} \tag{2.7}$$

In all of our numerical modelling we used Hermite-Gaussian modes, except in Chapter 2 where we conduct modal analysis for graded-index fibers by COMSOL Multiphysics.

Figure (2.4) below shows some of the fundamental and high order Hermite-Gaussian spatial intensity profile of modes used in our numerical simulation. Hermite–Gauss solution ($\mathrm{HG}_{\mathrm{mn}}$) modes can be obtained by separation of the variables in x and y. Using the weak-guidance approximation, a closed-form solution for the ideal modes of the MMF can be obtained in Cartesian coordinates. We define the normalized two-dimensional Hermite–Gaussian modes as [18] [58]:

$$\psi_{mn}(x,y) = \frac{\sqrt{\frac{2}{\pi}}}{w\sqrt{2^{m+n}m!n!}} H_m(\sqrt{2}\frac{x}{w}) H_n(\sqrt{2}\frac{y}{w}) e^{-\frac{x^2+y^2}{w^2}} \tag{2.8}$$

where w is the mode radius (different from frequency ω) is given by equation (2.9), $\mathrm{H}_m(x)$ and $\mathrm{H}_n(y)$ are Hermite polynomials and solutions to differential equation.

$$w^2 = \frac{\sqrt{2}a}{k_0 n_1 \sqrt{\Delta}} \tag{2.9}$$

$$\frac{d^2 H_n}{dx^2} - 2x\frac{dH_n}{dx} + 2nH_n = 0 \tag{2.10}$$

$$H_n(x) = (-1)^n \, e^{x^2} \frac{d^n}{dx^n} e^{-x^2} \tag{2.11}$$

Using equation (2.11) the first five Hermite polynomials are given by equation (2.12) below:

$$\begin{aligned} H_0(x) &= 1 \\ H_1(x) &= 2\,x \\ H_2(x) &= 4\,x^2 - 2 \\ H_3(x) &= 8\,x^3 - 12\,x \\ H_4(x) &= 16\,x^4 - 48\,x^2 + 12 \end{aligned} \tag{2.12}$$

Similarly, the modal propagation constants of Hermite-Gaussian modes in the Cartesian coordinates are given by equation (2.13) [4]:

$$\beta_{mn} = n_1 k_0 \left[1 - \frac{2(m+n-1)}{n_1 k_0 a} \sqrt{2\Delta} \right]^{\frac{1}{2}} \tag{2.13}$$

For most GRIN fibers $k_0 a >> 1$ and $\Delta << 1$, as a result, as long as m+n is not too large, we can expand β_{mn} in a binomial series and approximate it as [4]:

$$\beta_{mn} \approx n_1 k_0 - (m+n-1)\frac{\sqrt{2\Delta}}{a} \tag{2.14}$$

Equations (2.13) and (2.14) above reveals the most important features of the modes of a GRIN multimode fibers. It shows that the propagation constants of all non-degenerate modes (modes with different propagation constants) form a ladder like structure with equal spacing between any two neighbouring modes as shown in figure (2.3). This kind of characteristics is similar to the quantized energy levels of a harmonic oscillator and is the physical mechanism behind the self-imaging phenomenon in GRIN multimode fibers. In figure (2.3), the mode numbers are, the total number of modes considered with their respective propagation constants, moving sequentially from the fundamental mode (mode number 1, $\psi_{0,0}$) to the final high order mode (mode number 25, $\psi_{4,4}$). More precisely, if the indexes m, n (here used to identify the Hermite-Gauss modes) vary from 0 to m_{max}, one can move from a two-index notation m and n to a notation with a single mode number by calculating $m \cdot (m_{max} + 1) + n + 1$. From this expression the fundamental mode $m = 0, n = 0$ is mapped into mode number 1, while the largest mode number is given by $(m_{max} + 1)^2$. The spatial shape of the modes are provided by equation (2.8), and their particular propagation constants are given by equation (2.13). In addition from figure (2.3), we can understand that the mode number 1 (fundamental mode) has the largest propagation constant, whereas the mode number 25 (the highest order mode), has the smallest propagation constant. Furthermore, there are mode groups with the same propagation constants, but in general the propagation constant reduces moving from mode number 1 towards mode number 25.

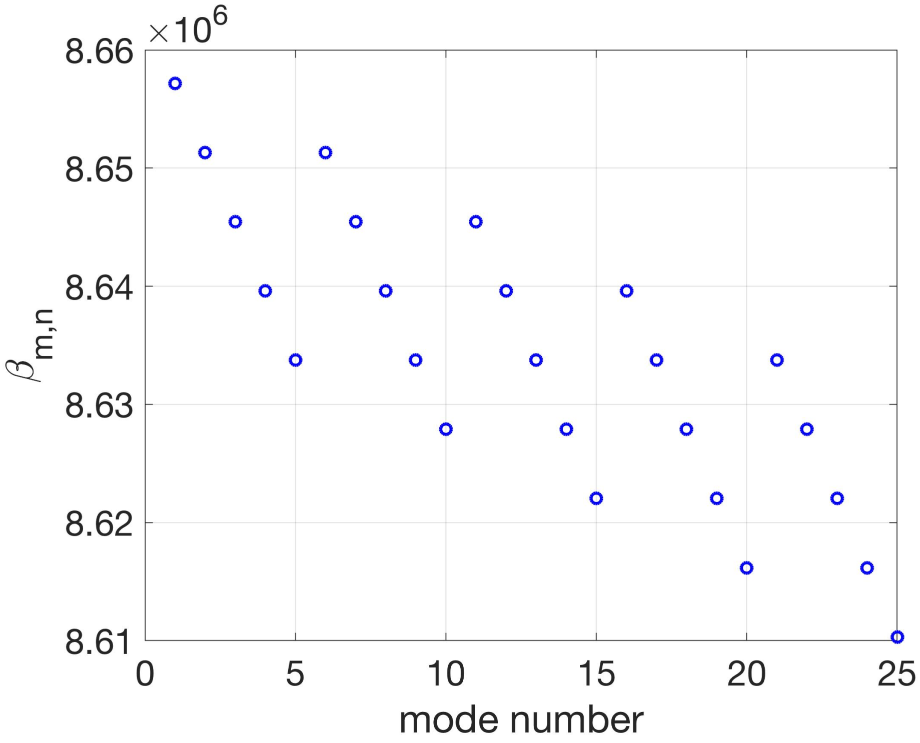

Figure 2.3: Graded-index multimode fiber propagation constant plot.

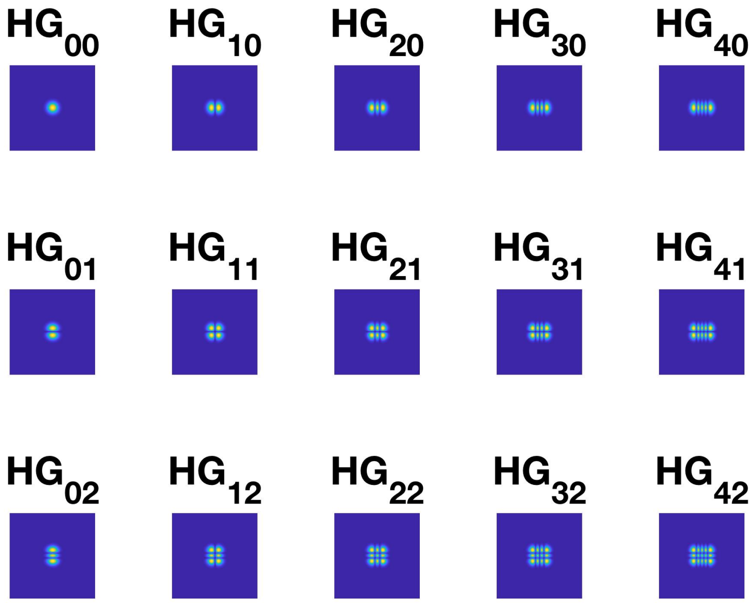

Figure 2.4: Intensity patterns of Hermite-Gaussian (HG$_{mn}$) modes

2.2 Mode Expansion

We start with a description of the propagation of light in a multimode fiber in the absence of gain or absorption, and choose a set of transverse modes ψ_n, n=1,2,...N which best represent the fiber's eigenmodes. Here it's basically assumed that the modes propagate with negligible coupling to each other, changing only the phase terms of their complex amplitudes. Due to the orthogonality of eigenmodes, the total guided field (optical field) $E_g(x,y,z)$ ($\frac{\sqrt{W}}{m}$) inside the fiber can be expressed as the superposition of all eigenmodes in the core [20] [61]. In other words the propagating field can be expanded through the base of guided modes $\psi_n(x,y)$ and the optical field at any point along the fiber's axis of propagation z is written as:

$$E_g(x,y,z) = \sum_n a_n(z)\psi_n(x,y)e^{i\beta_n z} \ + \ radiation \ \ modes \tag{2.15}$$

where (x,y) are the transverse coordinates, $\psi_n(x,y)$ (1/m) is the n-th normalized bound eigenmodes, a_n is the complex amplitude ($\sqrt{W}$) which describes both amplitude and phase of the corresponding mode, and β_n is the n-th modal propagation constant. Because the field transformation of guided eigenmodes into radiation ones is a negligible effect for typical fiber parameters, hence we will ignore the radiation modes. When this set of modes constitutes an orthonormal basis, the modal amplitude $a_n(z)$ is given by the projection of the optical field at the input facet over the n-th modal field [20] [4]. In other words, since the eigenmode set is a base for any guided light fields, the injection amplitudes are determined as the coefficients of decomposition upon this base, of the optical field injected at the fiber input facet:

$$a_n(0) = \int_{-\infty}^{+\infty}\int_{-\infty}^{+\infty} E_g(x,y,0)\psi_n^*(x,y)\mathrm{d}x\mathrm{d}y \tag{2.16}$$

In equation (2.16) above the slowly varying amplitude is obtained when input incident beam is normal (not inclined). Considering a Gaussian input beam launched into the GRIN fiber inclined at angle θ we use the following general equation to determine the amplitude.

$$E_g(x,y,0) = A_0\, exp\left(-\frac{x^2+y^2}{w^2}\right)\, exp(j\,k\,\mathrm{x}\,sin\theta) \tag{2.17}$$

$$a_n(0) = \int_{-\infty}^{+\infty}\int_{-\infty}^{+\infty} A_0\, exp\left(-\frac{x^2+y^2}{w^2}\right)\psi_n^*(x,y)\, exp(j\,k\,\mathrm{x}\,sin\theta)\mathrm{d}x\mathrm{d}y \tag{2.18}$$

Where k is the wave number in radians per meter for a free-space wavelength λ, A_0 is the field amplitude at the fiber input in square root of watts per meter ($\frac{\sqrt{W}}{m}$), and w is the radius of the beam at which the field amplitude falls to 1/e of its axial values that is related to the full width at half maximum (FWHM) as follows:

$$w = \frac{FWHM}{\sqrt{2ln2}} \tag{2.19}$$

For an orthonormal modal basis we have:

$$\int_{-\infty}^{+\infty}\int_{-\infty}^{+\infty} \psi_n(x,y)\psi_m^*(x,y)\mathrm{d}x\mathrm{d}y = \delta_{m,n} \tag{2.20}$$

The optical intensity (W/m^2) is normalized in such a way that it can be obtained by squaring the modules of the guided field given by equation 2.15. Here we can rewrite the intensity in terms of the transformed guided field.

$$\begin{aligned} I(x,y,z) &= \left|E_g(x,y,z)\right|^2 \\ &= \sum_{n,m} a_n(z)a_m^*(z)\psi_n(x,y)\psi_m^*(x,y)e^{i(\beta_n-\beta_m)z} \end{aligned} \tag{2.21}$$

The total local-modal power (W) is also simply calculated by integrating the intensity across the fiber cross section. The total power in multimode fiber could also be obtained by summing up the square of all the guided modes amplitude as shown in equation (2.22).

$$\begin{aligned} P(z) &= \int_{-\infty}^{+\infty}\int_{-\infty}^{+\infty} I(x,y,z)dxdy \\ &= \int_{-\infty}^{+\infty}\int_{-\infty}^{+\infty} \sum_{n,m} a_n(z)a_m^*(z)\psi_n(x,y)\psi_m^*(x,y)e^{i(\beta_n-\beta_m)z}dxdy \\ P(z) &= \sum_n |a_n(z)|^2 \end{aligned} \tag{2.22}$$

Likewise, the power evolution of each mode across the propagation direction is given by equation (2.23) [20]. The power of each mode is obtained by squaring its modal amplitude at the propagation direction.

$$P_n(z) = |a_n(z)|^2 \tag{2.23}$$

The width of input Gaussian beam should be relatively close to the beam width of the fundamental mode, in order to use small number of mode for simulations. Otherwise, large number of modes need to be considered for numerical simulations in graded-index multimode fiber. One important method to check this is the input power that could be determined by summation of the modes square amplitude, and the power calculated by integrating the square of the Gaussian input beam across the fiber transverse should closely match.

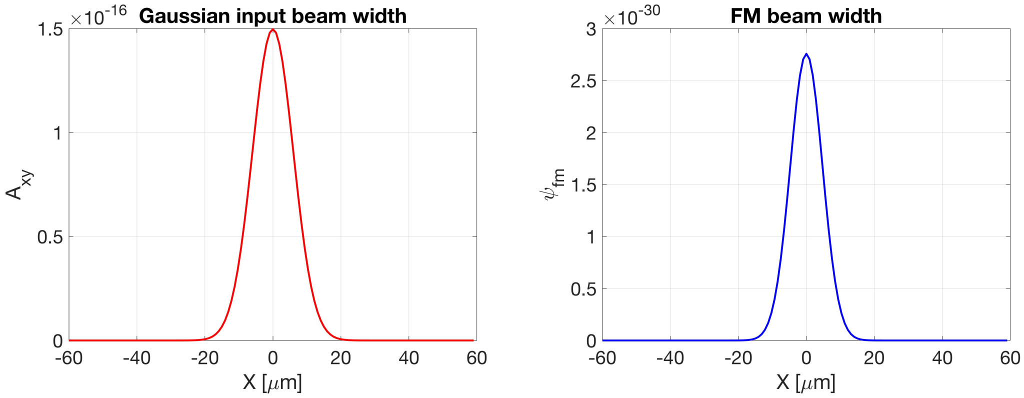

(a) Gaussian input beam width **(b)** Fundamental mode beam width

Figure 2.5: Gaussian input beam diameter of $10\mu m$ FWHM and fundamental mode width.

In other words, if a proper number of modes and input Gaussian beam width is set for numerical simulations, the following input power equations (Equation 2.24) should be equal at z = 0.

$$\begin{aligned} P(x,y,0) &= \int_{-\infty}^{+\infty}\int_{-\infty}^{+\infty} \left| A_0\, exp\left(-\frac{x^2+y^2}{w_0^2}\right) exp(j\,k\,x\,sin\theta)\right|^2 dxdy \\ P(x,y,0) &= \sum_{n}^{N} |a_n(0)|^2 \end{aligned} \tag{2.24}$$

2.3 3D Nonlinear Schroedinger Equation

An essential tool for analysing multimode non-linear optical beam propagation, will be introduced in this section. To probe the non-linear behaviour of multimode fibers, we first present the most common theoretical model used for this task, the generalized multimode non-linear Schrodinger equations (GMMNLSE). Multimode non-linear graded-index fibers will be examined using generalized multimode non-linear Schroedinger equation. The generalized MMNLSE was first derived by Poletti and Horak [50]. Generalized MMNLSE, however suffers from increasing complexity particularly with increasing number of modes. In a highly multimode fiber, it may be computationally much more efficient to use a direct numerical solution of the 3D NLSE. Hence, for a GRIN MMF the complex guided field $E_g(x,y,z)$ [$\sqrt{W}$/m] equation is approximated and simplified as follows [32]. In situations where many guided modes must be considered, this equation will offer computational advantages over the GMMNLSE. Such equation is also called the Gross-Pitaevskii equation.

$$i\frac{\partial E_g}{\partial z} + \frac{1}{2\beta}\nabla_\perp^2 E_g - \frac{\beta\Delta}{a^2}r^2 E_g + \frac{\omega n_{2kerr}}{c}(1-f_r)|E_g|^2 E_g = 0 \tag{2.25}$$

where $\nabla_\perp^2 = \partial_x^2 + \partial_y^2$ is transverse Laplacian, $\beta = \frac{\omega n_1}{c}$ is propagation constant, ω is carrier frequency in rad/s, $\Delta = \frac{n_1^2 - n_2^2}{2n_1^2}$ is the relative index difference, a is the fiber core radius, n_1 is the maximum core refractive index, n_2 is the cladding refractive index, n_{2kerr} is non-linear refractive index having a value of 3.2×10^{-20} m^2/W for fused silica used to fabricate silica fibers, $f_r \approx 0.18$ is the fractional contribution of the Raman response to the total non-linearity. Equation 2.25 is a powerful tool to study the effects of diffraction, waveguide and Kerr non-linearity in beam propagation. A simplified case with only spatial dependency is investigated in this equation, a slowly varying envelope approximation, unidirectional propagation, a simplified waveguide contribution, and a constant group velocity dispersion are some of the assumptions at the base of this model. We neglected the effects of gain, dispersion and saturations from the 3D NLSE for the moment. Except dispersion, the effects of gain saturation and dopants in GRIN MMF will be examined further in our research.

In [37][41] it is assumed that the beam diameter is much smaller than the core radius, and the real graded index profile of the fiber is also approximated. Our numerical model is based on Hermite-Gaussian modes (solutions for parabolic profile) which is a good approximation for practical implementations in a GRIN multimode fibers. In the beam propagation method (BPM) of our model, the real refractive index profile having a constant refractive index value for the cladding is used. The comparison between the coupled mode equation (based on the modes of the parabolic profile) and the BPM (based on the real profile) shows a good agreement even in the nonlinear regime and this confirms that the parabolic approximation works well with our input beam width.

2.3.1 Coupled Mode Equation

Here we will investigate the coupled mode equation in passive graded-index multimode fibers, due to Kerr nonlinearity. By substituting the modal expansion equation (2.15) into the 3D NLSE given by equation (6.1), we could find non-linear coupled equations given as follows for passive multimode fibers [6]:
where $E_g = \sum_n A_n(z)\psi_n(x,y)$ and $A_n(z) = a_n(z)e^{i\beta_n z}$

$$\sum(\frac{\partial A_n}{\partial z})\psi_n - \sum i\beta_n A_n \psi_n = i\frac{n_{2kerr}\omega}{c}\sum_{m,p,q} A_m A_p^* A_q \psi_m \psi_p^* \psi_q \tag{2.26}$$

Now exploiting the orthogonality among the modes which is given by equation (2.20) and projecting over ψ_n^*, and by substituting for $A_n(z) = a_n(z)e^{i\beta_n z}$ we can obtain the following coupled mode system:

$$\frac{\partial A_n}{\partial z} = i\beta_n A_n + i\frac{n_{2kerr}\omega}{c}\sum_{m,p,q} A_m A_p^* A_q \psi_m \psi_p^* \psi_q \psi_n^* \tag{2.27}$$

$$\frac{\partial a_n}{\partial z} + i\beta_n a_n = i\beta_n a_n + i\frac{n_{2kerr}\omega}{c} \sum_{m,p,q} Q_{m,p,q,n} a_m a_p^* a_q e^{i(\beta_m - \beta_p + \beta_q - \beta_n)z} \tag{2.28}$$

$$\frac{da_n}{dz} = i\frac{n_{2kerr}\omega}{c} \sum_{m,p,q} Q_{m,p,q,n}\ a_m\ a_p^*\ a_q\ e^{i\Delta\beta_{m,p,q,n}z} \tag{2.29}$$

where a_n represents the slowly varying complex amplitude of mode n, $Q_{m,p,q,n} = \int\int \psi_m \psi_p^* \psi_q \psi_n^* \mathrm{dxdy}$ is an overlap integral, $\Delta\beta_{m,p,q,n} = \beta_m - \beta_p + \beta_q - \beta_n$ is the phase mismatch, and $\psi_n(x,y)$ is the n-th orthonormal basis of guided modes, for the mode group with indices m, n, p, q.

Non-linearity introduces coupling between different modes, and in multimode propagation it introduces opportunities and at the same time problems. Non-linear effects in optical fibers arise due to interactions between propagating light and the fiber. Non-linear effects are weak in optical fiber at low power, but becomes stronger when light reaches certain threshold values, which occurs when the power is increased. There are different categories of non-linear effects, however in our study we will focus on effects that arises from the power dependent refractive index, such as self-phase modulation, cross-phase modulation and four-wave mixing. These non-linear effects leads to interferences, distortions, noise and excess attenuation of optical signals which limits the system performance.

Self-phase modulation (SPM) is non-linear effects that corresponds to $\mathrm{Q}_{m,m,m,m}$ and terms of the form $|\mathrm{a_m}|^2\mathrm{a_m}$ [65] in equation (5.7). Similarly, cross phase modulations (XPM) have terms of the form $\mathrm{Q}_{m,n,m,n}$ and $\mathrm{Q}_{m,m,n,n}$ where m $\neq$ n, and are of the form $|\mathrm{a_n}|^2\mathrm{a_m}$. XPM can lead to asymmetric spectral broadening when two pulses are travelling at different speeds. SPM and XPM are pure phase modulations, and cannot cause energy exchange between modes. All other non-linear coupling terms can be described as four-wave mixing (FWM), which is defined as terms that can cause transfer of energy.

2.4 Self-imaging in GRIN Fiber

When an electromagnetic field is coupled into a graded-index multimode fiber, a set of eigenmodes are excited and each of them propagates along the fiber independently with its own propagation constant. The excited modes interfere with each other and the field at any position inside the multimode fiber is a superposition of their mode field. The self-imaging of the input field inside graded-index multimode fiber can be obtained at certain positions where the excited modes are in phase [22]. The optical field $E_g(x,y,z)$ at any point inside the GRIN fiber is obtained by multiplying each mode with a phase factor, because all excited modes propagate independently inside the MM fiber, and the field $E_g(x,y,z)$ along the fiber is given by equation 2.15. Consider the case of two consecutive modes that are mostly excited, with propagation constants β_1 and β_n. Lets say β_1 is the propagation constants of the fundamental mode and β_n the propagation constants of n-th excited mode of the MM fiber. At certain positions inside the MM fiber, the reproduction of the input field occurs [71], that is, $\mathrm{E}_g(x,y,z_{self-image}) = \mathrm{E}_g(x,y,z=0)$, if the following condition is satisfied for all N modes.

$$(\beta_n - \beta_1)z_{self-image} = 2\pi m \tag{2.30}$$

Equation 2.30 indicates that the phase difference between any two excited modes is an integer multiple of 2π, that is, all excited modes are in phase. Self-imaging occurs at points $z_{self-image}$ along the multimode fiber. The self-image distance or the period (Λ) of longitudinal spatial oscillation is given by the following equation where a is fiber core radius and Δ relative index difference.

$$\Lambda = \frac{a\pi}{\sqrt{2\Delta}} \tag{2.31}$$

To investigate the self-imaging phenomenon in graded-index multimode fiber, we used modal expansion approach discussed in section 1.2 above, and 3D NLSE. In addition, for the numerical simulation I considered passive GRIN multimode fiber, and Kerr non-linear effect. For continuous-wave (CW) excitations, the propagation of a beam in a parabolic GRIN MMF experiences self-imaging.

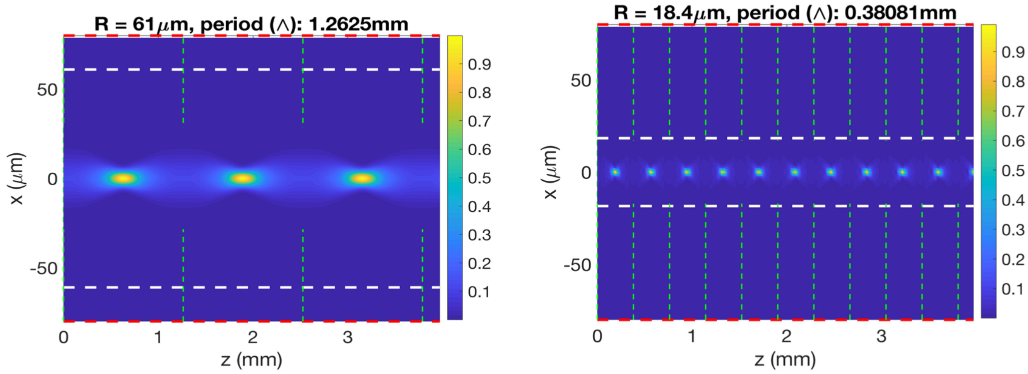

(a) Larger core end

(b) Smaller core end

Figure 2.6: Self-imaging phenomena in GRIN MMF: (a) Core radius $61\mu m$ (b) Core radius $18.4\mu m$

Figure 2.6 shows self-imaging phenomena in GRIN multimode fiber having the core radius of $61\mu m$ and $18.4\mu m$. The self imaging period which is directly related to the core radius is calculated using equation 2.31, and found to be 1.263mm and 0.381mm respectively. We used mode expansion approach to determine the self imaging period with normal input beam inclination in passive multimode fiber. Likewise, figure 2.8 shows inclined Gaussian input beam propagation in GRIN MMF, keeping other parameters the same as in the normal input or no inclination case. The input beam is inclined at the input facet of the fiber about 2.5° from the longitudinal axis, as it could also be visualized from figure 2.7.

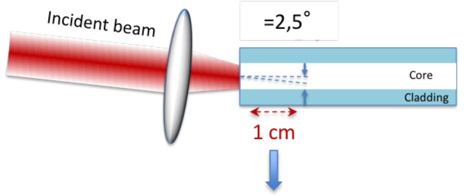

Figure 2.7: Inclined input beam injected at the input facet of graded-index MMF.

It can be seen from the figure that, the self-imaging period remains the same, but the interference shows zigzag behaviour inside the core.

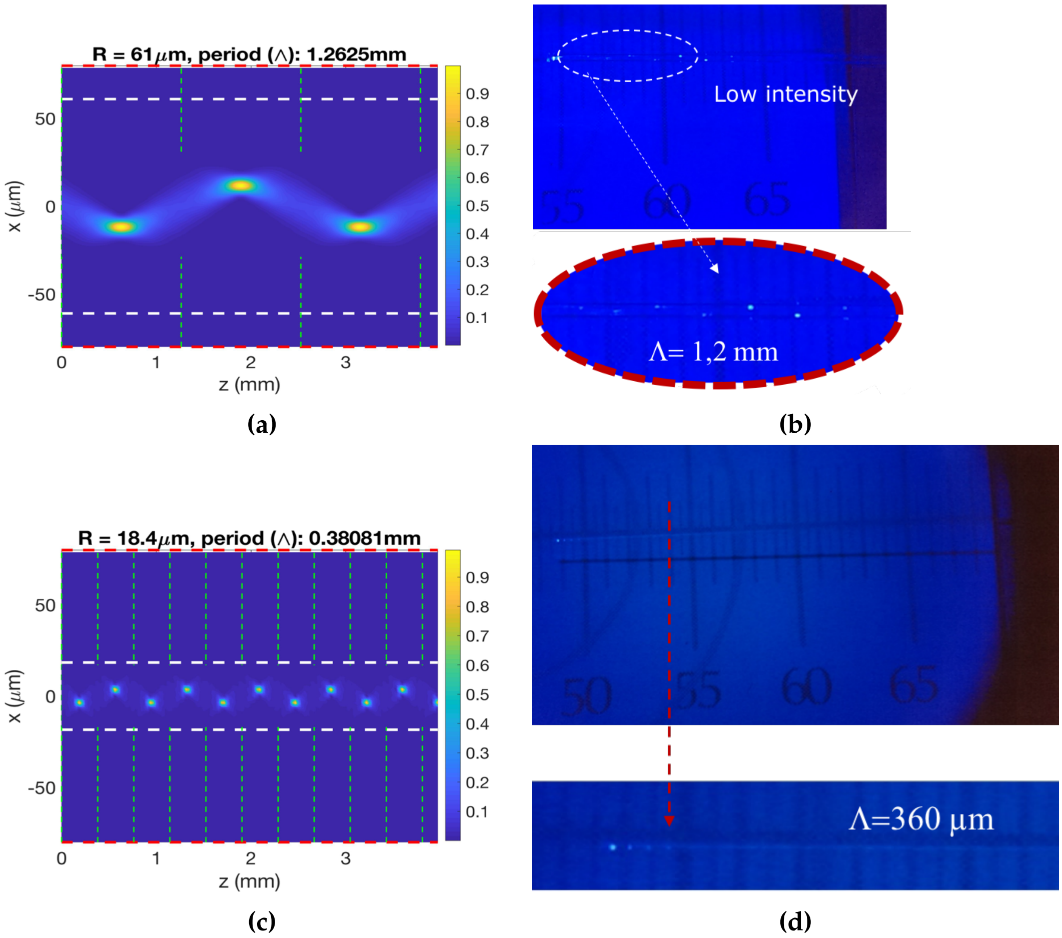

(a) **(b)** **(c)** **(d)**

Figure 2.8: Self-imaging in GRIN MMF with inclined input beam: (a) Numerical simulation results with large core size (b) Experimental result with large core size (c) Simulation result with smaller core size (d) Experimental result with smaller core diameter

Figure 2.8 shows inclined input beam propagation across passive GRIN MMF. Panels (a) and (c) refers to my numerical simulations using equation (2.15) and the analysis developed in section 2.1, while panels (b) and (d) refer to an experimental visualisation of the self-imaging period carried out by the colleagues at the XLIM laboratory. The two fiber diameters are taken from short segments of fiber near the small and the large section of a tapered multimode fiber, which was experimentally analysed in [46]. The period of self-imaging in numerical simulation and experimental results are in a relative good agreement. In the experiment a laser beam at a wavelength of 1064nm with CW Gaussian spatial shape is launched into the smaller core size of the tapered GRIN MMF. Self replicating spots of the beam at equal distance appears along the fiber length. The distance between each spot is equivalent to the self-imaging distance or period calculated by using equation (2.31) and the same as in the numerical simulations.

2.5 Chapter Summary

In this chapter graded-index multimode fibers and their properties are introduced, parabolic refractive index and step-index profiles are defined and formulated. Solutions to Helmholtz wave equation using Cartesian or cylindrical coordinates are thoroughly investigated and their corresponding mode intensity profiles are plotted. Hermite-Gaussian and Laguerre-Gaussian spatial mode equations with their respective propagation constants are discussed.

Mode expansion is the way of representing the guided optical field as a superposition of eigenmodes inside the core. The basic equation that relates modal amplitude to modal power is developed and analysed. We also presented mathematical derivation that shows how the coupled mode equations are determined from the 3D NLSE using the mode expansions.

Finally, the self-imaging property of graded-index multimode fiber that results from the modal interference inside the core is explored. We have investigated the self-imaging under normal and inclined input laser beam. The period of self-imaging remains the same under both conditions, but a zigzag displacement of the signal is observed in the latter. Furthermore, we also compared the self-imaging period we obtained numerically with experimental value, and found out that the two results are in a good agreement.

Chapter 3

Modelling of Ytterbium-doped Fibers

In this chapter we will investigate ytterbium doped fiber amplifiers that support few number of modes. First we will consider the modelling of graded-index fibers with Comsol Multiphysics, and solve wave equations to obtain spatial modes. The spatial modes are then used in propagation and rate equations to determine the power carried by each mode. Propagation equations of signal and pump are solved using the Runge-Kutta method given the initial conditions, to determine the signal and pump powers at any distance in the propagation direction. Finally our numerical simulation results will be shown and discussed. This chapter is a foundation for up-coming chapters where more complex effects are included, and large number of modes are considered. Here the fiber core is uniformly doped and the power of each mode (fundamental or higher order) is controlled manually. In other words, the power of each mode is set in the numerical simulation system. However practically as the number of modes increase and other effects are included this model has its shortcomings.

The need for higher output powers and the growth of fiber-based applications beyond the telecommunication industry, triggered the study of other rare earth dopants such as ytterbium (Yb). Ytterbium-doped fibers in particular, were found to have a number of advantages due to their distinctive electronic structure, which favours their use in high power laser systems. Ytterbium-doped fibers were not regularly used at the beginning, though Yb-doped fiber laser was discovered in 1988 [21]. This was due to the popularity of other rare-earth dopants like erbium and neodymium. Erbium doped fibers have the advantage that their emission wavelength (1520 to 1600 nm) lies in the telecommunication wavelength region and they can be pumped at a number of wavelengths from 510 to 1480nm. Neodymium doped fibers exhibit a four-level behaviour with highly efficient emission at 1060 nm wavelength for pumping at about 800 nm. However, these rare-earth dopants have explicit pitfalls, for instance, there is excited state absorption in erbium-doped fibers, and a limited emission bandwidth in neodymium-doped fibers. These drawbacks undoubtedly curbs the gain as well as applications of such fibers. For these and other reasons, ytterbium-doped fibers were of a great interest and studied in detail by Paschotta et al. in 1997 [48].

Applications of ytterbium-doped fiber amplifiers includes power amplification for spectroscopic measurements, free space laser communications, and small-signal amplifiers in fiber sensing [48]. Ytterbium-doped fiber amplifiers provide broad-gain bandwidth for high output power with excellent power conversion efficiency. In Yb-doped fibers many of the shortcomings which are well-known from erbium-doped amplifiers are avoided. Hence, high doping levels is possible which leads to high gain in a short length of fiber. The broad bandwidth is also ideal for the amplification of ultra-short pulses, and the high saturation fluence allows for high pulse energies. There is also a wide range of possible pump wavelengths (860nm to 1064nm), allowing a variety of pumping schemes, including the use of diode lasers or even high-power neodymium lasers.

3.1 Yb-doped Fiber Amplifier Modelling

This section explores my research activity at university of Parma with the research team in the department of Engineering and Architecture. We used Comsol Multiphysics a general finite-element modelling tool mode solver to obtain electric and magnetic field components of optical modes in Yb-doped graded-index fibers. Comsol can be linked with the general computing software Matlab through the use of a scripting language. Consequently, the user can program in the Matlab environment, and then call Comsol to solve the physical modelling problems. Finally, the numerical solutions given by Comsol are extracted and processed in Matlab. The eigen solutions (modal effective indices and electro magnetic fields) of the user-defined optical fiber obtained from Comsol are vector solutions. For weakly guiding fibers, the vector modes obtained from Comsol are then processed in Matlab to produce intensity modes (LP modes), for the scalar-model ytterbium-doped fiber amplifier simulations. In addition, as modal effective indices and modal profiles can be attained from Comsol directly, other basic modal properties such as modal dispersion and modal effective area can be acquired through simple post-processing in Matlab.

3.1.1 Determining Modes with Comsol Multi-physics

When solving wave electromagnetics problems with Wave Optics module, we use the finite element method for the governing Maxwell's equations. COMSOL Multiphysics uses finite element method to solve for electromagnetic fields within the modelling domains. The governing Maxwell's equations in three dimensions can be solved for the electric field, $\mathrm{E} = \mathrm{E}(x, y, z)$, throughout the modelling domain, where E is a vector with components $\mathrm{E} =< \mathrm{E}_x, \mathrm{E}_y, \mathrm{E}_z >$. All other quantities (such as magnetic fields, currents, and power flow) can be derived from the electric field. It is also possible to reformulate the above equation as an eigenvalue problem, where a model is solved for the resonant frequencies of the system, rather than the response of the system at a particular frequency. We can break down the finite element method into four steps:

1. **Model set-up:** Defining the equations to solve, creating the model geometry, defining the material properties, setting up metallic and radiating boundaries, and connecting the model to other devices.

2. **Meshing:** Discretizing the model space using finite elements. Whenever solving a wave electromagnetics problem, you must keep in mind the mesh resolution. Any wave-type problem must have a mesh that is fine enough to resolve the wavelengths in all media being modeled. This idea is fundamentally similar to the concept of the Nyquist frequency in signal processing. The sampling size (the finite element mesh size) must be at least less than one-half of the wavelength being resolved, 1064 nm in our case.

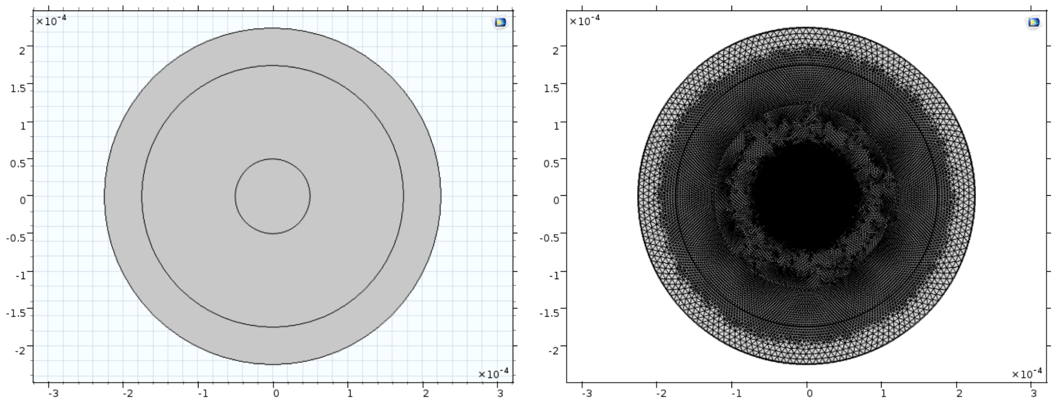

(a) **(b)**

Figure 3.1: Fiber geometry modelling with Comsol: (a) Fiber cross section (b) Meshed fiber cross section

3. **Solving:** Solving a set of linear equations that describe the electric fields. Once we have properly defined the problem and meshed our domains, COMSOL Multiphysics will take this information and form a system of linear equations, which are solved using either a direct or iterative solver.

4. **Postprocessing:** Extracting useful information from the computed electric fields. Once we have solved the model, we can extract data from the computed electromagnetic fields. COMSOL Multiphysics will automatically produce a slice plot of the magnitude of the electric field, but there are many other post-processing visualizations we can set up, like numerical information from our models.

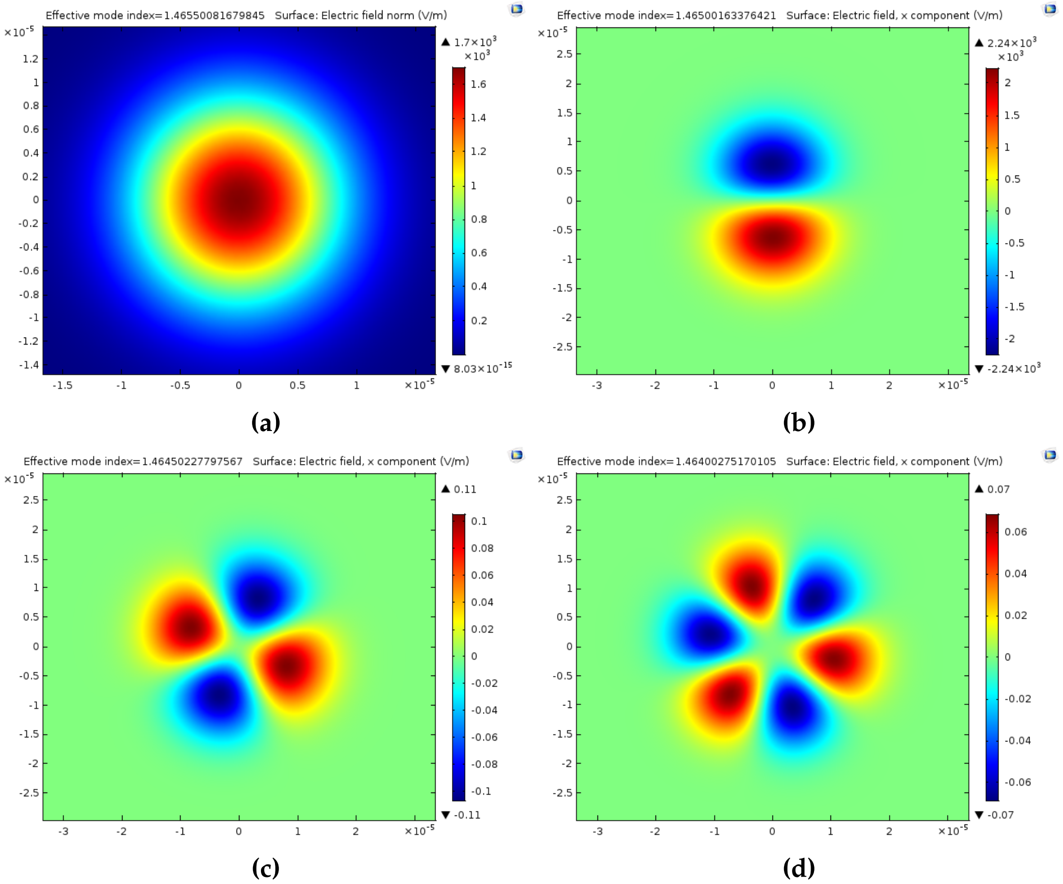

(a) **(b)**

(c) **(d)**

Figure 3.2: Fundamental and high order modes obtained by Comsol Multi-physics mode solver: (a) LP_{01} (b) LP_{11} (c) LP_{21} (c) LP_{31}

Parameters	**Value**	**Parameters**	**Value**
$R_{core}(\mu m)$	26	$\lambda_s(nm)$	1064
$R_{clad-1}(\mu m)$	175	$\lambda_p(nm)$	976
$R_{clad-2}(\mu m)$	225	n_1	1.466
n_2	1.45	n_3	1.37

Table 3.1: Parameters and respective values used for modelling with Comsol.

3.1.2 The Amplifier Model

Once we solve the wave equation using Comsol Multiphysics and obtain the modes, we will extract required parameters like intensity of signal (modes), intensity of pump, overlap integrals and etc., then its time to model our ytterbium-doped fiber amplifier. The operation of ytterbium-doped fiber amplifier is described by coupled differential equations [56], which involves:

1. Evolution intensities of the various signal and pump modes along the amplifying medium. This includes, the intensity evolution equations for signal and amplified spontaneous emission (ASE) in the i-th signal mode at the wavelength λ_s, and intensity evolution equation for the power in the pump mode at wavelength λ_p.
2. Population inversion along the amplifying medium. This involves, population density equations for lower level population ($N_1(r,\phi,z)$), upper level population ($N_2(r,\phi,z)$) and total doping population ($N_T(r,\phi)$).

The Equations can then be solved by using the standard fourth-order Runge-Kutta method given initial conditions for pump and signal power. Gains and noise figures for all signal modes may similarly be calculated.

The gain and noise performance of doped fiber amplifiers can be described by means of a set of coupled differential equations containing population and propagation equations. In order to determine the differential equations which form the ytterbium-doped fiber amplifier (YDFA) model, we need to consider a cylindrical coordinate system (r,ϕ,z) with the z-axis as the fiber axis. $N_T(r,\phi)$ is the ytterbium ions concentration in the transverse field, generally speaking a point function. At first, we ignore the ASE and we consider a photon beam at frequency $\nu_s = \frac{c}{\lambda_s}$ and signal intensity I_s.

Although the propagation and rate equations to solve for the case of single mode and multimode signals are similar. For this reason, we will split the model into single mode and multimode cases.

3.1.3 Single Mode Signal

Here we will discuss the propagation and rate equations when the signal is single mode. The propagation equation of signal intensity $I_s(z)$ at each fiber length z is provided by:

$$\frac{dI_s(z)}{dz} = [\sigma_{es}N_2 - \sigma_{as}N_1]\, I_s(z) \tag{3.1}$$

where absorption cross section σ_{as}, emission cross section σ_{es} and the intensity of the pump beam $I_p(z)$ with frequency $\nu_p = \frac{c}{\lambda_p}$ is also given by similar equation of (3.1). The intensity I_s of the transverse field corresponds to the magnitude of the Poynting vector of the fundamental mode of at the fiber wavelength (λ_s) 1064 nm. The optical power of the beam travelling along the fiber length of z is:

$$P_s(z) = \int_0^{2\pi}\int_0^{\infty} I_s(r,\phi,z)rdrd\phi \tag{3.2}$$

Since the functions of the modes do not depend on z, the intensity can be written as,

$$I_s(r,\phi,z) = P_s(z)i_s(r,\phi) \tag{3.3}$$

where i_s is the normalized optical intensity, corresponding to,

$$\int_0^{2\pi}\int_0^{\infty} i_s(r,\phi)rdrd\phi = 1 \tag{3.4}$$

The power propagation equation is thus obtained by using equations 3.1, 3.2 and 3.3, and by integrating over the transverse coordinate.

$$\begin{aligned}\frac{dP_s(z)}{dz} &= \sigma_{es}P_s(z)\int_0^{2\pi}\int_0^{\infty} i_s(r,\phi)N_2(r,\phi,z)rdrd\phi \\ &- \sigma_{as}P_s(z)\int_0^{2\pi}\int_0^{\infty} i_s(r,\phi)N_1(r,\phi,z)rdrd\phi \end{aligned} \tag{3.5}$$

The same process can be followed for the propagation equations of the pump and ASE powers, thus obtaining equations similar to (3.5). If then we associate these equations to those indicating the populations N_1 and N_2 as functions of the beam powers, we are able to calculate the amplifier parameters.

Assuming the ytterbium ions are uniformly distributed in a disk of radius b concentric to the core radius a, then integrals in equation (3.5) simplified. Furthermore, since the variations of the normalized intensities i_s and i_p in the doped region are very low, the population inversion is generally uniform along the doped fiber. Consequently, N_1 and N_2 only depend on z and can be taken out of the integrals in equation (3.5).

$$\begin{aligned}\frac{dP_s(z)}{dz} = \Big[&\sigma_{es}N_2(z)\int_0^{2\pi}\int_0^{b} i_s(r,\phi)rdrd\phi \\ &- \sigma_{as}N_1(z)\int_0^{2\pi}\int_0^{b} i_s(r,\phi)rdrd\phi\Big]P_s(z)\end{aligned} \tag{3.6}$$

The overlap integral, Γ_s, between the dopant and the mode at ν_s signal frequency is given by:

$$\Gamma_s = \int_0^{2\pi}\int_0^{b} i_s(r,\phi)rdrd\phi \tag{3.7}$$

Equation(3.5) can be simplified and finally written as:

$$\frac{dP_s(z)}{dz} = \Big[\sigma_{es}N_2(z) - \sigma_{as}N_1(z)\Big]\Gamma_s P_s(z) \tag{3.8}$$

It is useful to introduce two further parameters, the absorption coefficient $\alpha_s = \Gamma_s\sigma_{as}N_T$, and the gain coefficient $g_s = \Gamma_s\sigma_{es}N_T$. The two parameters are functions of the wavelength, their dimensions is inverse length (m^{-1}), and they describe the spectral characteristics of a doped fiber. They can be calculated directly, or after finding the overlap integral, the absorption cross sections, and the doping concentration. Equation (3.8) thus becomes,

$$\frac{dP_s(z)}{dz} = \left(g_s\frac{N_2(z)}{N_T} - \alpha_s\frac{N_1(z)}{N_T}\right)P_s(z) \tag{3.9}$$

Similarly, we can obtain the pump propagation equation, considering the stimulated emission cross-section being negligible in ytterbium,

$$\frac{dP_p^{\pm}(z)}{dz} = \pm\alpha_p\frac{N_1(z)}{N_T}P_p^{\pm}(z) \tag{3.10}$$

The superscript " + " refers to the co-propagating pump beam and the superscript " − " refers the counter propagating pump beam where,

$$\alpha_p = \Gamma_p \sigma_{ap} N_T$$
$$\Gamma_p = \int_0^{2\pi} \int_0^b i_p(r,\phi) r dr d\phi$$

Finding the ASE equation is a bit more complicated. To start with, ASE is not described by an intensity, but by a power spectral density $p(\nu)$, expressed in [W/Hz m^2]. Secondly, it is no longer possible to ignore the spontaneous emission, because without the spontaneous emission the ASE would not exist.

We can overcome the first problem by dividing the spectrum into smaller frequency intervals Δv, each centered at a different frequency v_j. We then substitute the spectral density with a sequence of intensities I_j of the type [56],

$$I_j = \int_{v_j - \frac{\Delta v}{2}}^{v_j + \frac{\Delta v}{2}} p(v) dv$$

each centered in v_j. The situation is thus similar to several signal beams propagating at the same time. The only difference is that for each j there is both a co-propagating and a counter-propagating ASE beam. As for the second aspect, spontaneous emissions, it will not be treated in the present discussion because it would require the equations of quantum electro-dynamics. We will thus only include the final result, which consists in adding to the propagation equations a term proportional to $mhv_j \Delta v_j$, where m indicates the number of modes which can propagate through the guide. In a single mode fiber m is 2, because its fundamental mode shows two polarizations. Thus ASE will be given by equation (3.11) [56]:

$$\frac{dP_j^{\pm}(z)}{dz} = \pm \left(g_j \frac{N_2(z)}{N_T} - \alpha_j \frac{N_1(z)}{N_T} \right) P_j(z) \pm g_j \frac{N_2(z)}{N_T} 2hv_j \Delta v_j \tag{3.11}$$

The powers of the co-propagating beams are assigned at $z = 0$, whereas the powers of the counter-propagating beams at $z = L$, where L is the length of the doped fiber. Notice that the co-propagating ASE is zero at $z = 0$, while the counter-propagating ASE is zero at $z = L$.

In order to complete the doped fiber amplifier model it is necessary to formulate the equations describing the populations, N_1, N_2 and N_T as functions of the powers of the signal, pump and ASE beams propagating through the fiber. These equations are known as population equations. The population density of the metastable state is given as [56]:

$$N_2(r,\phi,z) = N_T(r,\phi) \frac{\tau \left(\sigma_{as} \frac{I_s}{hv_s} + \sigma_p \frac{I_p}{hv_p} \right)}{1 + \tau \left[(\sigma_{as} + \sigma_{es}) \frac{I_s}{hv_s} + \sigma_p \frac{I_p}{hv_p} \right]} \tag{3.12}$$

where τ is the lifetime of the excited state and corresponds to the inverse of the spontaneous emission rate, and σ_{as}, σ_{ap} are absorption cross sections of signal and pump respectively. I_s and I_p are signal and pump intensities with optical frequency (ν_s) of signal at λ_s, and pump frequency (ν_p) of pump at λ_p. Finally the population in the ground state can be found through the ion conservation equation.

$$N_1(r,\phi,z) = N_T(r,\phi) - N_2(r,\phi,z)$$

By means of integration equation (3.12) over the transverse plane and thanks to the approximations introduced for propagation equations we finally obtain,

$$\frac{N_2(z)}{N_T} = \frac{\sum_k \tau\alpha_k \frac{P_k(z)}{h\nu_k \pi b^2 N_T}}{1 + \sum_k \tau(\alpha_k + g_k)\frac{P_k(z)}{h\nu_k \pi b^2 N_T}} \tag{3.13}$$

where the summations include all the co and counter-propagating signal, pump, and ASE beams. Apart from some exceptions, these equations cannot be solved analytically, so that it is necessary to solve them numerically.

3.1.4 Multimode Signal

In our previous discussion we have seen the propagation equations for single mode signal. Following the same procedures, we will discuss under this section when the spatial signal is multimode. The solver is based on the spatial model, describing the propagation of guided modes by dividing the fiber into constant discrete steps for applying a numerical solver to the amplifier propagation equations, which are assembled according to the number of propagating modes of signal and pump. Assuming loss to be negligible in the doped fiber, the evolution of power $\mathrm{P_{sl}}$ of mode l of signal (or pump) s is given by equation (3.14) [56]:

$$\frac{\Delta P_{sl}}{\Delta z} = \left(g_{sl}\frac{N_2(z_i)}{N_T} - \alpha_{sl}\frac{N_1(z_i)}{N_T} \right) P_{sl}(z_i) \tag{3.14}$$

and solved at each step $\mathrm{z_i}$ by the variable coefficient linear multistep Adams method. N_T is the total population of doping ions, calculated by pump absorption measurement. The population densities of doped atoms N_1 and N_2 at the fundamental and metastable state (lower and upper levels) are then calculated from the population rate equations of the active medium, whereas absorption (α_{sl}) and gain (g_{sl}) coefficients are determined from experimentally given ytterbium cross-sections (absorption σ_{asl}, and emission σ_{esl} cross-sections), overlap integral of signal Γ_{sl} and total dopant concentration N_T [56].

$$\alpha_{sl} = \Gamma_{sl}\sigma_{asl}N_T \tag{3.15}$$

$$g_{sl} = \Gamma_{sl}\sigma_{esl}N_T \tag{3.16}$$

By using the model field distributions we can determine the signal overlap integrals Γ_{sl} with the doped region S of the fiber core as follows [53]:

$$\Gamma_{sl} = \iint_S i_{sl}(x,y)\,dx\,dy \tag{3.17}$$

where $i_{sl}(x,y)$ is the signal mode normalized intensity distribution. This is simplified for the pump as the strong air-cladding confinement gives a highly multimodal pump distribution so that the pump overlap can be approximated by the ratio of the active core and inner cladding areas.

In WDM systems, the input to the doped fiber amplifier comprises M signal beams, each with a different frequency ν_{sk} and a different power P_{sk} with k = 1,..., M.

We will thus obtain M number of different equations given by equation(3.18) below.

$$\frac{dP_{sk}(z)}{dz} = \left(g_{sk}\frac{N_2(z)}{N_T} - \alpha_{sk}\frac{N_1(z)}{N_T} \right) P_{sk}(z) \tag{3.18}$$

3.1.5 Core and Cladding Pumping

In the core-pumping scheme, and for a single mode fiber, the pumping light source is single mode and launched to the single mode core to amplify the signal, and the amplified signal is also single mode. Core pumping in multicore optical amplifier uses multiple pumping light in order to launch the amplification source light into each core individually. In other words, core pumping injects multiple source light into each core individually. Both the pump and signal lights are multiplexed with a wavelength division multiplexing (WDM) coupler and launched into an erbium-doped core through a fan-in (FI), and the amplified signals are output through a fan-out (FO). The benefits of core pumping includes, high pump efficiency and applicability of components and high-speed control used in conventional single-core EDFA. Reducing size, cost, and power consumption are the main challenges of core pumping. The refractive index of the polymer coating around the cladding is set higher than that of the cladding, such that light guidance in the cladding is prevented.

In the cladding-pumping scheme, the pumping light source is multimode and launched into the cladding (referred to as the first cladding). In other words, cladding pumping injects one source light into the cladding region. The first cladding is further surrounded by the second cladding with a lower refractive index, such that the pump launched to the first cladding is guided by total-internal reflection. The pump interacts with the signal when the light crosses the core, and the signal maintains its single modeness during amplification, because the signal core is single mode. The cladding pumping scheme is expected to reduce the power consumption compared with that in the core pumping scheme. The fibers used for cladding pumping are often called as double-clad fibers, as there are two claddings (first and second cladding). Improving pumping efficiency, developing pump/signal combiner, and achieving high-speed control are the challenges of cladding pumping.

3.1.6 Gain and Optimum Length

The propagation equation for the signal can be used to derive a convenient relationship for the signal gain. The signal gain can be expressed in terms of the average inversion of the ytterbium ions along the fiber. Assuming zero background loss, and integrating signal propagation equation yields wavelength and position dependent gain. By integrating equation 3.8, the total gain G for a YDFA of length L is obtained using [3][9],

$$G = \exp\left[\int_0^L (N_2(z)\sigma_{es} - N_1(z)\sigma_{as})\Gamma_s dz \right] \tag{3.19}$$

Equation (3.19) suggests that the gain is a complex function of the shape of the inversion along the length of the fiber. The gain can be related simply to the average inversion, by defining upper and lower state population as,

$$\bar{N_2} = \frac{1}{L}\int_0^L N_2(z)dz \tag{3.20}$$

$$\bar{N}_1 = \frac{1}{L}\int_0^L N_1(z)dz \tag{3.21}$$

Equation (3.19) can then be simplified to,

$$G = \exp\left[(\bar{N}_2\sigma_{es} - \bar{N}_1\sigma_{as})\Gamma_s L\right] \tag{3.22}$$

This shows that the signal gain after traversal of the fiber is dependent only on the average inversion of the ytterbium ions in the fiber, and does not depend on the details of the shape of the inversion as a function of position along the fiber length. The ASE, on the other hand, will depend on the detailed shape of the inversion, due to the local nature of ASE generation. This also implies that the figure will depend on the profile of the inversion, and not just the average inversion.

Population density varies considerably along the fiber length due to the effect of gradual pump absorption. In doped fiber amplifiers, fiber may thus be strongly absorbent or they can be active media. Hence, it is possible to identify an optimum length of the doped fiber to maximise the gain. Let us consider the case of a single signal, a co-propagating pump and no ASE. On the input side of the amplifier, the high pump power allows an almost total population inversion, so that the signal power increases exponentially. As the power transfers from the pump to the signal, P_p decreases, while P_s increases, thus determining a gradual reduction of the population inversion and, consequently, of P_s growth rate. Beyond a certain position, the absence of population inversion makes the material absorbent for the signal wavelengths. The distance between the input port and the the fiber section at which the population inversion ceases is called optimum length, L_{opt}, of the amplifier. If $L = L_{opt}$ and the parameters are constant, the amplifier gain is maximised.

$$G = \frac{P_s(L)}{P_s(0)}$$

Both the optimum length and G increase if the input pump power $P_p(0)$ increases. The higher $P_p(0)$ is the longer the length of the fiber in which the pump is able to create a population inversion.

Gain in doped fiber amplifier is achieved due to population inversion of dopant ions. As there are limited number of dopant ions, increasing pumping power to a level at which all the dopant are excited will not increase the population of the excited level any further and the gain saturation will take place. As the input signal power increases, inversion level reduces and there will be no further amplification. The maximum output power beyond which no amplification occurs is called gain saturation.

3.1.7 Simulation Results

An active multimode fiber of 100/350 µm core and single cladding diameter with parabolic graded-index profile is considered. Assuming the doped region has the same size as the core (core fully doped), fundamental and two high order modes power evolution along 3m fiber length can then be visualized from figures 3.3 and 3.4, by varying the signal powers with respect of the fundamental mode. Table (3.2) below shows the main parameters and their corresponding values used in the simulation. Core pumping configuration for single cladding fiber is considered.

Parameters	**Value**	**Parameters**	**Value**
$a(\mu m)$	50	$D_{clad}(\mu m)$	350
$\sigma_{as}(m^2)$	5.0×10^{-27}	NA	0.216
$\sigma_{es}(m^2)$	2.89855×10^{-25}	$\tau(ms)$	1
$\sigma_{ap}(m^2)$	2.358×10^{-24}	$\alpha_p(dB/m)$	200
$\sigma_{ep}(m^2)$	2.358×10^{-24}	Length (m)	3
$N_T(ions/m^3)$	1.95807×10^{25}	λ_s (nm)	1064
λ_p (nm)	976		

Table 3.2: Parameters used in the modelling and numerical simulation.

To approximate the graded-index fiber profile with Comsol Multiphysics, we used concentric circles and determined refractive index n(r) as a function of radial distance for each circle. As it can be observed from figure (3.3a), the power in the fundamental mode (LP_{01}) is higher than that of high order modes (LP_{11} and LP_{21}) in the simulation. In the same figure (3.3a) 40dBm pump, 30dBm fundamental mode, 25dBm and 20dBm high order modes power are utilized. In this model as it's stated at the beginning, factors that can not be neglected in experiment like Brillouin scattering, Raman scattering and others at high input power are not considered. The reason for this is partly, we considered a short fiber amplifier length which can compensate low input power in long fiber amplifiers, and a simplified models with spatial dependency are implemented. Similarly, in figure (3.3b) equal amount of powers for fundamental and high order modes is set. In general, from figure (3.3) it could be understood that, the power of high order modes affect the signal amplification or gain of the fundamental mode. Setting the power of high order modes equal or higher than the fundamental modes as shown in figures 3.3b and 3.4 respectively, reduces the gain of the signal, which is due to the gain competition of high order modes. Along the propagation distance the power of fundament and high order modes, ceases amplification and stays constant after the point where the pump power is totally absorbed. The power stays stable and constant as no loss is considered for this model, and also due to material property of ytterbium ion, which keeps the signal from degradation for certain fiber length.

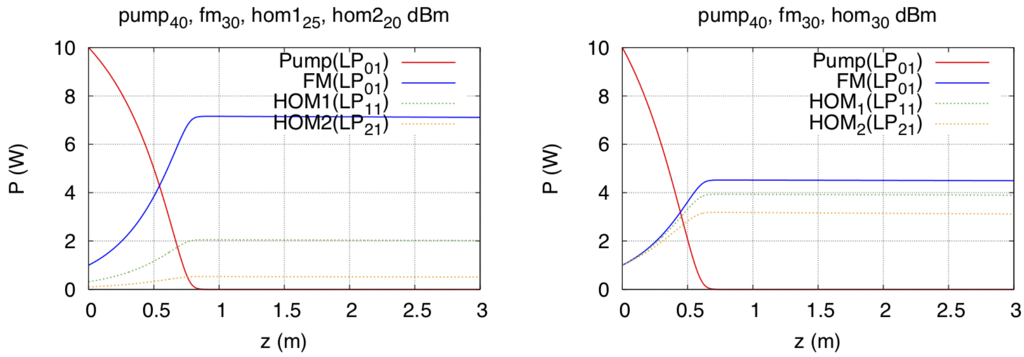

(a) **(b)**

Figure 3.3: Amplification of signal power along fiber length: (a) Higher fundamental modes (LP_{01}) power than high order modes (b) Power of fundamental mode (LP_{01}) the same as other high-order modes (LP_{11}, and LP_{21})

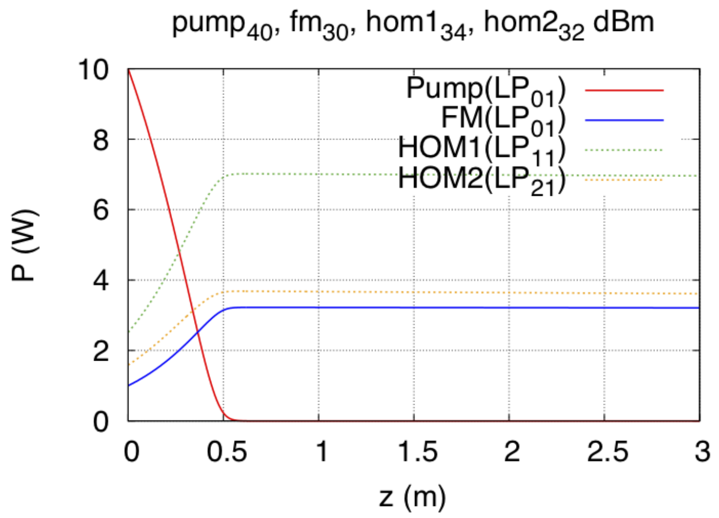

Figure 3.4: Amplification of signal power with 40dBm pump power, high-order modes have higher power than the fundamental mode

In figure (3.4) the power of high order modes is set to be higher than the fundamental mode. In normal conditions the power of fundamental mode is higher than high order modes, and preferentially amplified. In the figure the power of the pump signal is 40dBm, the power of fundamental mode is 30dBm, the first high order mode (HOM1 LP_{11}) is 34dBm, and the second high order mode ((HOM1 LP_{21})) is 32dBm. The amplification of the fundamental mode (blue color plot) along 3m fiber length is further reduced than the previous cases we have seen in figure (3.3).

3.2 Chapter Summary

Ytterbium-doped fiber amplifier modelling equations and techniques are presented under this chapter. In the fiber amplifier modelling procedures of this chapter, first the fiber geometry is defined, and thoroughly meshed, then the wave equation is solved by using Comsol Multiphysics. Parameters like effective refractive index, and modal intensity profiles are extracted from Comsol which are essential in determining overlap integrals, pump and signal propagations along the fiber length. In this fiber amplifier model the dopant is uniformly distributed inside the fiber, and core or cladding pumping could be applied. Rate and propagation equations are exploited to study the power evolution of pump, fundamental mode and other few high order modes. The populations at excited and ground state levels are determined using the rate equation given by equation (3.12), then signal propagation equation (3.9) and pump propagation equation (3.10) are solved to compute the amplification situation of signal (fundamental mode) along the fiber. Equation(3.18) is manipulated when many modes are considered, to determine the signal power evolution.

We varied the power of each mode and pump, to investigate the gain competition inside the fiber amplifier. When the input power of high order modes is equal or larger than that of the fundamental mode (LP_{01}), the overall gain is reduced and spatial beam close to the fundamental mode is not expected at the output end as shown in figure 3.4. As we are dealing with multimode fiber amplifier that support large number of modes, this model is not very suitable to excite a number of guided modes. In addition, this model is limited as it does not include factors that affects our signal propagation(like nonlinearity, gain saturation and etc.), and also different dopant profiles. For these and other reasons, we considered the modelling techniques in this chapter, which includes the population at higher and lower energy level, the signal and pump power propagation, as well as the signal gain along the fiber length as stepping-stone to look for other more flexible and powerful models.

Chapter 4

Rate and Propagation Equations

Silica fibers have lower losses($\alpha \approx 0.2$ dB/km) in the wavelength region close to $1.55\mu m$ or in C (1530 - 1565 nm) and L (1565 - 1625 nm) bands. Though the loss is small for a shorter span, the accumulated attenuation of the optical signal is higher over a longer fiber distance. For this reason, the development of loss compensation technique is vital to enable long-haul transmission successfully. Yb doped fibers are the results of important technologies today that can provide high optical gain and that are largely used to build high energy lasers for industrial applications.

When rare-earth elements are embedded in silica or other glass fibers, they become triply ionized. Many different rare-earth ions, such as erbium, holmium, samarium, thulium, neodymium and ytterbium, can be used to make fiber amplifiers that operate at wavelengths covering a wide range, from visible to infrared. Amplifier characteristics, such as the operating wavelength and the gain bandwidth, are characterized by dopants rather than by the fiber, which plays the role of a host medium. In this paper we have considered Yb-doped double clad fibers amplifiers, mainly due to their interesting applications for broad gain bandwidth with excellent beam quality, unique simple energy level structure, high pump absorption and efficiency [12]. Although ytterbium rare-earth dopants have efficient performance, low quantum defects, and interesting spectroscopic characteristics, the capacity of generating high powers labels them very attractive in which the output power of 10-50 kW at continuous wave single mode, multimode schemes has been recently reported. Ytterbium (Yb^{3+})-doped materials have been widely used for high efficiency high energy laser sources at the 1μm wavelength region because of their very low quantum defect and the unique energy level structure of Yb^{3+}. The observation reported in [67] is interesting and here is reported verbatim: "it has been generally recognized that these ion-ion interaction processes have very little influence on the operation of ytterbium-doped fiber lasers at low and moderate power levels. However, our recent study shows that the performance of $Yb^{3+}-$doped fiber amplifiers operating at low power levels still influenced by the ion-ion interaction processes due to the large amount of population at the upper laser level $^2F_{5/2}$".

4.1 Spectroscopic properties of Yb-doped silica glass

The spectrum of a rare earth doped fiber laser and amplifier ranges from visible (400-780nm) to mid-infrared (2-$5\mu m$), and includes almost all of the interesting wavelengths for optical fiber communication, biomedical, and aerospace applications. All rare–earth doped fiber amplifiers intensify the seed signal light through stimulated emission. The stimulated emission of ytterbium ion involves transitions between Stark levels of $^2F_{5/2}$ and $^2F_{7/2}$ electronic states called manifolds [39]. The dynamics of emission and absorption process of doping ions inside the host material is described by the rate equations. This can be achieved by making use of the dopant atomic energy structure as well as spectroscopic properties. The McCumber theory determines the relation between the absorption and emission cross sections for two energy–level gain media, which is given by equation (4.1) [42]

$$\sigma_e(\nu) = \sigma_a(\nu) exp\left(\frac{\epsilon(T) - h\nu}{K_B T}\right) \tag{4.1}$$

where σ_a and σ_e are the absorption and emission cross sections, h is Planck constant, ν is the frequency of light, K$_B$ is the Boltzmann constant, T is the absolute temperature in Kelvin, and $\epsilon(T)$ is the mean transition energy between two manifolds. The mean transition energy $\epsilon(T)$ at temperature T do not depend on the optical frequency, and can be determined from the energies of the single Stark levels. $\epsilon(T)$ for ytterbium doped gain mediums is often close to the photon energy of the zero–phonon, that is, the transition between the lowest sublevels of both manifolds. Emission and absorption cross sections are equal ($\sigma_e = \sigma_a$), at a wavelength of 975 nm, where the $\epsilon(T)$ = 1.27eV. Based on the McCumber investigation, the emission cross section and the radiative lifetime are related by equation (4.2)

$$\frac{1}{\tau} = \frac{8\pi n^2}{c^2} \int \nu^2 \sigma_e(v) d\nu \tag{4.2}$$

where n is the refractive index, τ is the lifetime of atoms at excited state level, and c is the speed of light in vacuum.

Figure 4.1 shows a model for the Yb^{3+} ions energy–level structure, consisting of two manifolds: a ground state $^2F_{7/2}$ (with four Stark levels denoted as L$_0$, L$_1$, L$_2$, and L$_3$) and a well–separated excited state $^2F_{5/2}$ (with three Stark levels labelled as U$_0$, U$_1$, and U$_2$), approximately placed at $10^4 cm^{-1}$ above the ground level. As a result, at both the pump and laser wavelengths, there is no excited state absorption (ESA) [12]. Furthermore, concentration quenching and nonradiative decay via multiphonon emission from $^2F_{5/2}$ are prevented due to this high energy gap.

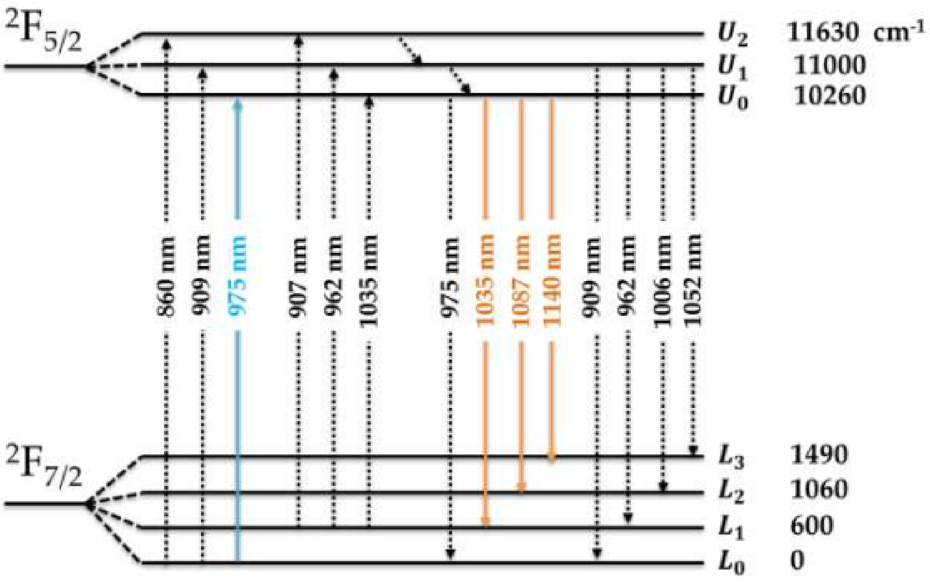

Figure 4.1: Energy level diagram of ytterbium silica glass [12]

The absorption and emission of the pump is the first transition between the two ytterbium manifolds. Subsequently, the absorption and stimulated emission of the signal, along with the spontaneous decay from the manifold $^2F_{5/2}$ appear concurrently. The spectroscopic diagram of figure 4.2 shows the absorption and stimulated emission cross sections of ytterbium doped silica glass optical fibers. The zero line transition between the excited state (U_0) and the lowest energy level of the ground state (L_0) in the manifold is represented by the absorption (fluorescence) peak at 975 nm, which is shown by point A in figure 4.2. The operation of a laser at a wavelength of 975nm is the three level process which is due to an emission to the lowest Stark level. The absorption peak at a shorter wavelength (point B in the plot) corresponds to a transition from the ground level L_0 to either of the excited level U_1 or U_2. The absorption peak at longer wavelength (point C in figure 4.2) is attributed to the transition from level L_1 which can produce re-absorption and leads to higher thresholds in the ytterbium laser systems operating at around 1μm.

Moreover, the emission spectrum peak (D) correlates to the energy transfer from level U_0 to the levels L_1, L_2, and L_3, whereas the one at (E) belongs to the transition from level U_1, creating weak emissions around 900 nm. The broad absorption spectrum of ytterbium ions enables the easy configuration of the pump wavelength. Based on the demand of the laser systems, the laser signal wavelength can be configured in the range 970 nm - 1200 nm because of the wide emission spectrum of ytterbium ions.

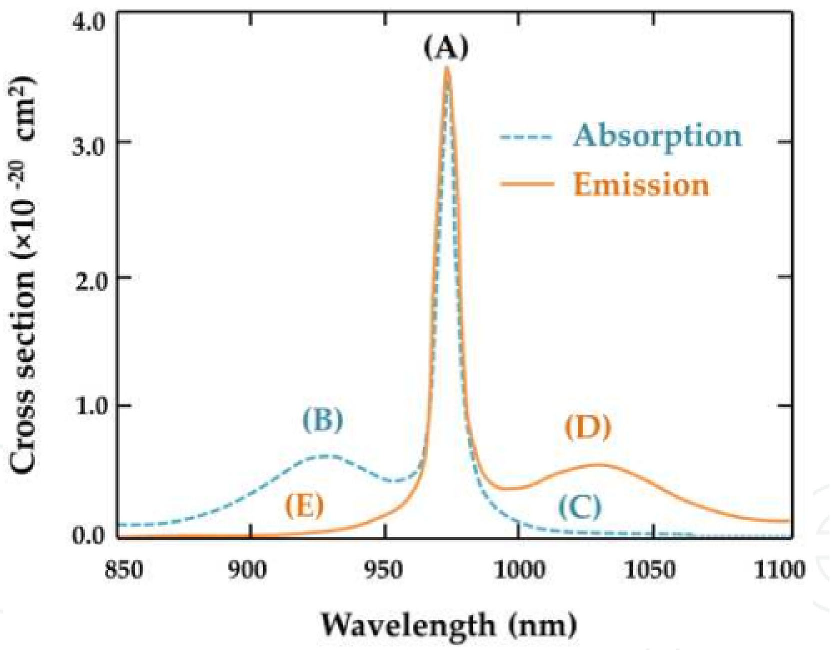

Figure 4.2: Absorption and emission spectra of ytterbium ions in germano silicate host [12]

4.2 Rate Equations

The dynamics of energy level populations in laser gain media like rare-earth-doped crystals or fibers are often modelled using a system of rate equations. These are differential equations, describing the temporal evolution of level populations under the effect of optically induced and non-radiative transitions. The rate equations are typically introduced here with the definition of the relevant parameters for the quasi three energy level structures of the rare-earth elements. The fourth order Runge-Kutta method will be implemented, by neglecting the effects of ASE (Amplified Spontaneous Emission) parasitic noises in our numerical simulations.

The rare-earth dopants determine the amplifier characteristics, comprising the operating wavelength and the gain bandwidth. It is the dopant that characterise the amplifier properties rather than the host medium. The performance of fiber amplifiers also relays on the rates of radiative and nonradiative decays that are caused by mechanisms related to lattice vibrations, cooperative up conversion to higher levels, and ion–ion interactions. Fiber amplifiers delivers high optical gains at moderate pump power levels over a relatively large spectral bandwidths.This makes the fiber amplifiers a preferable entity for many applications like signal processing, material processing, and telecommunications.

For active multimode fiber doped with ytterbium rare-earth element, the rate and propagation equations provide population density at each energy level, signal and pump power evolution across the fiber propagation direction. Our assumption here is that, the rare-earth ions are only doped in fiber core and pump laser will distribute homogeneously in fiber core cross section which is cladding pumping. We follow the standard treatment where the electronic levels are modelled as a two-level gain system, with N_1 and N_2 representing, respectively, the fractional lower and upper level populations. With steady state two-level rate equation given by (4.4), the upper level population fraction $N_2(x,y,z)$ of fiber cross section can be expressed as follows in Cartesian coordinates [59] [64]:

$$N_2(x,y,z) = N_T(x,y,z)\frac{I_p(z)\lambda_p\sigma_{ap} + \lambda_s\sigma_{as}\sum_k I_s^k(x,y,z)}{\frac{hc}{\tau} + I_p(z)\lambda_p(\sigma_{ap}+\sigma_{ep}) + \lambda_s(\sigma_{as}^s+\sigma_{es})\sum_k I_s^k(x,y,z)} \tag{4.3}$$

where h is Planck's constant, c is velocity of light in vacuum, τ is upper-level lifetime of Yb-ions representing the spontaneous decay from the upper excited level to the lower ground state, I_p is intensity of pump laser, I_s^k is intensity distribution of k-th eigenmode, λ_p and λ_s are pump and signal wavelength respectively, σ_a and σ_e are absorption and emission cross sections (m^2) of Yb-ions and superscript p and s means pump and signal, respectively. For steady state condition, the populations are time invariant [28] and the doping profile of the ytterbium ions $N_T(x,y,z)$ satisfies the equation $N_T(x,y,z) = N_1(x,y,z) + N_2(x,y,z)$ [28].

$$\frac{d}{dt}N_i(x,y,z) = 0 \quad (i = 1,2) \tag{4.4}$$

Here intensity distribution for uniform pump field distribution across the cladding (cladding pumping), the pump intensity could be expressed by equation 4.5 [1]. Where $P_{pump}(z)$ is pump power and R_{clad} is inner cladding radius.

$$I_p(z) = \frac{P_{pump}(z)}{\pi R_{clad}^2} \tag{4.5}$$

In population equation given by equation 4.3 above the intensity distribution of eigenmodes (I_s^k) at signal wavelength could be obtained from the guided field [35] as:

$$I_s(x,y,z) = \left|E_g(x,y,z)\right|^2$$

where, $\left|E_g(x,y,z)\right|^2$ is guided field of eigenmodes which is explored in chapter 1. Normalized modal intensity distribution $i_n(x,y)$ of the n-th mode in the fiber's transverse plane could be provided as the ratio of modal intensity distribution and modal power in the longitudinal direction [25].

$$\begin{aligned} & i_n(x,y) = I_n(x,y,z)/P_n(z) \\ & P_n(z) = \int_{-\infty}^{+\infty}\int_{-\infty}^{+\infty} I_n(x,y,z)dxdy \\ & \int_{-\infty}^{+\infty}\int_{-\infty}^{+\infty} i_n(x,y)dxdy = 1 \end{aligned} \tag{4.6}$$

where $P_n(z)$ is the power of the n^{th} mode, and it is equivalent to the integration of the light intensity $I_n(x,y,z)$ over the transverse coordinates as given by equation (4.6). Intensity of pump in the case of core pumping is not uniform across the transverse direction and hence equation (4.5) may not be valid under this situations. We need to modify equation (4.3) for the case of core pumping and the population fraction at the higher level will be given by equation (4.7) below. In this case the pump signal absorption is higher and as a result the pump power is absorbed in a short segment of fiber length.

$$N_2(x,y,z) = N_T(x,y,z)\frac{\lambda_p\sigma_{ap}\sum_k I_p^k(x,y,z) + \lambda_s\sigma_{as}\sum_k I_s^k(x,y,z)}{\frac{hc}{\tau} + \lambda_p(\sigma_{ap}+\sigma_{ep})\sum_k I_p^k(x,y,z) + \lambda_s(\sigma_{as}+\sigma_{es})\sum_k I_s^k(x,y,z)} \tag{4.7}$$

In the situations where the dopant distribution is non-uniform inside the fiber core the variations of rare-earth dopant is given by equation (4.8). For parabolic dopant profile, the dopant concentration varies as a function of radial distance from the fiber core where is nominal (maximum)[59][40], whereas zero outside the core (in cladding), and its determined by using equation (4.8). Figure 4.3 below shows parabolic dopant concentration where the nominal is 2x10^{25} (ions/m^3), and reduced from the core to cladding areas where its zero outside the fiber core diameter.

$$\begin{aligned} N(x,y) &= N_0\left(1-\frac{r^2}{a^2}\right), \quad r < a \\ &= 0, \quad r > a \end{aligned} \tag{4.8}$$

where $r^2 = x^2 + y^2$ and N_0 is the maximum doping concentration at the core center and reduces towards the fiber cladding.

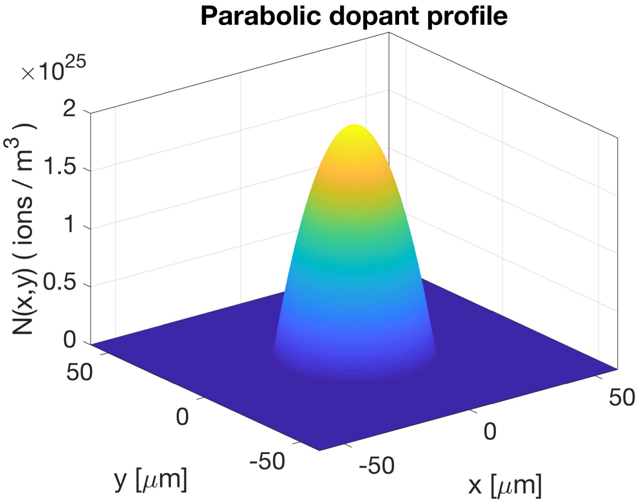

Figure 4.3: Dopant distribution inside the fiber core for parabolic dopant profile

The gain coefficient in units of per meter g(x,y,z) (m^{-1}) in core cross section is related to the population of the rare-earth ions, the emission and absorption cross sections at signal wavelength and is provided by equation (4.9) [59][64]. The gain coefficient is a parameter introduced by emission and absorption cross sections, and is used to determine the gain of fiber amplifier per unit distance.

$$g(x,y,z) = (\sigma_{as} + \sigma_{es})N_2(x,y,z) - \sigma_{as}N_T(x,y,z) \tag{4.9}$$

Once we found the populations at lower or excited levels using the rate equations we have seen so far, its time to determine the evolution of power (signal or pump) along the evolution direction using propagation equations for fiber lasers and amplifiers. From the propagation equations we can obtain the variation of pump laser, as well as the signal modes at each segment of fiber length [8] along the propagation direction. Doped fiber amplifiers could be pumped in the forward or backward direction, the propagation equations are used to show the evolution of the pump power along the fiber length. The differential equations for forward pump power propagation, $P_p^+(z)$, and backward pump power propagation, $P_p^-(z)$, are given by the following equations [49]:

$$+\frac{dP_p^+(z)}{dz} = \Gamma_p\left(\sigma_p^{ae}N_2(z) - \sigma_{ap}N_T\right)P_p^+(z) - \alpha_p P_p^+(z) \tag{4.10}$$

$$-\frac{dP_p^-(z)}{dz} = \Gamma_p\left(\sigma_p^{ae}N_2(z) - \sigma_{ap}N_T\right)P_p^-(z) - \alpha_p P_p^-(z) \tag{4.11}$$

Similarly, the evolution equations for forward signal power propagation, $P_s^+(z)$, and backward signal power propagation, $P_s^-(z)$, are also given by:

$$+\frac{dP_s^+(z)}{dz} = \Gamma_s\left(\sigma_s^{ae}N_2(z) - \sigma_{as}N_T\right)P_s^+(z) - \alpha_s P_s^+(z) \tag{4.12}$$

$$-\frac{dP_s^-(z)}{dz} = \Gamma_s\left(\sigma_s^{ae}N_2(z) - \sigma_{as}N_T\right)P_s^-(z) - \alpha_s P_s^-(z) \tag{4.13}$$

where N_T is the total Yb^{3+}concentration, which is assumed constant along the fiber laser, α_s and α_p are background absorptions, σ_{as} (σ_{ap}) is the absorption cross section at the signal (pump) wavelength shown in figure 4.2, σ_{es} (σ_{ep}) is the emission cross section at signal (pump) wavelength, $\sigma_p^{ae} = \sigma_{ap} + \sigma_{ep}$, and $\sigma_s^{ae} = \sigma_{as} + \sigma_{es}$. The fraction of pump power that is coupled to the doped core of the gain fiber is represented by Γ_p. Γ_p can be approximated as the ratio of the doped core area to the area of the inner cladding, in a double-cladding configuration, where the pump mode is fully scrambled. Similarly, Γ_s is the fraction of the signal power that overlaps the doped core area.

Parameters	**Value**	**Parameters**	**Value**
$a(\mu m)$	26	$\lambda_s(nm)$	1064
$R_{clad}(\mu m)$	150	$\lambda_p(nm)$	976
$FWHM(\mu m)$	20	$P_{pump}(W)$	10
$Length(m)$	2	$\tau(ms)$	1
$h(m^2kg/s)$	6.626×10^{-34}	n_{clad}	1.45
$\sigma_{as}(m^2)$	5.0×10^{-27}	$N_0(ions/m^3)$	9.0×10^{25}
$\sigma_{es}(m^2)$	2.8985×10^{-25}	n_{core}	1.467
$\sigma_{ep}(m^2)$	2.358×10^{-24}	$c(m/s)$	3.0×10^{8}
$\sigma_{ap}(m^2)$	2.358×10^{-24}		

Table 4.1: Parameters and respective values used in numerical simulations [49] [62]

For continuous wave (CW) bulk lasers, the upper manifold populations ($N_2(z)$) is determined by equation (4.14) as provided by [29]:

$$\frac{N_2(z)}{N_T} = \frac{\frac{\Gamma_p\sigma_{ap}(P_p^+(z)+P_p^-(z))}{h\nu_p A} + \frac{\Gamma_s\sigma_{as}(P_s^+(z)+P_s^-(z))}{h\nu_s A}}{\frac{\Gamma_p\sigma_p^{ae}(P_p^+(z)+P_p^-(z))}{h\nu_p A} + \frac{1}{\tau} + \frac{\Gamma_s\sigma_s^{ae}(P_s^+(z)+P_s^-(z))}{h\nu_s A}} \tag{4.14}$$

where $\sigma_p^{ae} = \sigma_{ap} + \sigma_{ep}$, $\sigma_s^{ae} = \sigma_{as} + \sigma_{es}$. Equation (4.14) describes the variation of the upper-level population density of the Yb^{3+} ions along the fiber through its dependence on the z-varying pump and signal powers. The differential equations for forward and backward pump and signal propagation equations are given by equations (4.10) and (4.13).

Pump and signal power propagations given by equations (4.11) and (4.13) could be solved using the fourth-order Runge–Kutta method and shooting algorithm, given initial boundary conditions. Equations (4.11) and (4.13) are resolved by a two-point boundary problem, which are the system of n first-order differential equations missing some boundary values [36]. There are many numerical algorithms for solving two-point boundary value problem such as shooting algorithm. Shooting method is the most commonly used algorithm, it begins from a guessed initial values and treats the problem as an initial value problem which can be solved by Runge-Kutta. When the initial guessed value is not reasonable, the initial guessed value can be corrected based on the relative error between the truth value and the guessed value by means of the different convergence algorithms until the boundary conditions are satisfied. Whereas the shooting algorithm must generally know the initial or terminal value, the laser powers at the two ends are unknown for the high-power fiber laser system and we only know the relation between them. Generally speaking, a shooting algorithm applicable to the two-point boundary value problem of a set of differential equations consists of three parts, namely, the determination of accurate initial guesses, a correction mechanism for the improvement of the initial guesses, and a numerical integration procedure [24]. For the numerical integration, any computational method can be used as long as it performs the integration accurately. The Runge–Kutta method with adaptive step size is used in this work. In general, the initial guesses and their correction mechanism are crucial for a shooting algorithm to converge quickly and stably.

The population N_1 at the ground state is higher, and the population N_2 at the excite state is zero before applying the pump power. When the active medium is pumped, the populations are excited to the upper energy level or population inversion takes place. Here it should be noted that even if N_1 is larger than N_2, as there are populations at a higher energy level, there is a signal amplification by stimulated emission. In addition, when the pump power is absorbed along the fiber length, the populations at excited state drop to the ground level and the total population N_T is the same as N_1 as it can be seen from figure 4.4b. At this point there is no signal amplification, and the amplified signal will also decrease due to absorptions. Furthermore, from equation (4.9) the gain is proportional to $\sigma_{es}N_2 - \sigma_{as}N_1$ and since σ_{es} is much larger than σ_{as}, the gain can be positive even if N_2 is smaller than N_1.

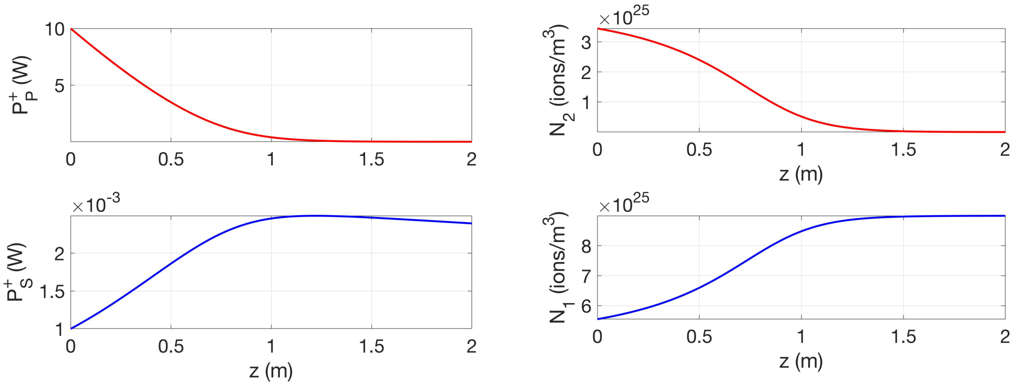

(a) Pump and signal powers **(b)** Populations N_2 and N_1 in forward pump

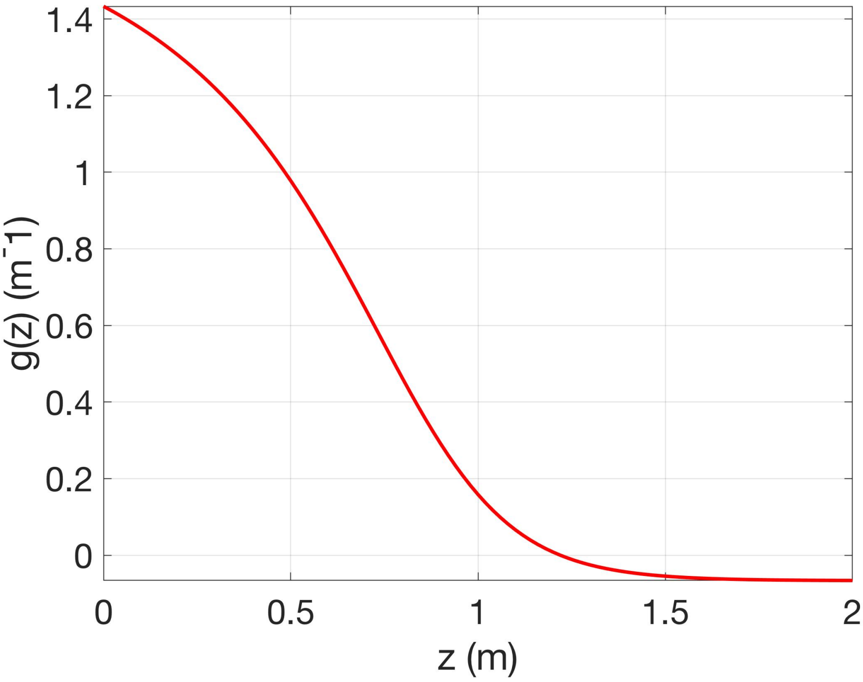

(c) Gain coefficient in forward pump

Figure 4.4: Signals, population and gain coefficient in forward pumping.

The solution of the propagation equations provided by (4.10) and (4.12) for pump and signal propagation along 2m fiber length are plotted in figure 4.4. A forward propagating 10W pump power, 1mW signal power, with fiber mode distribution should be used. Similarly populations of ytterbium ions at higher and ground levels, and gain coefficient are depicted in figure 4.4b, and 4.4c respectively. Its could be observed from figure 4.4a, that as the pump power is depleted after 1m of fiber length, the signal power ceases amplification after the same fiber distance. In other words, after 1m of fiber length the population at excited state (N_2) is depleted, and populations at ground layer are maximized, which indicates there is no amplification via stimulated emission.

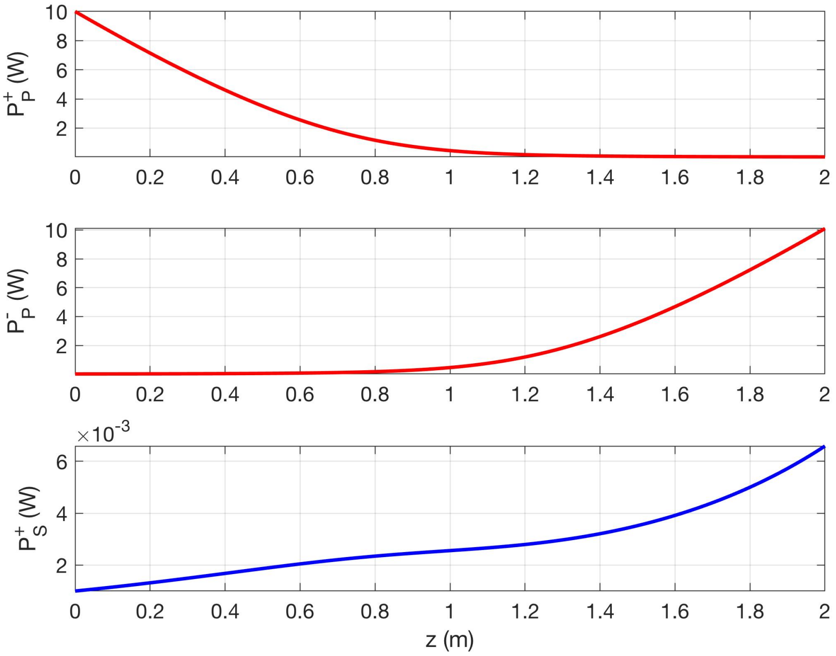

(a) Pump and signal powers

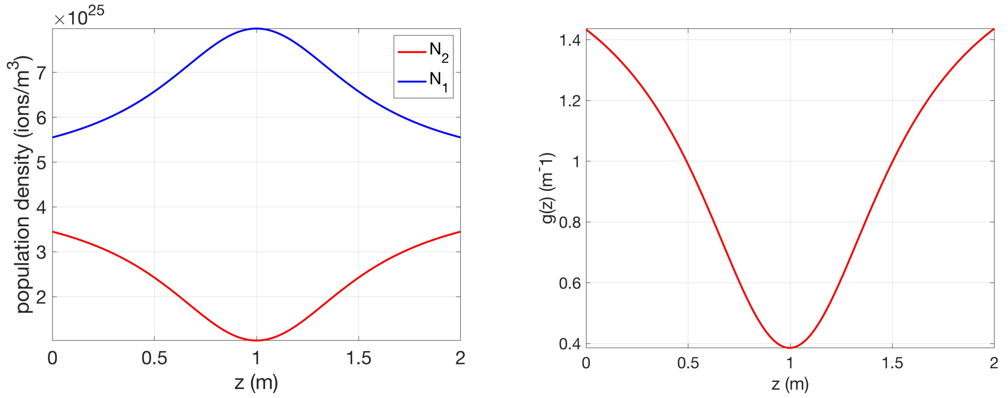

(b) Populations in forward-backward pumping scheme **(c)** Gain coefficient in forward, backward pump

Figure 4.5: Signals, population and gain coefficient in forward and back pumping.

Figure 4.5 shows plots of signal and pump power propagation, populations of Yb^+ ion at higher and lower energy levels. In figure 4.5a the pump power propagation in forward P_p^+(W) and backward P_p^-(W) evolution along 2m fiber length is considered. From the same figure we can also see the power evolution of signal P_s^+(W) in forward propagation directions. In figure 4.5b it is plotted the population fraction at higher excited energy level N_2 and at lower lower N_1 for both forward as well as backward pumping scheme simultaneously. Similarly position or z dependent gain coefficient in forward and backward pumping scheme is shown in figure 4.5c. The position dependent gain coefficient g(z) which varies along z direction is given by equation (4.15) as follows:

$$g(z) = \Gamma_s \left[(\sigma_{as} + \sigma_{es})N_2(z) - \sigma_{as}N_T\right] - \alpha_s \tag{4.15}$$

4.3 Saturation Intensity and Fluence

Before diving into the discussion of saturation power and energy of continuous wave and pulsed input laser signals, let's see some basic characteristics of pulsed lasers first. Pulsed lasers emit discrete pulses at a given repetition rate or frequency as shown in figure 4.6. Regularly repeating train of optical pulses have a period (T) related to repetition rate (f_{rep}) reciprocally, i.e, $T = 1/f_{rep}$. Assume the energy (E) contained in every pulse constant, power is just the time rate of change of the energy flow (energy per unit time). So this leads us to define two different types of power, peak power and average power. Pulse peak power is estimated from pulse energy and pulse width also called pulse duration ($\tau_{pulse} = \Delta t$). Similarly, pulse average power is determined from pulse energy (E) and pulse period (T). Assuming uniform power distribution, the peak (P_{peak}) and average (P_{avg}) powers of pulsed laser are given by:

$$P_{peak} = \frac{E}{\tau_{pulse}} \tag{4.16}$$

$$P_{avg} = \frac{E}{T} = Ef_{rep} \tag{4.17}$$

Rearranging variables allows us to define a new quantity called duty cycle, which indicates the fractional amount of time the laser is ON during any given period. The duty cycle is thus given by the ratio of pulse duration to pulse period, or by the ratio of average power to peak power, as provided by equation (4.18) below.

$$\text{Duty cycle} = \frac{\tau_{pulse}}{T} = \frac{P_{avg}}{P_{peak}} \tag{4.18}$$

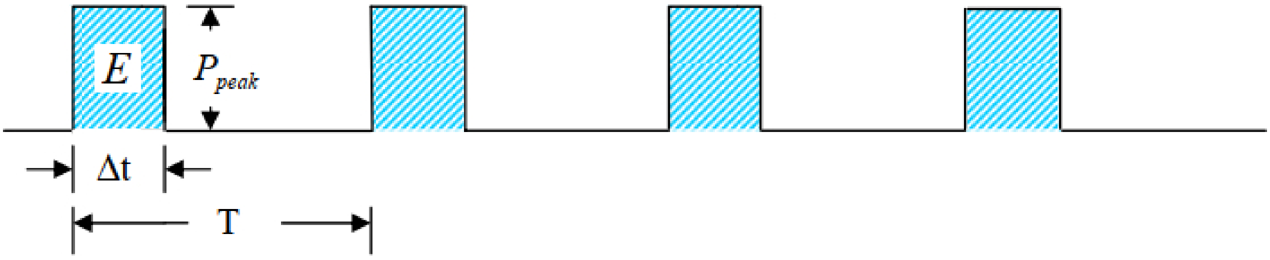

Figure 4.6: Temporally separated pulses of a pulsed laser

Continuous wave and pulsed lasers both can be described by the same intensity saturation parameter if pulse duration is longer than fluorescence lifetime (upper-state lifetime). On the contrary, we must apply energy density saturation parameter instead of intensity saturation when pulse time duration is lower than fluorescence lifetime. Saturation energy is a measure of the incident optical pulse energy required for achieving significant saturation of an absorber or a gain medium. Other parameter is saturation fluence which is the saturation energy per unit area [12]. Saturation power (P_{sat-CW}) for continuous wave lasers and saturation fluence F_{sat} (energy of pulsed laser per unit area) for pulsed lasers are given as follows:

$$P_{sat-CW} = \frac{h\ A\ \nu_s}{\tau(\sigma_{as} + \sigma_{es})} \tag{4.19}$$

$$\begin{aligned} I_{sat-CW} &= \frac{P_{sat-CW}}{A} \\ &= \frac{h\ \nu_s}{\tau(\sigma_{as} + \sigma_{es})} \end{aligned} \tag{4.20}$$

$$\begin{aligned} I_{sat-pulse} &= \frac{\tau}{2\tau_{pulse}}\ I_{sat-CW} \\ &= \frac{h\ \nu_s}{2\tau_{pulse}\ (\sigma_{as} + \sigma_{es})} \end{aligned} \tag{4.21}$$

$$E_{sat-pulse} = \frac{h\ \nu_s\ A}{2\ (\sigma_{as} + \sigma_{es})} \tag{4.22}$$

$$E_{pulse} = P_{peak}\tau_{pulse} \tag{4.23}$$

$$F_{sat} = \frac{E_{pulse}}{A} \tag{4.24}$$

where τ upper state lifetime, τ_{pulse} pulse duration, A is mode area, ν_s signal frequency, σ_{as} and σ_{es} are absorption and emission cross sections of the laser signal, I_{sat-CW} is saturation intensity of continuous wave, $I_{sat-pulse}$ is saturation intensity of pulsed laser, $E_{sat-pulse}$ is saturation energy for pulsed lasers, and E_{pulse} is energy of pulsed laser.

Let us use ytterbium doped multimode fiber parameters implemented in experiment [46], to determine the saturation power and saturation intensity. In fiber amplifiers and fiber lasers, saturation power and saturation energies are parameters that affects and determines their performance. In unsaturated regimes, fiber amplifiers and fiber lasers are characterised normally, that is, input conditions have direct effect on the output. For instance, increasing the input power have direct consequence on the output power, the output power is also increased. However, in the saturated region this kind of relation is no more valid. Hence it is essential to know the saturation powers in continuous wave signal or saturation energy as well as in pulsed type of input seeds. To calculate these saturations we use saturation equations given by (4.19) through (4.24). The main parameters used in experiment by Niang and et al. [46] are: core and cladding diameters of 47/114μm input average power 22.5mW, 1.1dB/m linear attenuation, 5m Yb-doped graded-index multimode fiber length, 10W continuous wave pump power, 500ps pulse duration, input pulse laser with 500Hz repetition rate at 1064nm signal and 940nm pump wavelengths. We found out that the saturation power of continuous wave signal, $P_{sat-CW} = 1.1015W$, continuous saturation intensity, $I_{sat-CW} = 6.3488 \times 10^8\ W/m^2$, saturation intensity of pulsed laser, $I_{sat-pulse} = 6.3488 \times 10^{14}\ W/m^2$, and saturation energy of pulsed laser, $E_{sat-pulse} = 5.5074 \times 10^{-4}\ J$. Determining these saturation intensities and power is essential in fiber amplifiers and laser, to know weather they are operating in maximum achievable power level or normal operation region (below the saturation point). To investigate this point further, let's see scenarios under which there could be local pulse energy saturation in self replicating beam propagation in graded-index multimode fiber. With 10W peak signal power and pump power of 20W, the pulse energy is determined to be, $E_{pulse} = 5nJ$. If the saturated energy is less than, this pulse energy ($E_{pulse} = 5nJ$), then it is said to be the pulse energy is saturated, this could be achieved when the signal (beam) diameter is 0.1μm, and the saturated pulse energy at this signal diameter is, $E_{sat-pulse} = 2.493nJ$. To sum up, the pulse is saturated, when the saturation energy of the pulse is lower than the pulse energy ($E_{sat-pulse} < E_{pulse}$). Saturation energy of the pulsed fiber laser or amplifier is the maximum achievable energy, and once the pulse is saturated increasing the input laser signal or other input conditions could not increase the output fiber amplifier and fiber laser signal.

As we can see from figure 4.7 the mode diameter when there is high intensity is 7.4μm, and at the position where there is low intensity is 55μm. This shows energy of the pulse is not saturated locally along the propagation direction, as the beam diameter is larger than 0.1μm at high intensity point. In other words, for this situation, the pulse energy is, $E_{pulse} = 5nJ$, and saturated pulse energy at larger beam diameter (55μm) is, $E_{sat-pulse} = 754.18\mu J$, and at lower beam diameter (7.4μm), $E_{sat-pulse} = 13.653\mu J$. Under both these situations the saturation pulse energy is higher than, the pulse energy which confirms there is no local saturation along the pulse propagation direction.

Generally, we have shown that the pulse saturation properties are strongly dependent on mode area, peak power, repetition rate and pulse duration. From the energy conservation point of view as well, the gain of the amplifier have to saturate, because we cannot extract more output power from the amplifier than it was [12]. Operating fiber amplifiers in saturation region could have also advantages [12], some of which are: small fluctuations in the seed signal do not reflect to the same extent in the output amplified signal, fiber amplifier which has multiple spectrally close input signals with variable intensity, may work as a gain equalizer because smaller input signal powers have higher gain (through less saturation), and higher input powers have lower gain (due to a higher degree of saturation), and saturated optical amplifier presents a high energy extraction efficiency.

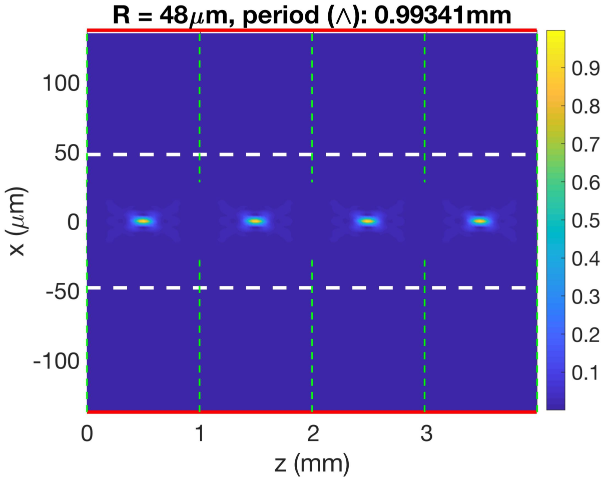

(a) Self-imaging in GRIN MMF

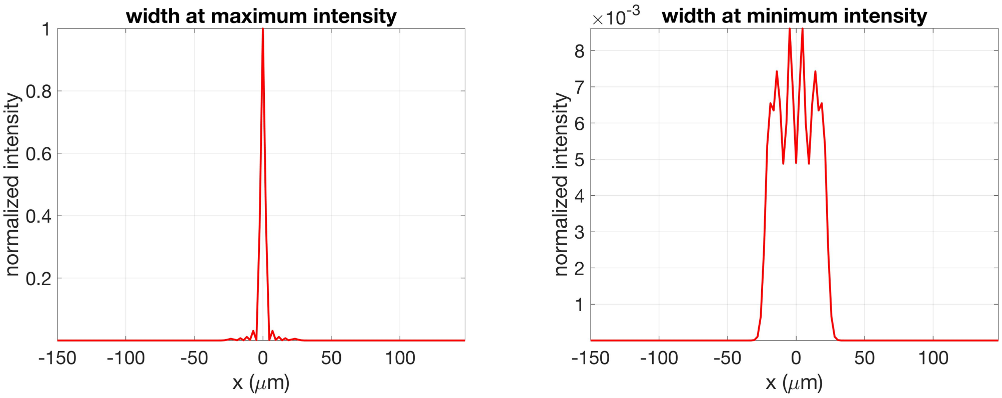

(b) Beam width under maximum intensity **(c)** Beam width under minimum intensity

Figure 4.7: Local intensity saturation phenomenon in GRIN MMF

4.4 Optimization of Parameters and Maximizing Gain

Now let's explore how to optimize parameters to investigate maximum gain in Yb^{3+} doped multimode fiber amplifiers, from bulk medium rate and propagation equations. In other words, here we will see how we can maximize the gain of pulsed signal power and control the output power by optimizing pulsed laser parameters given in table 4.2. These parameters in active multimode fibers include, input power of signal, input pump power, dopant concentration, fiber length, beam width, fiber core radius and filling factor ratios. In addition to input parameters pumping schemes, i.e, cladding or core, backward or forward pumping could also affects the amplification phenomenon.

Parameters	Value	Parameters	Value
$D_{core}(\mu m)$	96	$\lambda_s(nm)$	1064
$D_{clad}(\mu m)$	275	$\lambda_p(nm)$	940
FWHM(μm)	75	P_{pump} (W)	20
L (m)	1	$\tau(ms)$	1
n_{core}	1.47	n_{clad}	1.457
$\sigma_{as}(m^2)$	5.0×10^{-27}	$N_0(ions/m^3)$	9.0×10^{25}
$\sigma_{es}(m^2)$	2.89855×10^{-25}	P_{peak}(W)	10
$\sigma_{ep}(m^2)$	2.358×10^{-24}	Δt(ps)	500
$\sigma_{ap}(m^2)$	2.358×10^{-24}	f_{rep}(Hz)	500

Table 4.2: Pulsed laser parameters used in [19] numerical simulations.

Rather than increasing the pump power, and dopant concentration to have gain maximization or signal power amplification we have increased the signal beam diameter and achieved higher seed gain in backward pumping scheme. Using parameters listed in table 4.6 with pump power of 20W in backward pumping, and peak signal power of 10W, we can observe pump power, signal power and gain coefficient propagation. In figure 4.8, 40μm signal diameter is considered all other parameters kept constant with respect to the plot in figure 4.9 where 75μm signal width diameter is examined.

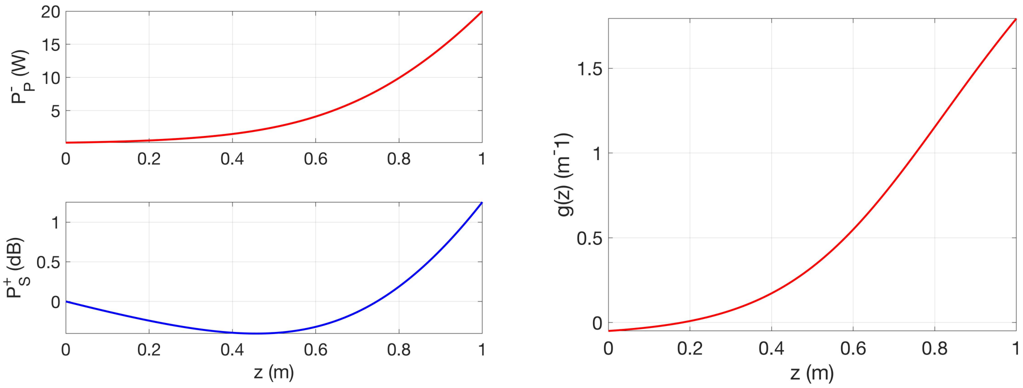

(a) Pump and signal power **(b)** Gain coefficient per meter

Figure 4.8: Signal and backward pump power propagation with 40μm signal diameter.

A gain more than 6dB is obtained as it could be observed from figure 4.9, using 10W peak input power at 1m fiber length. The same input conditions are used as when the input beam width is 20μm, but here it is incremented to 75μm, and we obtained higher gain six times larger.

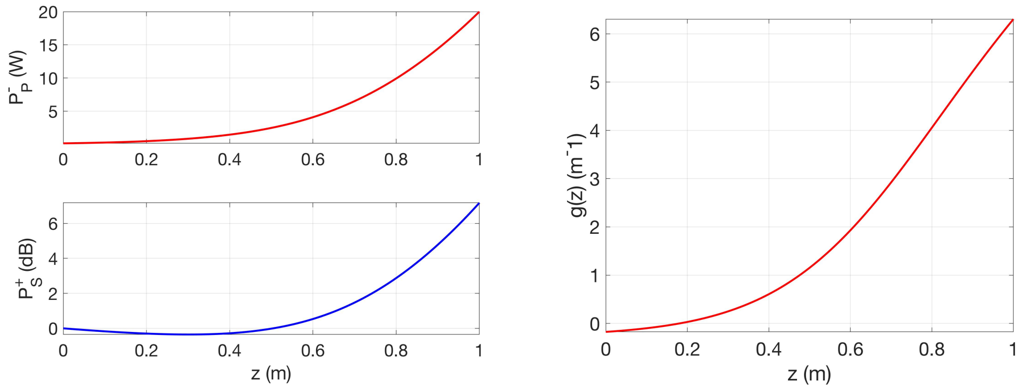

(a) Pump and signal power **(b)** Gain coefficient per meter

Figure 4.9: Backward pump and signal power propagation with $75\mu m$ signal diameter.

Figure 4.10 shows propagation of pump and signal powers both in forward direction. Except the pumping scheme (forward in this case), other parameters remains the same as the previous two figures, where the pump was propagating backward, with signal having a diameter of $75\mu m$ full width at half maximum, and 20W pump power. In the first half meter of the fiber the signal propagates linearly, from its minimum to 8.5dB maximum signal power gain. After the first half of the fiber the pump power is totally absorbed, and the signal power gain remains constant, where there is no more increment.

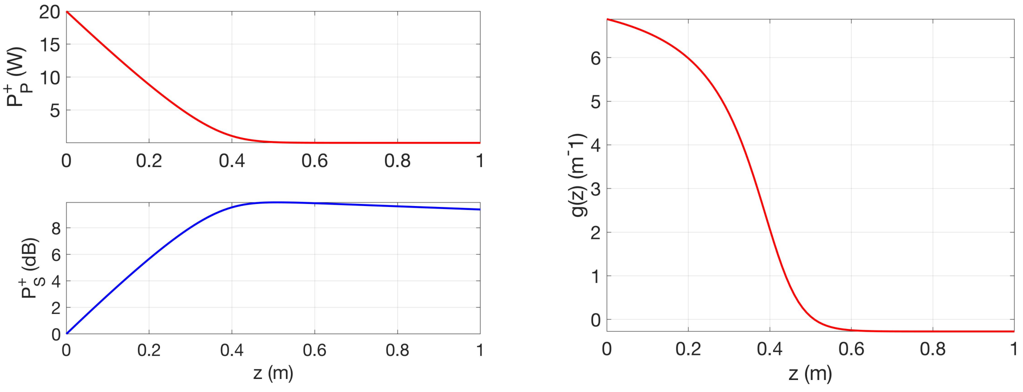

(a) Pump and signal power **(b)** Gain coefficient per meter

Figure 4.10: Forward pump and signal power propagation with $75\mu m$ signal diameter.

4.5 Chapter Summary

In this chapter, rate and propagation equations for highly multimode fiber amplifiers by considering core and cladding pumping schemes are formulated and studied. The evolution of pump power, signal and populations are plotted under different circumstances of pumping: forward, backward, and both forward and backward. Saturation intensity for continuous wave signals, and saturation fluence for pulsed laser inputs are also formulated and investigated.

Local intensity saturation for self-imaging input signal in graded index multimode fiber is analysed, and discussed. After making numerical investigations and analysis, we realized that local saturation could happen inside fiber amplifiers, at high intensity (pinch) point. Conditions that maximize the signal gain by optimizing the given fiber amplifier parameters are also thoroughly studied in this chapter

Chapter 5

Nonlinear and Gain Coupling in Unperturbed Multimode Fibers

In a perfect multimode optical fiber, mode coupling would not occur because each mode is orthogonal to the others. However, because of imperfections in fibers, such as bends, local gain and temperature modes can couple [38]. Mode coupling could also occurs in a tapered multimode fiber, where the core radius varies along the fiber length [59]. Each time when the core radius varies, power is exchanged among the modes, and mode coupling happens. In [27][68] it is defined that there is weak mode coupling, when the coupling is between modes having similar propagation constants, and strong mode coupling is a coupling between modes having unequal propagation constants.

In our research activity, we have investigated mode coupling in ytterbium doped multimode fibers due to active medium (gain), Kerr nonlinearity and random disorder. In this chapter we will investigate coupling in unperturbed active multimode fiber, that is, excluding disorder which will be discussed in the next chapter. Uniform gain distribution is considered first and position dependent gain across the fiber propagation distance is contemplated. In addition, we probed mode selection techniques to achieve single mode regime beam quality of the laser output in large mode area fiber. This could be realized by suppressing the excitation or propagation of high order transverse modes in active GRIN multimode fibers, by carefully adjusting the launch conditions of the signal beam and modifying the dopant profiles. Input seed beam with inclined angle, parabolic and ring dopant profiles are examined in our numerical simulations for mode selection and beam cleaning activity.

Let us start by examining the sole effect of non-homogeneous gain distribution, in which the evolution equation is provided by:

$$\frac{\partial E_g(x,y,z)}{\partial z} = \frac{1}{2} g(x,y,z) E_g(x,y,z) \tag{5.1}$$

where $g(x,y,z)$ is intensity gain and obtained from equation (4.9) in chapter 4. This gain term is related to the rare-earth dopant populations at lower and higher energy level after excitation by pump power, and determined from the rate equations. Expanding equation 5.1 with the modal basis or by substituting guided electric field given in chapter 1 into equation 5.1 we can obtain:

$$\frac{\partial}{\partial z}\left(\sum_n a_n(z)\psi_n(x,y)e^{i\beta_n z}\right) = \frac{1}{2} g(x,y,z)\left(\sum_n a_n(z)\psi_n(x,y)e^{i\beta_n z}\right) \tag{5.2}$$

All elements of the base are here identified by a single index, namely n. Now exploiting the orthogonality among the modes and projecting over another mode, say ψ_k one obtains the following coupled mode system

$$\frac{da_k}{dz} = \frac{1}{2}\sum_n a_n(z) \int\int g(x,y,z)\psi_n(x,y)\psi_k(x,y)^* e^{i(\beta_n-\beta_k)z} dxdy \tag{5.3}$$

where,

$$\int\int \psi_n(x,y)\psi_k(x,y)^* e^{i(\beta_n-\beta_k)z} dxdy = 1 \text{ , when n = k}$$

From equation (5.3) we can make the following general main points:

1. In case when the gain $g(x,y,z)$ is homogeneous in x,y as it happens for uniform dopants and uniform pump distribution the equation reduces to:

   $$\frac{da_k}{dz} = \frac{1}{2}\sum_k g(z)a_k(z) \tag{5.4}$$

   This fact implies that each mode sees exactly the same gain and modes are not coupled by gain. In other words, there is no selection of modes by gain. Coupling can still be possible due to other factors like, linear mode coupling (fiber bending) or nonlinear mode coupling, but these terms are not present here.

2. In case the gain $g(x,y,z)$ is not homogeneous in x,y dopants or pump beam should feature non homogeneity at the scale of the mode sizes, then equation (5.3) shows that a non uniform gain brings mode coupling. Some coupling terms are fast oscillating due to the beating terms among the modes. In GRIN multimode fibers some of these terms are not fast oscillating due to the degeneracy of modes (resonant coupling), mode coupling induced by gain is discussed for instance in [43]. In this case when the gain is not uniform, one can rewrite equation (5.3) in the following way:

   $$\frac{da_k}{dz} = \sum_{n,k} G_{n,k}(z)a_n(z)e^{i(\beta_n-\beta_k)z} \tag{5.5}$$

   where,

   $$G_{n,k}(z) = \frac{1}{2}\int\int g(x,y,z)\psi_n(x,y)\psi_k(x,y)^* dxdy \tag{5.6}$$

   It is evident that to have a modal selection by gain the gain non uniformity should be at the scale of the modal distribution. The gain per mode, $G_{n,k}(z)$, provided by equation (5.6) depends on the transverse dopant distribution and pump modal profile.

3. Note that this model consider only the possible coupling induced by non uniform gain. The presence of gain implies also other mechanisms of mode coupling here not considered: Thermal variation of the refractive index, gain saturation (non uniform in x,y), variation of the refractive index close to resonance.

Another important feature is when modal dependent gain (as the one arising from non uniformity of dopants) meets a coupling mechanism, especially when the two scales (differential gain and coupling length) have similar size. For the case of mode dependent gain and linear mode coupling (especially for two modes) this point has been investigated in several papers [20] [66]. A much less explored case is a multimodal system where the coupling mechanism is both linear and nonlinear. Limiting first our analysis to the nonlinear coupling only in presence of gain, our modelling equation to solve numerically is derived in chapter 2 from evolution of optical beam governed by multi-dimensional nonlinear equation, and here we will add the effect of gain on nonlinearity [5]. The general coupled mode equation due to non-uniform distribution of gain and nonlinearity we implemented to study the evolution of modal power along the fiber length is given by equation (5.7). In other words, we need to add the gain term for active multimode fiber, formulated by equation 5.5 into coupled mode equation only due to nonlinearity, and the coupled mode equation given by (5.7):

$$\frac{da_n}{dz} = \sum_k G_{k,n}(z) a_k(z) e^{i(\beta_k - \beta_n)z} + i\gamma \sum_{m,p,q} Q_{m,p,q,n} a_m a_p^* a_q e^{i\Delta\beta_{m,p,q,n} z} \tag{5.7}$$

where the function a_n represents the slowly varying complex amplitude of mode n, with corresponding linear propagation constant β_n. $\Delta\beta_{m,p,q,n} = \beta_m - \beta_p + \beta_q - \beta_n$ is the phase mismatch for the mode group with indices m,n,p,q and overlap coefficients $Q_{m,p,q,n} = \int\int \psi_m \psi_p^* \psi_q \psi_n^*$ where $\psi_n(x, y)$ is the n-th element of the orthonormal basis of guided modes. $\gamma = \frac{n_{2kerr}\omega}{c}$ is the nonlinear coefficient (m/W) of the fiber at the angular frequency ω (rad/sec), with n_{2kerr} being nonlinear index having a value of $3.2x10^{-20}(m^2/W)$ for silica fibers.

The total input power P_{in} in our numerical model is determined by integrating intensity across the fiber area using equation (5.8) at $z = 0$. The power evolution of each mode $P_n(z)$ is plotted both in linear and the dBW (decibel watts) scale, where the dBW scale is given by equation (5.9).

$$P_{in}(z = 0) = \sum_n |a_n(z = 0)|^2 \tag{5.8}$$

$$P_n(dBW) = 10\, log_{10} \left(\frac{P_n(W)}{1W} \right) \tag{5.9}$$

5.1 Coupling with Uniform Gain Profile

Here we will illustrate the case of flat gain and an input Gaussian beam of diameter 10μm at FWHM (full width at half maximum) an input tilt angle so not to excite preferentially the fundamental mode. The small input tilt angle is also considered to compensate the disturbance that occurs in experiment or practically. The refractive index and gain profile for uniform dopant distribution are illustrated in Figure 5.1a (top left panel). In the figure 5.1 it is also plotted the propagation of modal power for 2m long GRIN multimode fiber length. The blue curve shown in the figure is the fundamental mode, labelled HG_{00}, where HG stands for Hermite-Gaussian mode. For the first meter of propagation the evolution in logarithmic scale is linear, all modes grow with the same gain as expected and the fundamental mode has not the largest component due to the initial tilt ($2.5°$). In the second meter the propagation starts to exhibits a nonlinear evolution, and modes exchange energy. Modes are more and more coupled by the nonlinear terms as soon as the beam is amplified. The fractional contents depends (for a fixed input condition) on the input power. To solve equation 5.7 numerically we limited the sum only to those terms having a low (< 50 rad/m) phase mismatch (both for gain and FWM). However it is known that rapidly varying coupling terms are responsible for an effect of gain equalization (gain non uniformity can be equalized by rapidly varying terms) and new simulations should consider also these rapidly varying terms [64]. In this first study the fast oscillating terms are removed to increase the computational efficiency. Evolution of modal powers and gain per mode for a total of 25 simulated Hermite-Gaussian modes for uniform dopant profile is illustrated in Figure 5.1.

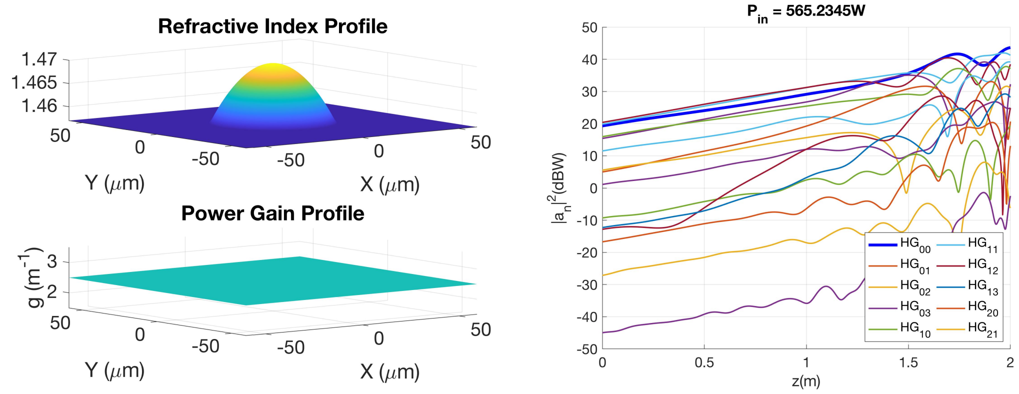

(a) Refractive index and gain profile

(b) Evolution of modal powers

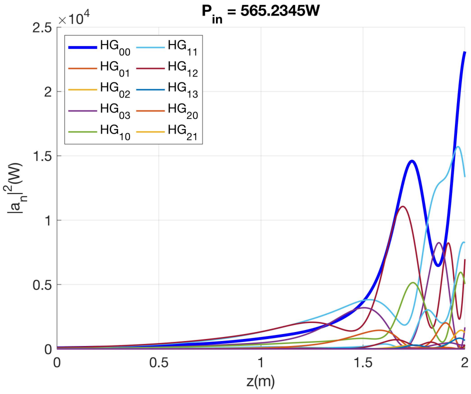

(c) Modal power evolution

Figure 5.1: Evolution of modal power upon amplification with flat gain profile.

In figure 5.2 the input power is increased from 565.234W to 1017.422W with respect to figure 5.1, but other parameters are kept the same. Here we can observe that increasing power has significant effect in modal power coupling, as the effect of Kerr nonlinearity is higher. For uniform gain profile, all the guided modes (25 Hermite-Gauss modes) have equal gain per mode (G(n,k)) in units of per meter. Table 5.1 indicates some of the guided Hermite-Gauss modes used in our numerical simulations as indicated also in the legend of the figures. The tables shows the number of modes that corresponds to the Hermite-Gaussian (HG_{mn}).

Hermite-Gauss Modes	**Mode Number**	**Hermite-Gauss Modes**	**Mode Number**
HG_{00}	1	HG_{10}	6
HG_{01}	2	HG_{11}	7
HG_{02}	3	HG_{12}	8
HG_{03}	4	HG_{13}	9
HG_{04}	5	HG_{14}	10

Table 5.1: Fundamental and high order modes (not the whole guided modes) used in our numerical simulations.

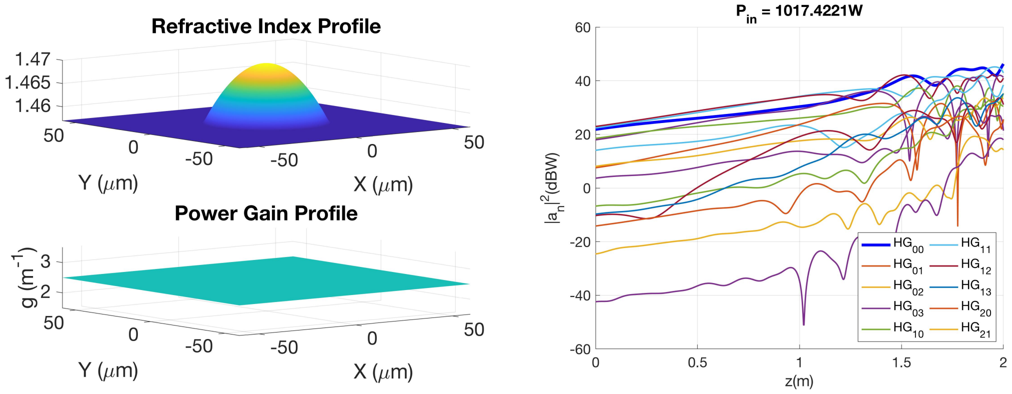

(a) Refractive index and gain profile **(b)** Evolution of modal powers

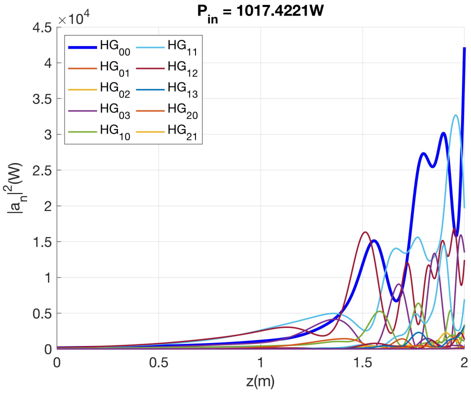

(c) Modal power evolution

Figure 5.2: Propagation of modal power upon amplification with uniform gain profile.

5.1.1 Position Dependent Gain Coefficient

Here we will see numerical simulations when the gain coefficient in equation 5.5 varies across fiber length or simply position dependent. The gain for each eigenmode $G_{n,k}(z)$ can then be calculated as follows:

$$G_{n,k}(z) = \frac{1}{2}\int_{-\infty}^{+\infty}\int_{-\infty}^{+\infty} g(z)\psi_n(x,y)\psi_k^*(x,y)\mathrm{dxdy}, \qquad \text{for } n = k \tag{5.10}$$

where $g(z)$ is position dependent gain or gain coefficient determined from pump power and dopant concentrations, using shooting and Runge-Kutta algorithms discussed in chapter 4.

Numerical simulations in figure 5.3 and 5.4 below shows the case in the presence of Kerr nonlinear effect, uniformly distributed dopant concentration with 10W pump power and back pumping scheme. The power evolution of modes in this case shows, there exist modal interaction along the fiber length irrespective of the magnitude of position dependent gain coefficient. The mode coupling is more complex after the first meter of fiber length which is due to higher amount of gain coefficient in that region. Furthermore, the interaction and modal power exchange is higher when the input power is increased from 565.23W to 5.652kW, as it could be seen in figure 5.4a and 5.4b.

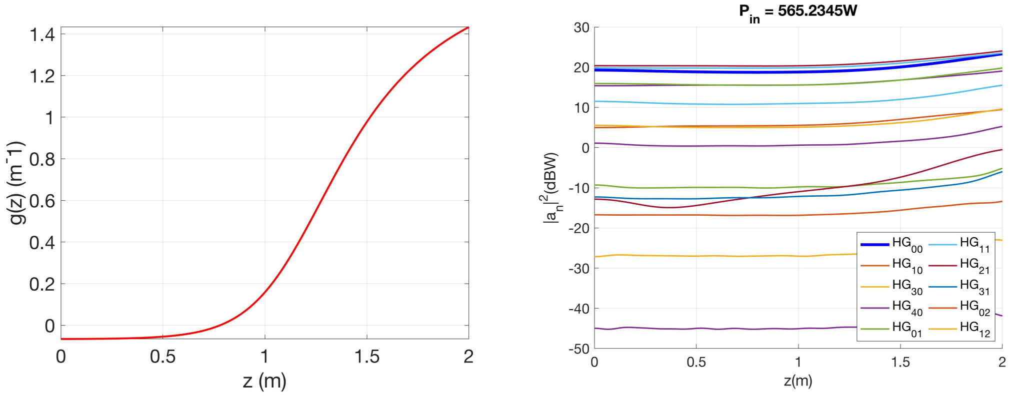

(a) Gain coefficient in backward pump

(b) Modal power evolution in dBW

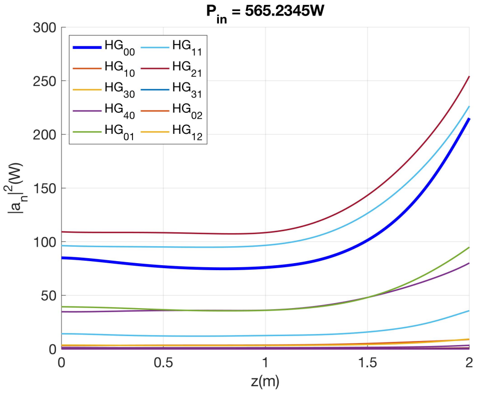

(c) Modal power evolution in linear scale

Figure 5.3: Modal power evolution for z dependent gain and with nonlinearity.

Figure 5.3 and 5.4 are numerical simulation results under the same input parameters, except the input power is increased in the later figure. Both gain and nonlinear effects are included, but the coupling is due to nonlinearity, because the gain distribution is uniform along the fiber length. As we can observe in figure 5.4 there is high modal coupling among the fundamental mode (blue plot) and other high order modes, and power is transferred from one mode to another.

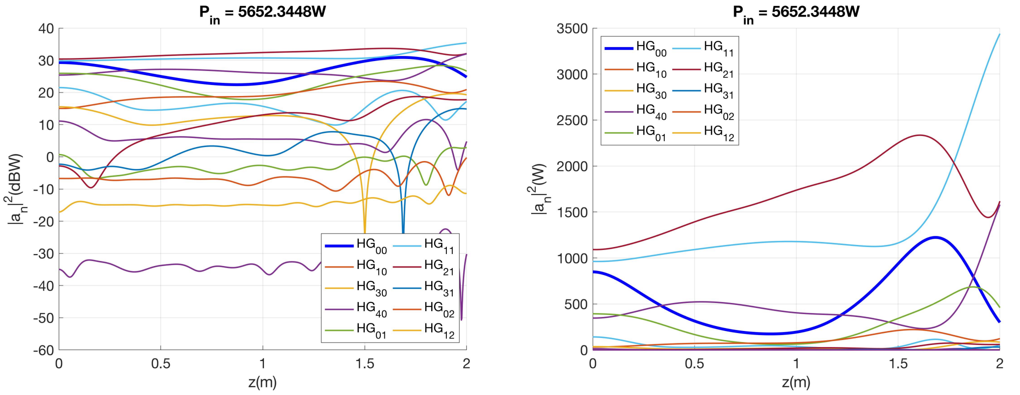

(a) Modal power evolution in dBW **(b)** Modal power evolution in linear scale

Figure 5.4: Modal power evolution for z dependent gain and with nonlinearity.

5.2 Non-uniform Gain Coupling

We now consider, with the same input condition as before, a fiber with a parabolic graded-index (GRIN), but with a non uniform doping concentration. Under non-uniform distribution of active medium, we will see parabolic and ring dopant profile. Ring is a dopant profile where we have nearly zero gain in the center, and large gain for low and high order modes. These situations are, of course, difficult to obtain because the doping concentration also modifies the refractive index which in turn can be hardly kept parabolic unless with the insertion of other types of dopants to compensate. The index and gain profiles for ring dopant distribution is illustrated in Figure 5.12 (top left panel). The right panel of the same figure shows the evolution of the fractional contribution of modes. Again the first meter of propagation is nearly linear and it is possible to see how the fundamental mode (blue curve) is amplified less than the other modes as a result of the non uniform gain. Surprisingly when the nonlinear coupling get stronger then fundamental mode also grows up. Note that the mode is not amplified directly but it is driven by the coupling of the other modes.

5.2.1 Parabolic dopant profile

Evolution of modal powers, gain per mode for a total of 25 simulated Hermit-Gaussian modes for parabolic dopant profile is illustrated in figure 5.5. From figure 5.5c we can see that the gain per mode for fundamental mode (HG_{00}) is higher than that of other high order modes, that is in fact due to pump distribution and the dopant concentration which is higher inside the core, and favours the fundamental mode which has the same profile. From the same figure (figure 5.5c) we can see that, differential modal gain (the gain difference between modes) is small. Further we will investigate numerical simulation results for parabolic doped profile by increasing the input power, the effects of input source inclination and normal input incidence, the effects of reducing and increasing the dopant radius with respect to the radius of refractive index profile with 25 Hermite-Gaussian modes. First let's consider under low and then high input power, inclined incident input beam, and with the same size of dopant radius as that of core refractive index size (it could be observed from figure 5.5a).

Figures 5.5 to 5.7 shows numerical simulations of parabolic dopant distribution under the same input conditions (25 guided modes, 10μm input beam width FWHM, inclined to 2.5°) but the input power is increased from 565.23W to 5.6523kW. The refractive index profile, power gain profile, modal power evolution in dBW scale, gain per mode for each guided modes, and modal power propagation in linear scale (W) is provided in each figure respectively from top left to bottom right. Increasing the input power has significant effect for mode coupling due Kerr nonlinearity as well as non-uniform gain distribution. In other words, the modes are coupled strongly (complex) throughout the fiber length when the input power is higher, than when the input power is lower as it could be seen from figure 5.5b. As a result, there is high power transfer from high order modes to fundamental mode and among high order modes as well.

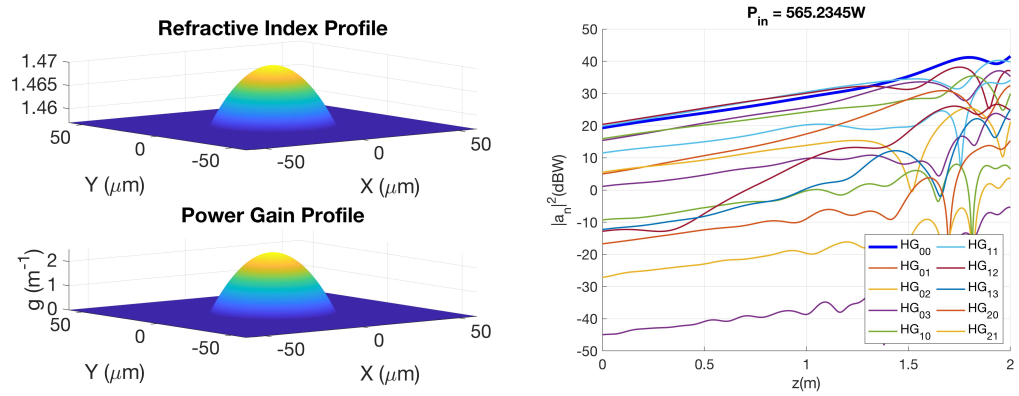

(a) Refractive index and gain profile **(b)** Evolution of modal powers

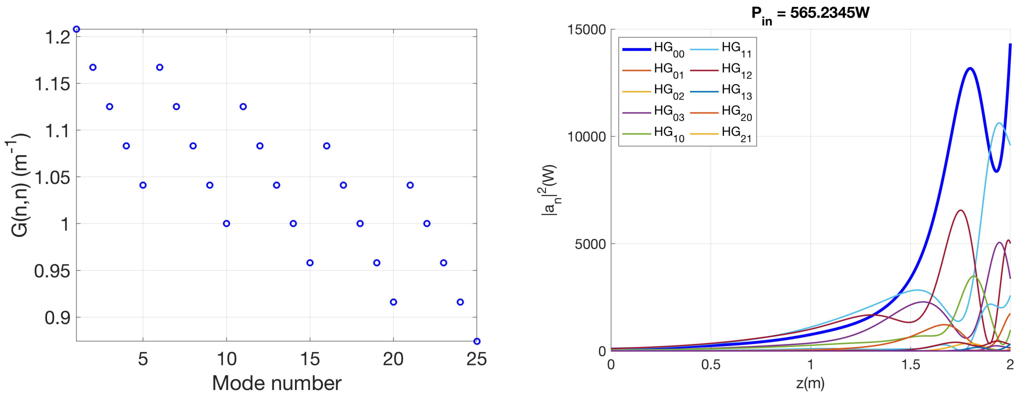

(c) Gain per mode **(d)** Modal power evolution

Figure 5.5: Propagation of modal power for parabolic gain profile.

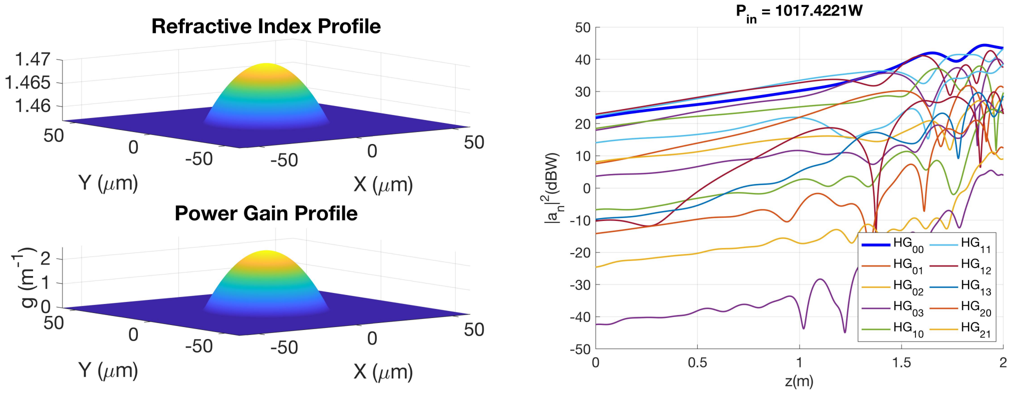

(a) Refractive index and gain profile **(b)** Evolution of modal powers

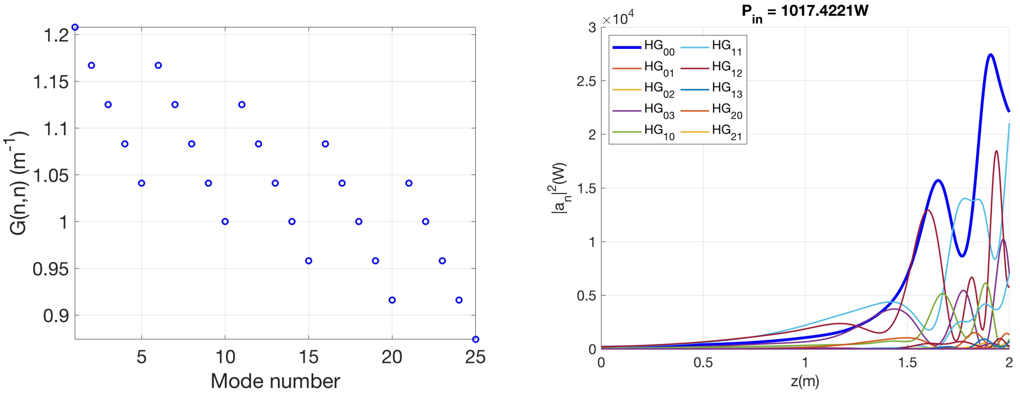

(c) Gain per mode **(d)** Modal power evolution

Figure 5.6: Evolution of modal power for parabolic gain profile.

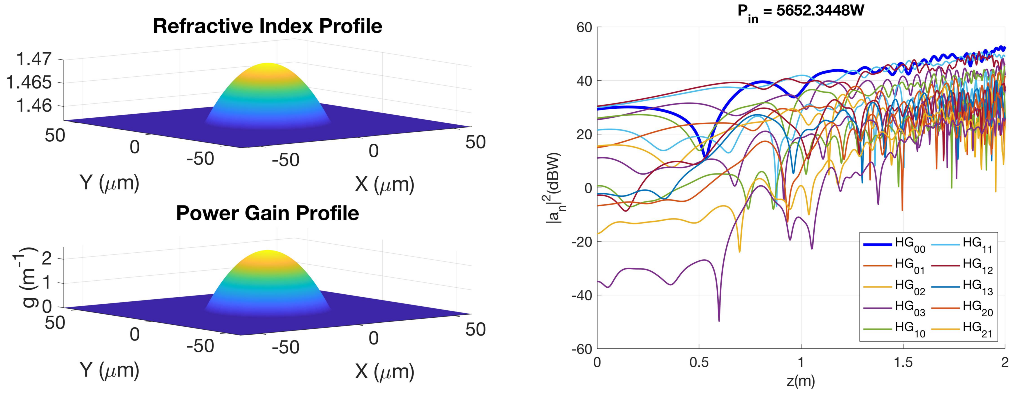

(a) Refractive index and gain profile

(b) Evolution of modal powers

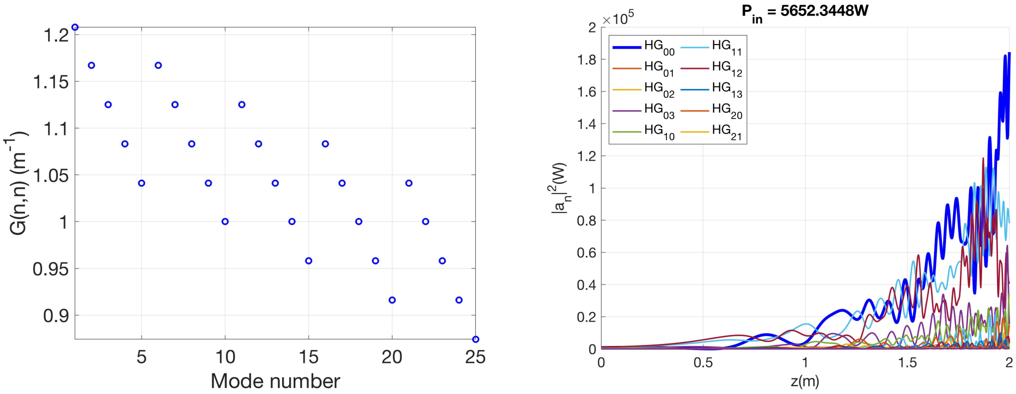

(c) Gain per mode

(d) Modal power evolution

Figure 5.7: Evolution of modal power for parabolic gain profile and higher input power.

Furthermore, under the same parabolic dopant profile, we will see the results when reducing the radius of dopant concentration, with respect to refractive index profile. I reduced the radius of the dopant concentration to half of the radius of the core that is 13μm, and the simulation result is shown for two values of input power. Likewise, the modal power propagation results with larger radius of dopant concentration ($40\mu m$), is also shown in figure (5.11). It is understood from numerical simulation results that, by increasing the radius of rare-earth dopant distribution with respect to parabolic index profile, large number of modes could be supported and the output power is higher. This effect is only visible if the number of modes are higher, and increasing the dopant distribution is able to accommodate. Otherwise for smaller number of modes increasing the dopant radius may not bring any differences. The plots shown in figures (5.10) and (5.11) indicate propagation of modes along a 2m fiber length under 565.23W and 1017.42W input power respectively, with distribution of dopants covering larger fiber cross section. From the same figure it could be seen how the power of each mode vary under each input power, both in logarithmic and linear scales.

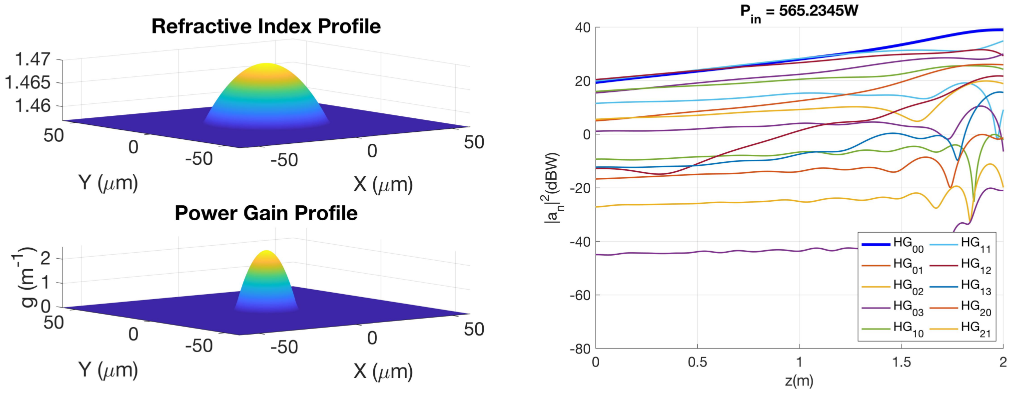

(a) Refractive index and gain profile **(b)** Evolution of modal powers

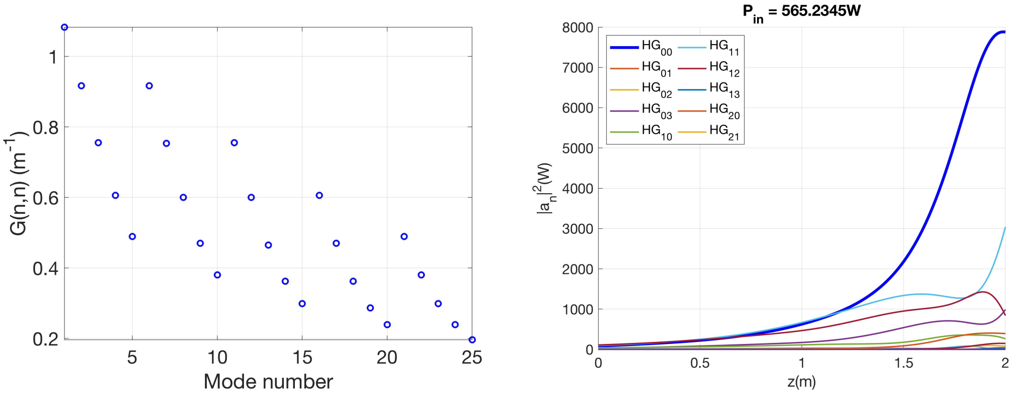

(c) Gain per mode **(d)** Modal power evolution

Figure 5.8: Evolution of modal powers with reduced radius of parabolic gain profile.

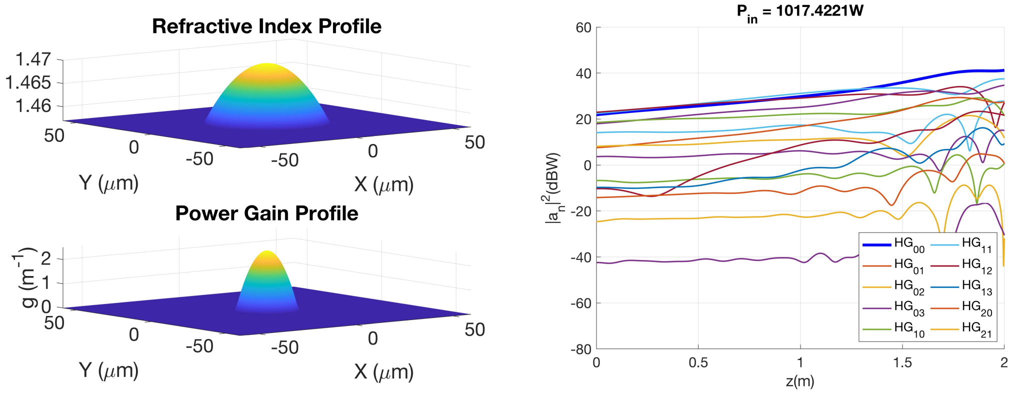

(a) Refractive index and gain profile

(b) Evolution of modal powers

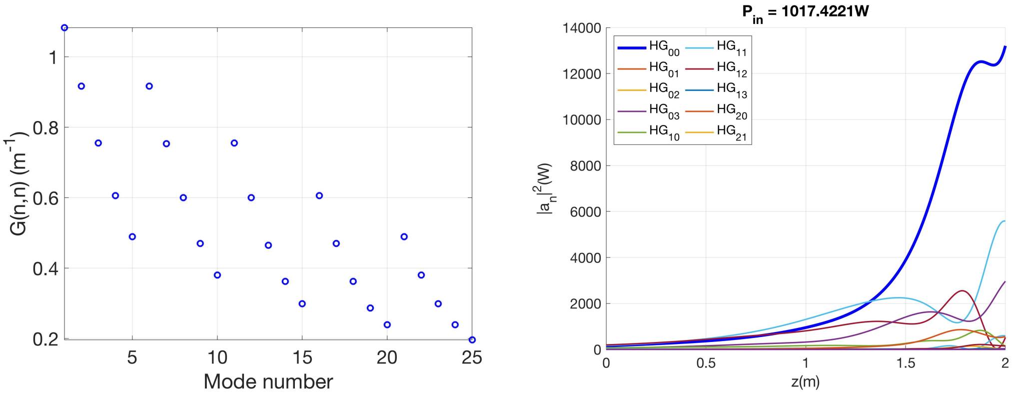

(c) Gain per mode

(d) Modal power evolution

Figure 5.9: Evolution of modal powers with reduced radius of parabolic gain profile.

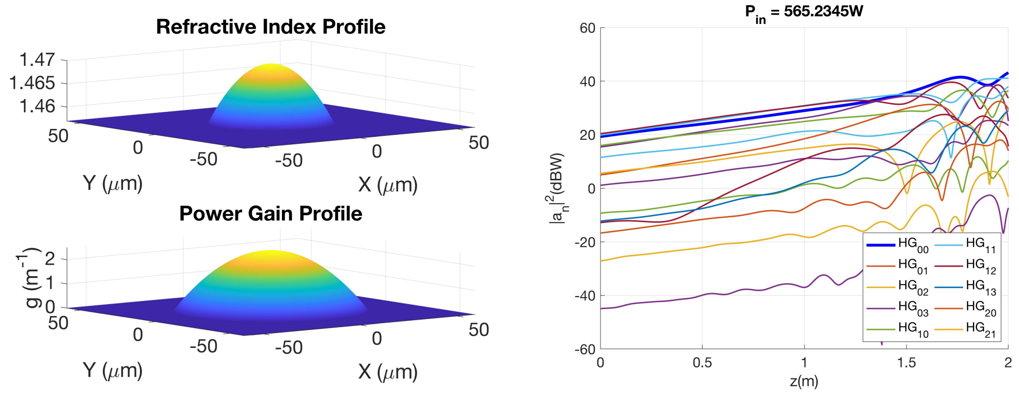

(a) Refractive index and gain profile

(b) Evolution of modal powers

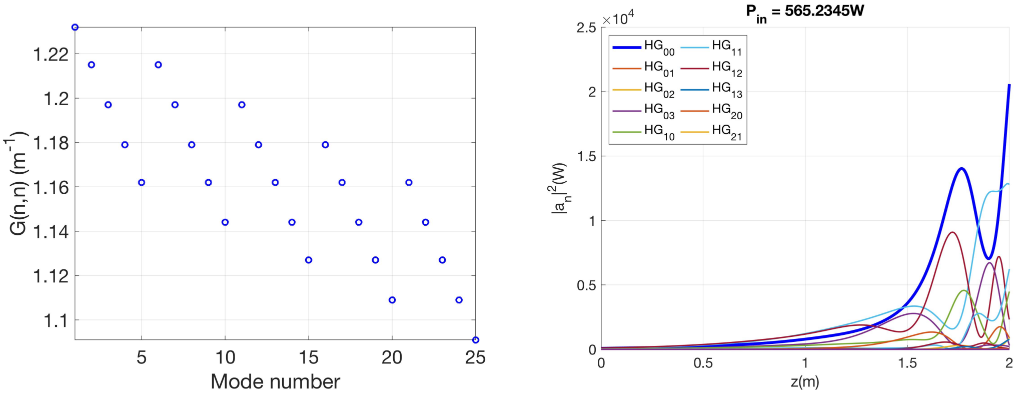

(c) Gain per mode

(d) Modal power evolution

Figure 5.10: Evolution of modal powers with larger radius of parabolic gain profile.

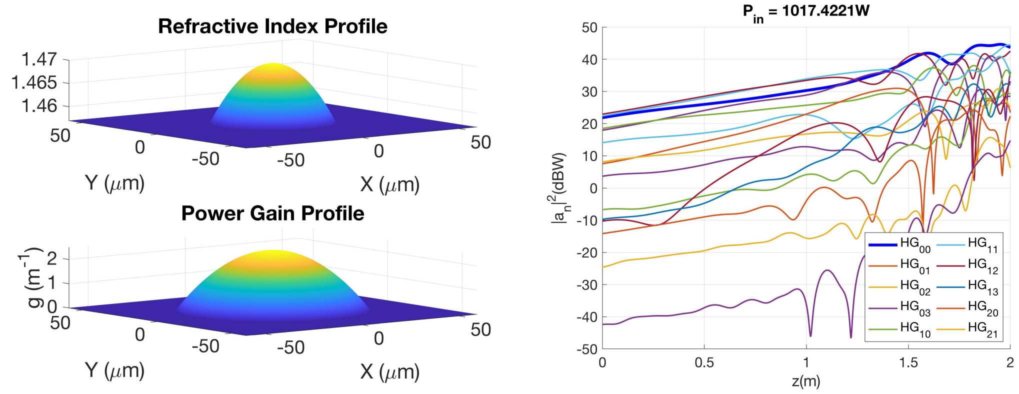

(a) Refractive index and gain profile

(b) Evolution of modal powers

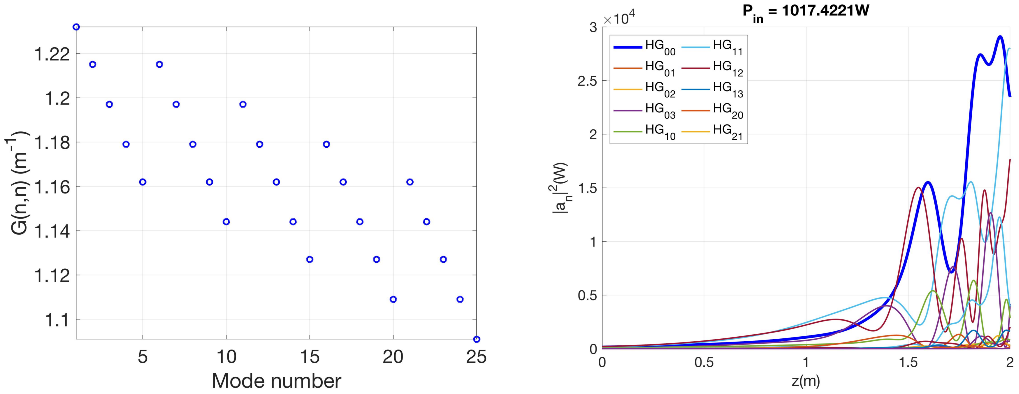

(c) Gain per mode

(d) Modal power evolution

Figure 5.11: Evolution of modal powers with larger radius of parabolic gain profile.

To summarize, what we have seen up to now are numerical simulation results for parabolic doped GRIN multimode fiber under different input power and dopant radius. It is clear that by increasing input power nonlinear length and modes nonlinear coupling distance is reduced. Decreasing the dopant radius towards the core, results in reduced output power. This is mainly due to the fact that, by reducing the dopant the input beam of light excites limited number of modes confined in that region of rare-earth elements and suppress the other high order modes outside the active region, which results in reduced output power amplification. In addition by reducing the dopant area, the differential modal gain as we can observe from the gain per mode plot (figures 5.8c and 5.9c) is higher as expected. Increasing the dopant concentration area however, have the opposite effect. Increasing the active medium region, will able to amplify all the high order modes supported by the GRIN multimode fiber. In the simulation, it is important to consider the number of modes used with respect to the dopant area. That means that if a few number of modes are considered in the simulation than the multimode fiber supports, increasing the dopant area might not have a significant difference or effect.

5.2.2 Ring dopant profile

The ring gain profile is shown in Figure 5.12a where the dopant is concentrated close to the cladding and sparse or null close to the core center. In ring dopant profile light in the spatially coherent high order mode is amplified and then coupled to the low (fundamental) mode [51]. This kind of dopant distribution has the advantage of increasing the efficiency of energy extraction in the amplifier, when the doped ring position coincides with a maximum in the high order mode intensity pattern. Here from the figure the radius at which we have a zero gain (no dopant concentration) is $10\mu m$. From the same figure we can see how the fundamental mode plotted with blue color is amplified less than the other high order modes due to the dopant distribution in addition to input tilt. This dopant profile in general favours amplification of higher order modes and transfers modal powers (due to exchange of energy) to the fundamental mode which is facilitated by nonlinear and non-uniform gain coupling. Furthermore, we will study the effects of increasing input power, and shrinking the dopant concentration towards the cladding, in other words increase the radius at which we have a zero gain around the center. It is expected that by shrinking the dopant concentration the output power amplification will decreases, due to the reduction of dopants. In other words this means, for lower dopant distribution, the output power is also reduced.

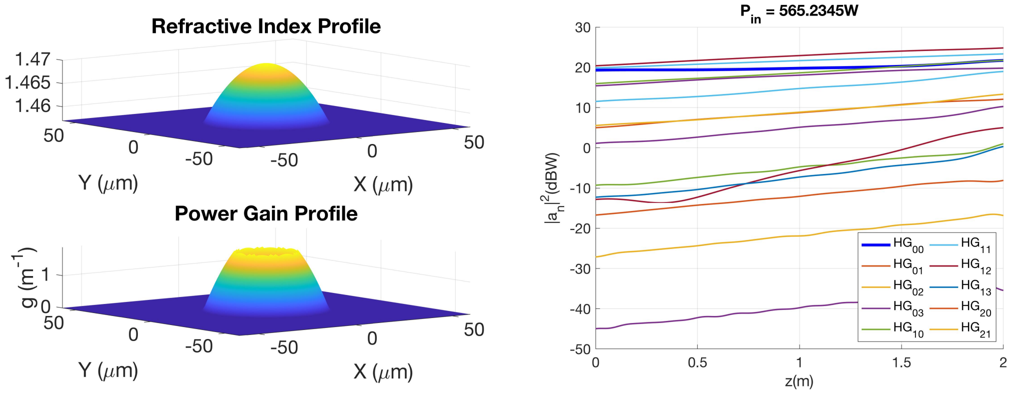

(a) Refractive index and gain profile

(b) Evolution of modal powers

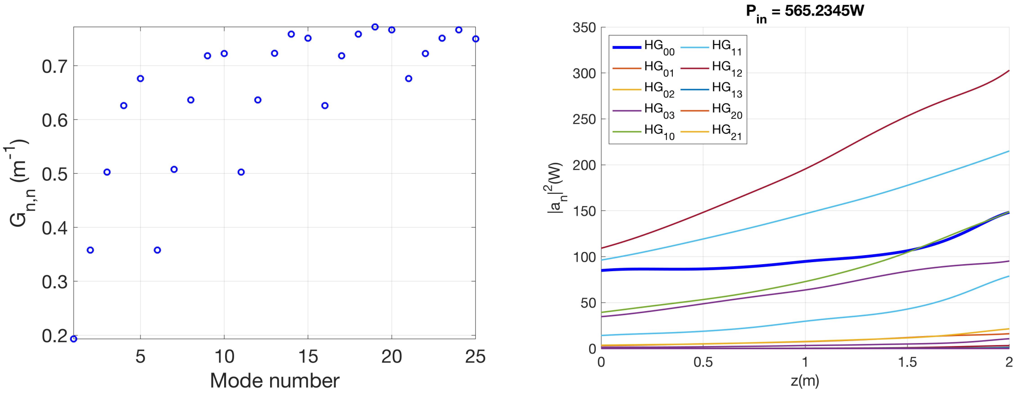

(c) Gain per mode

(d) Evolution of modal powers

Figure 5.12: Evolution of modal powers upon amplification with ring gain profile.

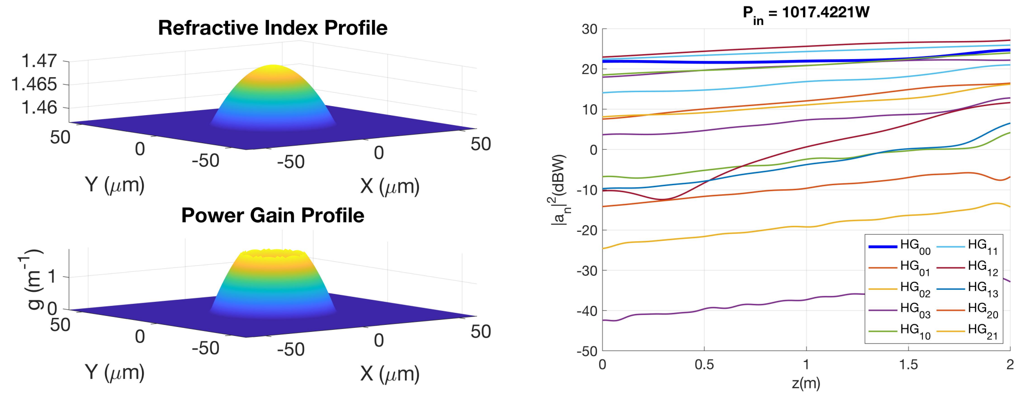

(a) Refractive index and gain profile **(b)** Evolution of modal powers

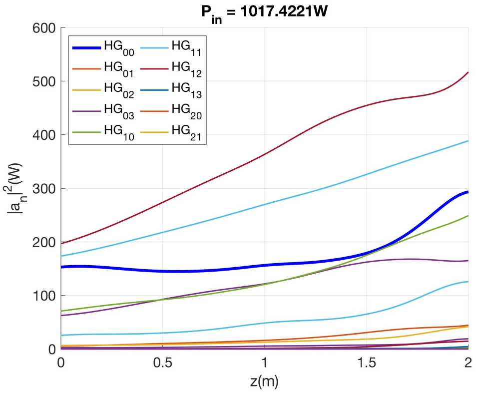

(c) Modal power evolution

Figure 5.13: Evolution of modal powers upon amplification with ring gain profile.

Finally from our numerical simulation results we presented until now under uniform and non-uniform dopant distributions, we can summarize main results as shown in table (5.2). From the table P$_{out}$(W) is the total output power at the end facet of fiber length obtained from the whole considered modes (guided modes). The power in decibel scale (dB) is given as the ration of output to input power in logarithmic scale. It is clear from the table that under the same input conditions, the total gain in dB scale is lower for ring dopant profile.

$$Gain(dB) = 10\ log_{10}\left(\frac{P_{out}(W)}{P_{in}(W)}\right) \tag{5.11}$$

	$P_{in}(W)$	$P_{out}(W)$	Gain (dB)
1. Flat dopant profile	565.24	8.389×10^4	21.71
	1017.42	1.5100×10^5	21.71
	5652.34	8.3888×10^5	21.71
2. Parabolic dopant profile	565.24	5.5142×10^4	19.8926
	1017.42	9.9179×10^4	19.8892
	5652.34	5.5129×10^5	19.8915
3. Ring dopant profile	565.24	1.5550×10^3	4.3950
	1017.42	2.7930×10^3	4.3857
	5652.34	1.5340×10^4	4.3359

Table 5.2: Total gain, input and output power at the end of fiber length

5.3 Random Phase Distribution and Beam Cleaning

Random phase distribution and input beam tilt angle have direct consequences on the propagation of fundamental and higher order modes in active GRIN multimode fibers. Under this section we will scrutinize effects of uniform random phase distribution on output guided field. Intensity profile of output guided field shows speckle, as the random phase distribution increases. The random phase distribution angle (θ_R) is controlled by multiplying the uniform random number by an angle in the range of $0 - 2\pi$. In addition, large number of modes and a wide transverse spacial window are required to visualize a speckled beams using coupled mode equation. The spatial field envelope A(x,y) of a Gaussian input beam for initial condition are related to tilt angle (θ) and random phase distribution (θ_R) by equation (5.12).

$$A(x,y) = \int_{-\infty}^{+\infty}\int_{-\infty}^{+\infty} A_0 exp\left(-\frac{x^2+y^2}{w^2}\right)\psi_n^*(x,y)exp(j\theta_R(x,y) + jkxsin\theta)\mathrm{dxdy} \tag{5.12}$$

Intensity profile of output guided field could be visualized from figure 5.14, for uniform dopant distribution in the fiber core, by neglecting Kerr nonlinearity, and with uniform random phase distribution. A coupled mode equation given by equation (5.7) is used for the numerical simulation with $20\mu m$ input Gaussian beam diameter full width at half maximum (FWHM). Figure 5.14 shows intensity profiles of guided modes at the output end of the multimode fiber in the absence of gain and Kerr. The output modal power propagation in the logarithmic scale is constant throughout the fiber length, and the spatial intensity profile of output beam is speckled under this scenario.

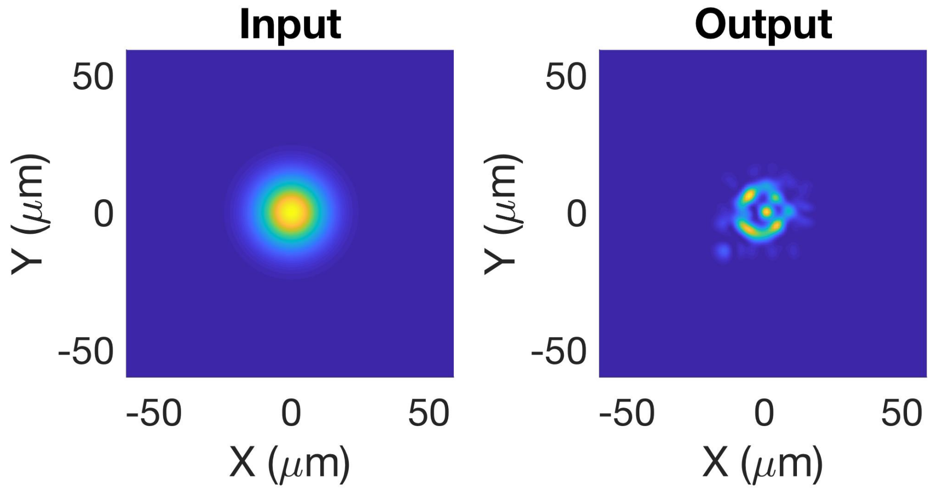

Figure 5.14: Transverse intensity profile of a speckled output guided field at random phase

5.4 Kerr Nonlinear Effect and Beam Cleaning

Optical fibers provide the backbone of today's internet communication networks, and enable compact, low cost light sources for a variety of industrial and biomedical applications. In most of these applications, single-mode fibers are used. Replacing single-mode fibers with multimode fibers leads to a dramatic growth of transmission capacity, and a substantial increase of average power and pulse energy from fiber lasers. However, because of mode interference, multimode fibers suffer from an inherent randomization of the spatial transverse beam profile, leading to a beam scrambling in a complex speckled pattern. Kerr beam self-cleaning exploits the intensity dependent refractive index, or Kerr nonlinearity, of glass fibers to recover the beam quality of a multimode wave, and compensate for temporal modal dispersion.

The physical mechanisms responsible for Kerr induced beam self-cleaning is due to the self-imaging property in GRIN multimode fiber and nonlinear mode mixing effects. In fibers with a parabolic index profile, the equally spaced propagation constants of the modes lead, through the coherent mode beating, to a periodic local intensity oscillation along the fiber, which in combination with the Kerr nonlinearity creates a periodic longitudinal modulation of the refractive index [32]. Modal FWM interactions introduce quasi-phase-matching conditions allowing for numerous mode coupling processes, and thus energy exchanges among the modes, which may favor the fundamental mode of the fiber. Parabolic profile of the refractive index provides the highest value of mode overlap between the input multimode field and the fundamental mode. The energy exchanges, which involve the fundamental mode, become irreversible because of its highest self-phase modulation coefficient; if the initial power distribution is in favour of the fundamental mode at a sufficiently large input power, one observes an irreversible decoupling of the fundamental mode, allowing the power to remain in this mode.

We will demonstrate how to control the beam quality in active graded index multimode fibers, by exploiting the effect of Kerr nonlinear dynamics using coupled mode equations. In a fiber with parabolic index profile, the average intensity will be bell shaped and peaked at the centre of the fibre, this is because light tends to be more concentrated in regions with higher refractive index [66]. Fundamental mode (HG_{00}) completely overlaps with parabolic index profile and is preferably amplified, with respect to the high order modes that show smaller overlap integrals. Numerical simulation in figure 5.15 and 5.16 are in the presence of the nonlinear effect, the beam width of Gaussian input is $20\mu m$ in diameter full width at half maximum (FWHM), with normal input beam inclinations. Random phase distribution is considered and an angle of $3/2\pi$ (the angle θ_R in equation (5.12)) is multiplied by uniformly varying random number. The angle θ_R has to be controlled in such a way that, it should neither be very small nor very large, otherwise the output signal is highly speckled (distorted). The effect of amplification is excluded, as it can be understood from the intensity profile plots of figures (5.15b and 5.16d) that by increasing the input power (P_{in}), a reorganized and stable beam at the output end is observed due to Kerr nonlinear effect. With higher input power, there is high modal interaction (coupling), hence transfer of energy among the modes, particularly to fundamental mode which results in beam reorganization and cleaning at the fiber end. The beam cleaning is not only observed at the output end of the fiber, but even beyond some section of the fiber length.

Beam cleaning is the process that transforms the output speckled beam pattern into a high quality, quasi single mode bell-shaped beam, accompanied by a low power background of high order modes (HOM) [33]. The beam cleaning leads to the transition form a speckled pattern to a more regular pattern where power is concentrated around the axis of the fiber and the cleaned beam remain cleaned for the entire length of the fiber.

There are a well known beam quality metrics for high energy fiber lasers and amplifiers. The M^2 factor also called beam quality factor is a common measure of the beam quality, which represents the degree of variation of a beam from an ideal Gaussian beam. It provides a quantitative means to establish how well a given laser beam will focus or diverge and is always relative to a diffraction limited condition of the same beam size and wavelength. The best possible beam quality is a diffraction-limited Gaussian beam having an M^2 equal to 1. Mathematically, M^2 is given by:

$$M^2 = \frac{\theta \pi w_0}{\lambda} \tag{5.13}$$

where θ is the beam divergence, w_0 is the measured beam waist and λ is the wavelength of light.

The M^2 method is useful for a quick estimate of beam cleaning, but it is not really appropriate especially in the nonlinear regime and for multimode beams. This is because, by definition it only characterizes nearly Gaussian beams. So it is not suitable to characterize the quality of speckled beams, and even of a bell-shaped beams that could result from the superposition of many low order modes. For multimode beams it is necessary to evaluate the distribution of their energy among the individual linear modes of the guiding structure. The proper approach to characterize beam self-cleaning is the mode decomposition method, which provide a more effective approach to qualitatively and quantitatively characterize the beam quality, rather than the M^2 parameter [17] [30]. The existing mode decomposition methods are based on genetic algorithms, adaptive optics, or digital holograms produced by spatial light modulators (SLM).

In our simulations, the quality of the beam is evaluated based on the metrics like, fraction of fundamental mode power evolution relative to that of the high order modes, FWHMI (full width at half maximum intensity) as a function of input power and distance, as well as by observing the iso-intensity surfaces along the fiber length. We have used these beam quality measurement methods together, to evaluate and characterize the beam quality. The iso-intensity surface (the surface at half of the maximum) diameter should decrease across the fiber length, and the fraction of power in the fundamental mode should also be larger than the other high order modes when there is a beam cleaning.

The input powers (P_{in}) and ($\text{P}_{in-Gauss}$) shown in the title of the figures are calculated from the total N guided modes and from the input Gaussian beam respectively as in equation (5.14). The input power P_{in} is determined from the total guided modes amplitude at $z = 0$, and the input power $\text{P}_{in-Gauss}$ is calculated by integrating the input Gaussian beam across the transverse.

$$\begin{aligned} P_{in-Gaus} &= \int_{-\infty}^{+\infty}\int_{-\infty}^{+\infty}\left|A_0\,exp\left(-\frac{x^2+y^2}{w_0^2}\right)exp(j\,\theta_R(x,y)+j\,k\,\mathrm{x}\,sin\theta)\right|^2 dxdy \\ P_{in} &= \sum_{n}^{N}|a_n(0)|^2 \end{aligned} \tag{5.14}$$

Figure 5.15 shows fraction of modal power propagation, and intensity profile of output guided field for an input power of 126W and 1260W. Modal power evolution plot (figure 5.15a) indicates, propagation of power across the fiber length is constant in lower input power case and there is no interference among the modes throughout the fiber length, but there is weak oscillation in figure 5.15c due to relatively high power. Similarly, the intensity profile plots (figure 5.15b and 5.15d) show speckled output beam.

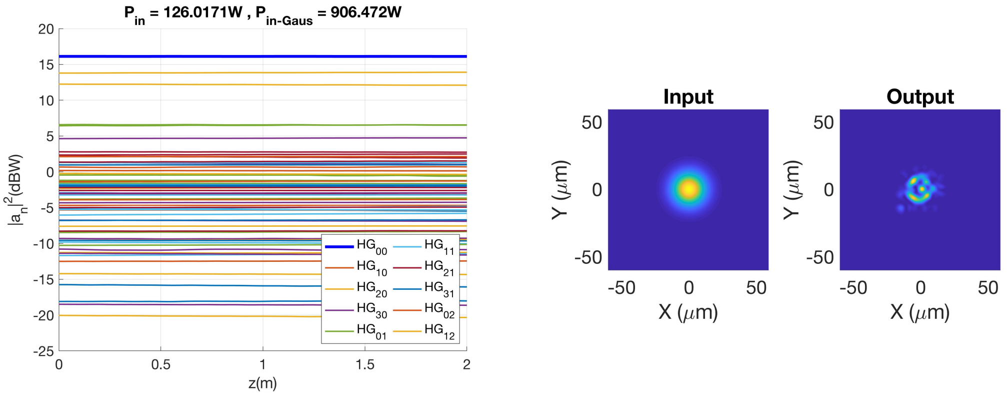

(a) Modal power **(b)** Intensity profile

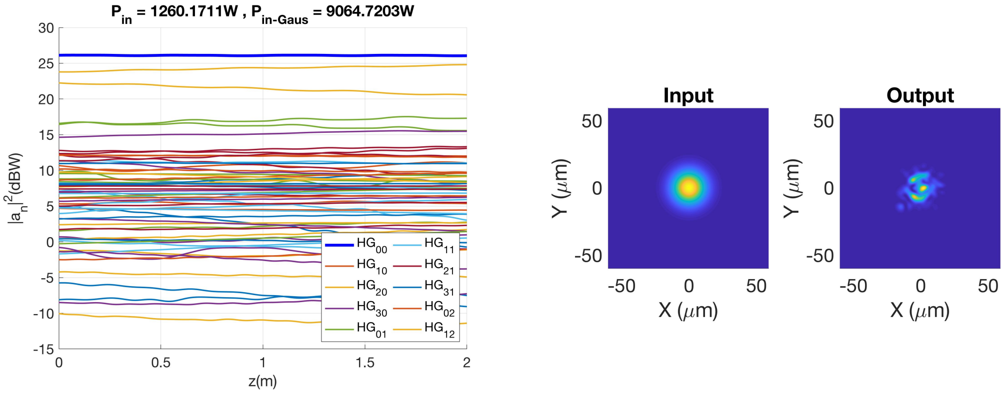

(c) Modal power **(d)** Intensity profile

Figure 5.15: Modal power and intensity profiles with Kerr at low input power

Figure 5.16 presents numerical simulation under the same input conditions as in figure 5.15, but input power, $P_{in}(0)$, is increased for this situation. We can observe from the figures that Kerr nonlinear effect due to high input power enhances modal power coupling which transfers energy from high order modes (yellow curve) to the fundamental mode (blue curve) and among the high order modes. As a result, the power transfers from high order modes to the fundamental mode (HG_{00}) enables beam cleaning, as we can observe from both the intensity profile of output beam (figure 5.16d), and modal power propagation (figure 5.16c) across 2m of fiber length. Under this scenario the gain is neglected, and the transfer of energy is caused by Kerr nonlinear effect when the input power is higher. As we have seen so far, we have showed that at high input power the spatial self-cleaning into the fundamental mode (HG_{00}) occurs due to Kerr nonlinear effect. Further investigations as presented in [47] also reveals self-cleaning into high order mode (LP_{11}) of the fiber arises, due to the nonlinear polarization dependence.

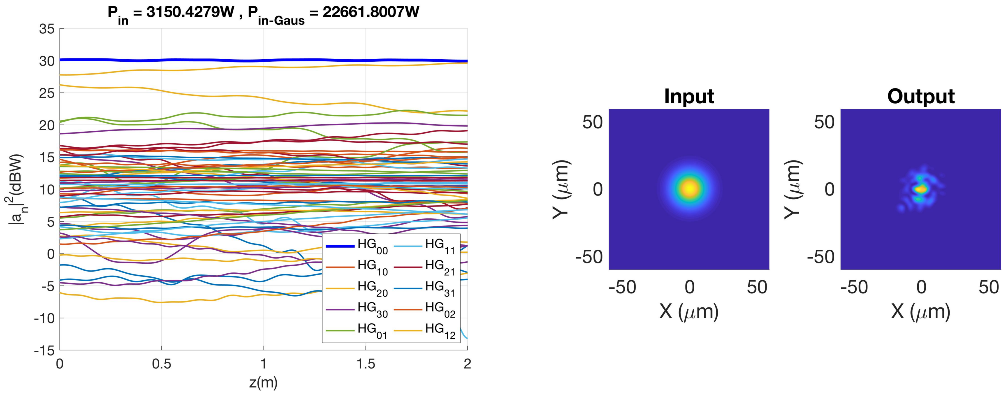

(a) Modal power **(b)** Intensity profile

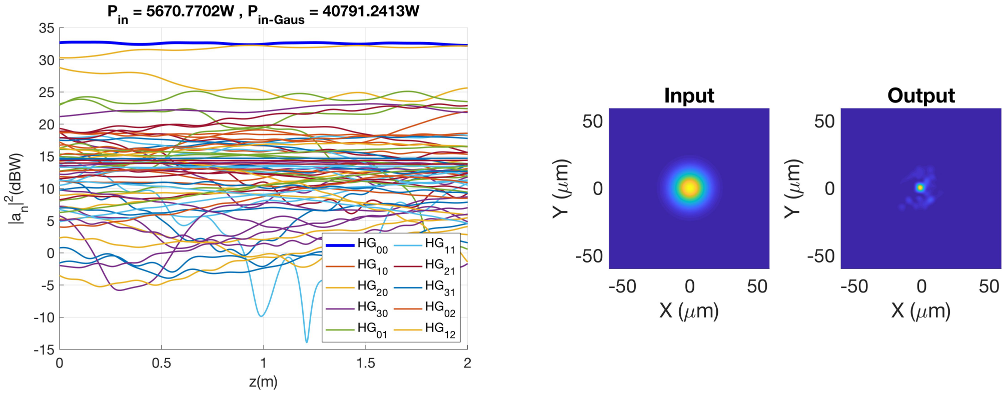

(c) Modal power **(d)** Intensity profile

Figure 5.16: Modal power and intensity profiles with Kerr at higher input power

5.5 Chapter Summary

This chapter discussed the inevitable mode coupling process in multimode fiber amplifiers. There are different factors responsible for this phenomenon, but we considered here the coupling due to non-uniform dopant distribution and Kerr nonlinear effect. We began the study by formulating the coupled mode equations in the presence of those two factors (gain and nonlinearity) as it could be visualized in equations (5.7). After that the gain and Kerr nonlinear effects are introduced in the coupling equation, the effects on the propagating power of each guided modes, and the total output beam situation at the output end of the multimode fiber have been studied. We examined different dopant (gain) distribution inside the multimode fiber core; flat (uniform), parabolic, and ring gain distributions.

Section 5.1 presents the investigation with uniform dopant distribution in the multimode fiber core. The gain per each guided modes are similar, and the modal power propagation shows linear evolution at the initial stage of propagation, but mode coupling shows up at the end fiber length due to Kerr nonlinearity. Figures 5.1 and 5.2 shows this phenomenon. The two figures are different in the sense that the input power is increased in the later, and its evident that at higher input power mode coupling is stronger and Kerr nonlinear effect emerges faster than when the input power is lower. In subsection 5.1.1 we have analysed modal power propagation with backward pumping scheme, and uniform dopant distribution. Figures 5.3 and 5.4 shows the modal power evolution at 565.23W and 5.652kW input power by including the effect of Kerr. It could be understood from the plots that by increasing the input power and considering Kerr nonlinearity the mode coupling becomes stronger.

Moving on to section 5.2, non-uniform gain coupling (parabolic and ring dopant profiles) are described and thoroughly investigated. Figures 5.5, 5.6 and 5.7 presents guided mode power propagation along multimode fiber in the presence of Kerr nonlinearity, for parabolic dopant profile by increasing the input peak power respectively. The coupling of modes is complex when the input power is incremented as it could be clearly visualized from the figures.

Ring dopant profile is another non-uniform gain distribution considered in this chapter and we found out that this dopant profile in general favours amplification of higher order modes and transfers modal powers to the fundamental mode which is facilitated by non-linear and non-uniform gain coupling.

In the final section of chapter 5, we have also explored the beam self-cleaning due to Kerr nonlinear effect. Speckled output beam is obtained as it is observed from figure 5.15 at low input powers, but due to power transfer from other high order modes towards the fundamental mode, a clean beam is obtained when the input power is incremented, as it could be seen from figure 5.16.

Chapter 6

Propagation in Perturbed Active Multimode Fibers

An amplifier device such as a laser gain medium cannot maintain a fixed gain for arbitrarily high input powers, because this would require adding arbitrary amounts of power to the amplified signal. Therefore, the gain is reduced for high input powers, and this phenomenon is called gain saturation or gain compression. If the amplifier operates at power levels such that $P_s(z)/P_s^{sat}(z) << 1$ for all z, the amplifier is said to operate in the unsaturated regime, where $P_s(z)$ is power signal power and $P_s^{sat}(z)$ is saturated signal input power. Saturation refers to the dependence of the gain on the power of the input signal. As the input power increases, the gain decreases until it reaches the saturation point, at which the output power doesn't vary with an increase of the input. The saturation power is typically defined as the input power required in order for the gain to drop by 3dB from the small-signal gain g_0. Beyond the saturation point, the gain falls abruptly and tends towards unity for which $P_{out} = P_{in}$. In the up coming sections we will explore the effects of gain saturation in active multimode fibers using 3D NLSE. Perturbation in multimode fiber that affects propagation of input laser signal is also another main issue to be investigated in our research. Perturbations (disorder) such as bending in multimode fiber is the effect that contributes to generate linear coupling and beam cleaning [60]. Although multimode fibers are resistant to perturbations, these inevitable factors could affect the propagation of modal power, and alter the outcome from the normal expectations.

In this chapter first we will investigate numerical simulation models, coupled mode and 3D NLS equations (universal model governing the evolution of complex field envelopes in nonlinear media) introduced in chapter 1. We will discuss how the two modelling equations perform under the same conditions, to make sure weather we can use them interchangeably. Next we will dig into using 3D NLSE model by considering the effects of gain saturation, disorder and Kerr nonlinearity. Lastly, we will explore the phenomenon of beam cleaning by making use of 3D NLSE with the effects of disorder, saturated gain and Kerr nonlinearity. Our numerical simulation results are visualized for further analysis with respect to theoretical modelling equations, and laboratory results are also presented for comparison.

6.1 3D NLSE and Coupled Mode Equations

In Chapter 2 we have seen that the coupled mode equations are used for numerical simulations with mode expansion, where gain and nonlinearity are the only two coupling factors investigated. Here we will compare the difference of using coupled mode equations and 3D NLSE tools to conduct numerical simulations. The 3D NLSE we analysed accounts for disorder and saturated gain, but the coupled mode equations do not consider these effects (consider only gain and nonlinearity). For this reason, we neglected the presence of disorder and saturated gain in the 3D NLSE and used equal parameters in both equations. A Gaussian beam diameter full width at half maximum (FWHM) of $40\mu m$, uniform dopant distribution, no random phase and normal inclination of input beam are considered. Gain and Kerr nonlinear effects are included in both numerical tools and a total of 81 guided modes are propagated across a 2m GRIN MMF. The guided modes are excited differently in coupled mode equations and 3D NLSE. Gaussian beam is projected on each Hermite-Gaussian modes in the case of coupled mode equations, whereas Gaussian beam is projected on the modes after propagation in 3D NLSE. Furthermore, we will increase the number of guided modes and reduce the input beam diameter, to confirm how the two equations can be used interchangeably (that is if they perform similarly).

To begin with, let's use 81 guided modes and $40\mu m$ input beam diameter and then compare the power evolution of modes particularly that of the fundamental mode. Similarly we will see intensity profile of input and output guided modes by using the two modelling equations. As it could be observed from figure 6.1 the blue curve represents fundamental mode power fraction evolution when coupled mode equations are used, and the dashed red curve represents fundamental mode power in logarithmic scale when 3D NLSE is implemented. Likewise, figures 6.1c and 6.1d are intensity profiles of input Gaussian beam and intensity profiles of guided output beam, with coupled mode equation and 3D NLSE.

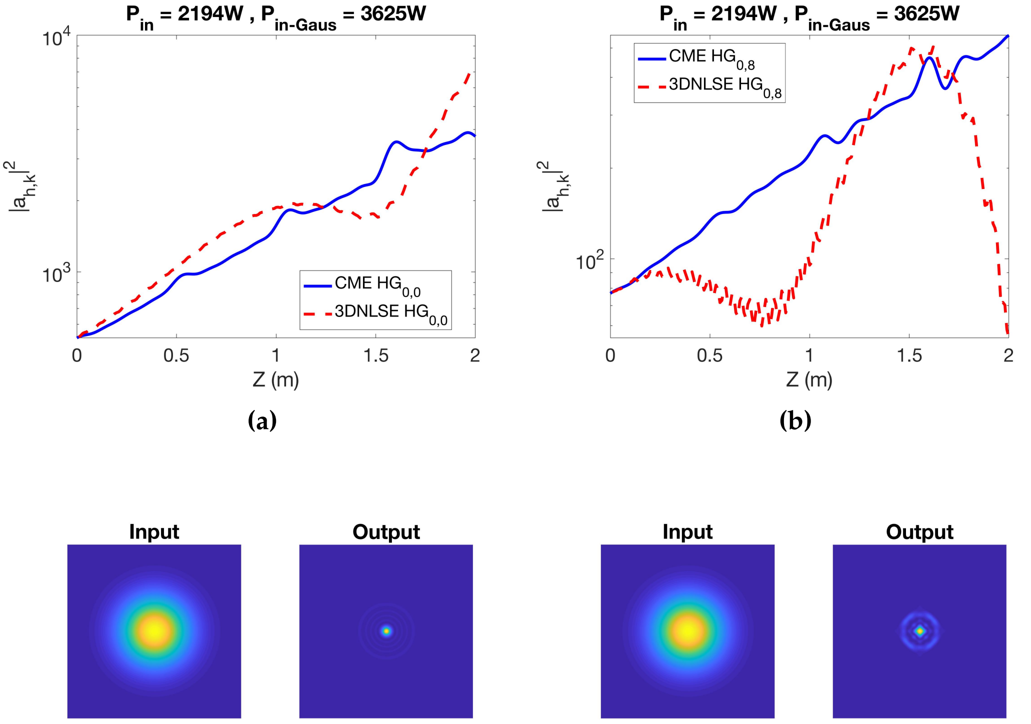

(a) **(b)**

(c) **(d)**

Figure 6.1: Numerical simulation comparison in the presence of gain and Kerr: (a) Fraction of fundamental modes power propagation using CME (coupled mode equation) and 3D NLSE (b) Fraction of high order mode power propagation using CME and 3D NLSE (c) Intensity profile of input beam and output guided field using 3D NLSE (d) Intensity profile of input beam and output guided field using CME

Now reducing the Gaussian beam full width at half maximum (FWHM) diameter to $20\mu m$, we will demonstrate numerical simulation results using both coupled mode and 3D NLSEs. Effects of Kerr and gain without saturation are included, with 81 total guided modes in both equations. Like the previous simulation, similar input initial conditions are considered for comparison.

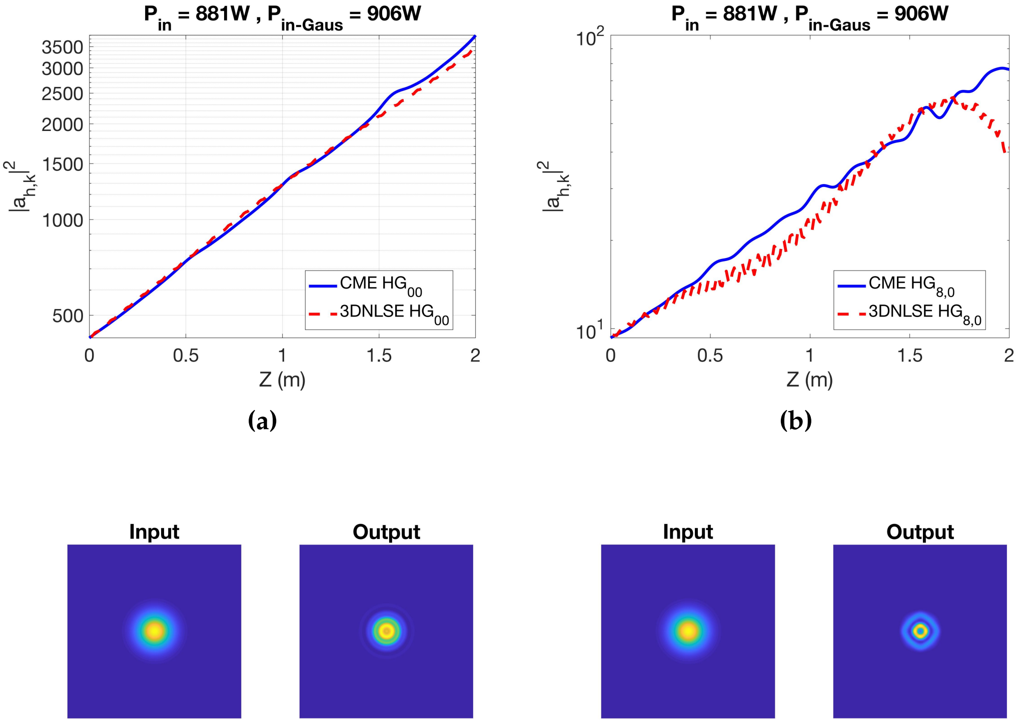

(a) **(b)**

(c) **(d)**

Figure 6.2: Numerical simulations using CME and 3D NLSE in the absence of saturated gain and disorder: (a) Fraction of fundamental modes power propagation using CME (coupled mode equation) and 3D NLSE (b) Fraction of high order mode power propagation using CME and 3D NLSE (c) Intensity profile of input beam and output guided field using 3D NLSE (d) Intensity profile of input beam and output guided field using CME

To summarize, as we can understood from the previous consecutive figures, it is clear that figure 6.2 shows an agreement of fundamental modes power propagation in 2m of fiber length for the two models. This is achieved by reducing the beam width of input Gaussian beam and increasing the number of guided modes. In the same figure it is shown that the input powers (P_{in}) and $P_{in-Gaus}$ calculated by using equations in chapter 4 are getting closer by using reasonable number of modes and input Gaussian beam width. Under such conditions, computed numerical simulations using coupled mode and 3D NLS equations resembles. In addition, the time complexity, though it could be reduced down are comparable, which roughly scales as $N^3 - N^4$ with N being the number of modes included in the simulation [32] [34]. In fact, modal-expansion and coupled mode method displays a nearly linear scaling of numerical complexity with mode number. The numerical solution algorithm of 3D NLSE and its complexity was analysed in [32] showing that, although in principle the time complexity grows proportionally to the fourth power of the number of modes N, it can be reduced to scale as N^3 by exploiting the fiber symmetries and selection rules. Likewise, the time complexity of coupled mode expansion method roughly scales as $N^3 - N^4$ [34].

6.2 3D NLSE with Gain Saturation and Disorder

Multimode nonlinear propagations will be studied, by considering the effects of saturated gain and disorder, using 3D MM-GNLSE other than the coupled mode equations we analysed in gain and nonlinear coupling. In highly multimode fiber, it may be computationally much more efficient to use a direct numerical solution of the 3D NLSE. In the case of a GRIN MMF, the equation for the complex field envelope $E_g(x,y,z)$ [$\sqrt{W}/\mathrm{m}$] is as follows (such equation is also called the Gross-Pitaevskii equation)[32].

$$i\frac{\partial E_g}{\partial z} + \frac{1}{2\beta}\nabla_\perp^2 E_g + \frac{1}{2}\frac{g_0}{1+\frac{I(x,y,z)}{I_{SAT}}}E_g - \beta\Delta(\frac{r}{a})^2 E_g + \frac{\omega n_{2kerr}}{c}(1-f_r)|E_g|^2 E_g = 0 \quad (6.1)$$

where $\nabla_\perp^2 = \partial_x^2 + \partial_y^2$ is transverse Laplacian, $\beta = \frac{\omega n_1}{c}$ is propagation constant, ω is carrier frequency in rad/s, $I_{SAT} = \frac{F_{SAT}}{\tau_{pulse}}$ saturation intensity, F_{SAT} is saturation fluence, τ_{pulse} is pulse duration, g_0 is small signal gain, $\Delta = \frac{n_1^2-n_2^2}{2n_1^2}$ is the relative index difference, a is the fiber core radius ($26\mu m$), n_1 is the maximum core refractive index 1.47, n_2 is the cladding refractive index 1.457, n_{2kerr} is non-linear refractive index having a value of 3.2×10^{-20} m^2/W for fused silica used to fabricate silica fibers, f_r is Raman fraction found to be about 0.18 for silica fibers. Equation 6.1 is a powerful tool to study the effects of diffraction, active medium, waveguide and Kerr nonlinearity in pulse propagation. Furthermore, it's used to investigate the propagation of optical pulses in non-linear active multimode fiber in the presence of saturated gain and disorder.

Disorder arises from stochastic density fluctuations of the glass and dopants, as well as small manufacturing errors and environmental effects such as bending, twisting, and core ellipticity. The effect of disorder is included here in our numerical model by changing the transverse profile of the refractive index by deforming the circular core into an elliptical core. In other words, the fiber is perturbed by elliptical deformation along the orientation of the coordinate axes which varies randomly. Here it should be understood that we didn't make statistical study, however we are able to change the fiber refractive index profile, by changing the orientation of the ellipse randomly. This is how the effect of disorder is included in the 3D NLSE. In fact, the model of disorder is not directly introduced into equation (6.1) rather it is included through the waveguide refractive index profile change. Still the 3D NLSE given by equation (6.1) is used, but we can insert an arbitrary refractive index given by equation (6.2), which is different from a parabolic index profile. Rotating an ellipse by certain angle θ_{rand} provides the following coordinate points, and the corresponding refractive index is given by equation (6.2).

$$x_e = x\cos(\theta_{rand}) - y\sin(\theta_{rand})$$

$$y_e = x\sin(\theta_{rand}) + y\cos(\theta_{rand})$$

$$n^2(x_e, y_e) = n_1^2(1 - 2\Delta(\frac{x_e^2}{a^2} + \frac{y_e^2}{b^2})) \quad (6.2)$$

The model considered here includes a coarse step of 5mm where the fiber is deformed, to introduce random variations in the fiber on both polarization axis. In other word, the orientation of the ellipse is randomly changed every 5 mm, and the random orientation of the ellipse is a good model (despite its arbitrariness) as it can be deduced from the fact that, in the linear regime, the numerical solution shows the formation of speckled patterns at the fiber output. In this model the gain, which could be non uniform in the transverse coordinate, is considered together with disorder (linear random coupling) and Kerr effect (nonlinear coupling). In these numerical simulations the input Gaussian beam is straight and not tilted. Disorder causes coupling between modes with similar propagation constants, primarily within mode groups. Fundamental mode is less affected by disorder, while the high order modes are the most affected [66].

The 3D NLSE equation (6.1) is a simplified case of GNLSE with only spatial dependency, the Brillouin and Raman scattering which are time dependent are not included. We are aware of these effects at high input powers. However, there was no evidence of any role of the Raman effect in the beam reshaping process, and beam cleaning can be achieved in the absence of this dissipative process [33]. Even with the strong assumption of neglecting time and spectrum, the numerical simulations require a very heavy computational burden due to large fiber cross-section and large number of modes, and to numerically observe the onset of beam cleaning we have to increase the input power. In order to speed up the simulations we have shortened the fibers, by limiting their lengths to a few meters, from 10m in the experiments to 2m in the simulations, and we have increased the power to obtain the same nonlinear evolution observed in the experiments.

The Raman threshold, the power level at which the Raman process becomes stimulated and transfers most of the signal power to the Stokes wave is estimated using equation(6.3)[2] for the continuous wave (CW) case.

$$P_{Rth} = 16\frac{A_{eff}}{g_R L_{eff}} \tag{6.3}$$

where g_R s the Raman gain coefficient, A_{eff} is the effective core area, and L_{eff} is effective length. For short segment of fibers, as in our case, the effective interaction length L_{eff} coincides with the physical length of the fiber L.

By applying equation (6.3) the Raman threshold power at a relatively short and long fiber lengths of $L_{eff} = 2m$ and $L_{eff} = 10m$ using $g_R = 10^{-13}m/W$ and core radius of $26\mu m$ are 170kW and 34kW respectively. The results for $L_{eff} = 10m$ shows that the Raman threshold power remains below the laser power used in the experiments. It is then a reasonable assumption to neglect the Raman contribution in the numerical simulations.

Similarly, the Brillouin threshold power P_{Bth} can be estimated using the following equation

$$P_{Bth} = 21\frac{A_{eff}}{g_B L_{eff}} \tag{6.4}$$

where g_B is the Brillouin gain coefficient. The Brillouin effect which is efficient only with continuous wave signals or extremely long pulses was not observed in the experiments we conducted.

Mode coupling enables transfer of energy from one ideal mode to another during propagation. The coupling strength between modes depends on the difference between the two modal propagation constants. Mode-coupling in GRIN MMF is primarily local, where the perturbation may strongly couple modes having nearly equal propagation constants, but weakly coupled modes have highly unequal propagation constants [27].

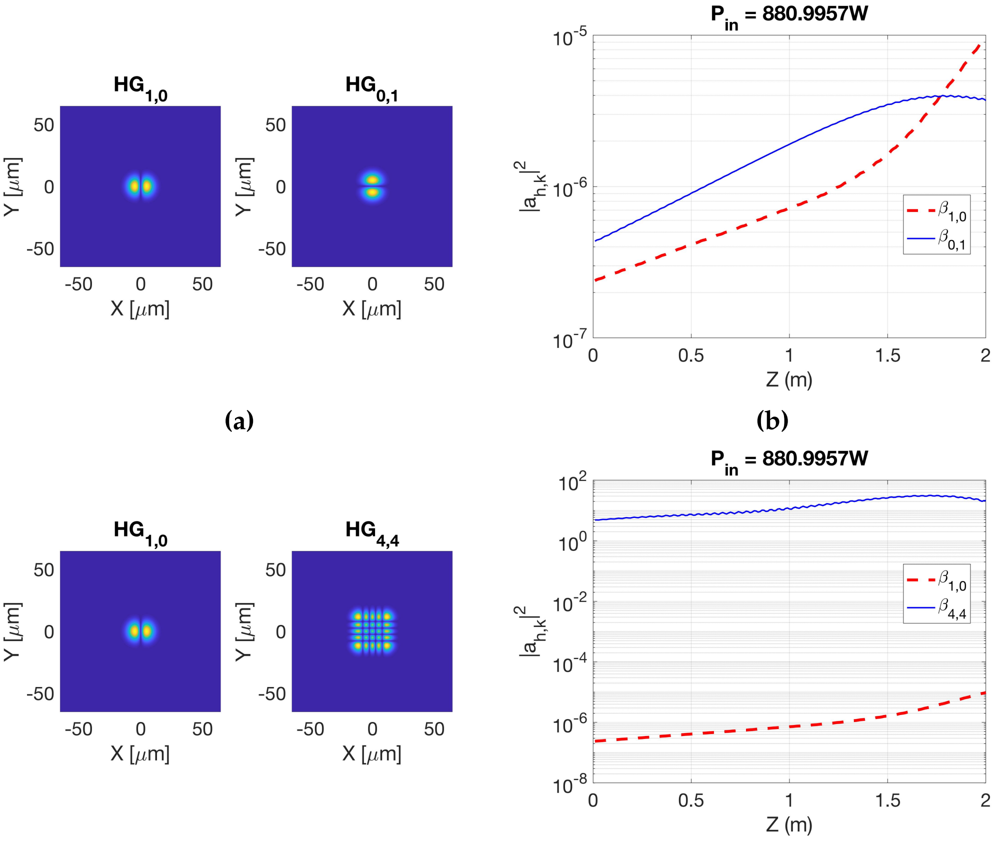

(a) (b)

(c) (d)

Figure 6.3: Mode coupling among similar and different propagation constants in the presence of Kerr and gain: (a) Hermite-Gaussian mode profiles (b) Mode coupling between similar propagation constants (c) Two different mode profiles (d) Mode coupling between different propagation constants

6.3 Gain with Saturation

The effect of saturated gain in equation (6.1) are accounted by:

$$\frac{\partial E_g}{\partial z} = \frac{1}{2}\frac{g_0}{1+\frac{I(x,y,z)}{I_{SAT}}}E_g \tag{6.5}$$

where the saturation intensity I$_{SAT}$ $= F_{SAT}/\tau_{pulse}$, F$_{SAT}$ is saturation fluence in J/m^2 and τ_{pulse} is pulse duration in second. The F$_{SAT}$ and τ_{pulse} in our numerical simulations have a values of $3.1744 \times 10^5 J/m^2$ and $500ps$ respectively. To neglect the gain saturation effect we set $\frac{I(x,y,z)}{I_{SAT}}$ in equation (6.5) to zero and we obtain, $\frac{\partial E_g}{\partial z} = \frac{1}{2}g_0 E_g$, where g_0 is small signal gain.

In this section we will investigate the effect of saturated gain using 3D NLSE. In most of the doped multimode fibers studied, the saturated gain effect is not included [32]. In our study we will explore saturated gain and other effects in Yb^{3+} doped multimode fiber amplifiers. First let's study the effects of saturated gain, disorder, but without Kerr nonlinearity in the 3D NLSE. Our numerical simulation considers uniformly distributed Yb^{3+} ions across the core cross section of the graded index MMF. Gaussian input beam of $40\mu m$ in diameter FWHM, and 25 guided modes are propagated across 2m fiber length without input beam inclination angle.

Higher gain at distance z, and modal power is obtained in the absence of saturated gain as we can observe from figure 6.4, and on the contrary, low modal power is obtained when saturated gain is considered. Furthermore from the same figure, it is understood that mode coupling is stronger due to the presence of both linear (disorder and gain) and nonlinear coupling. The red dotted curves in figure 6.4a shows power evolution of high order modes ($HG_{1,0}$ and $HG_{0,1}$) and energy transfer between those modes. In figure 6.4a the curves in cyan and blue shows the power evolution of high order and fundamental modes.

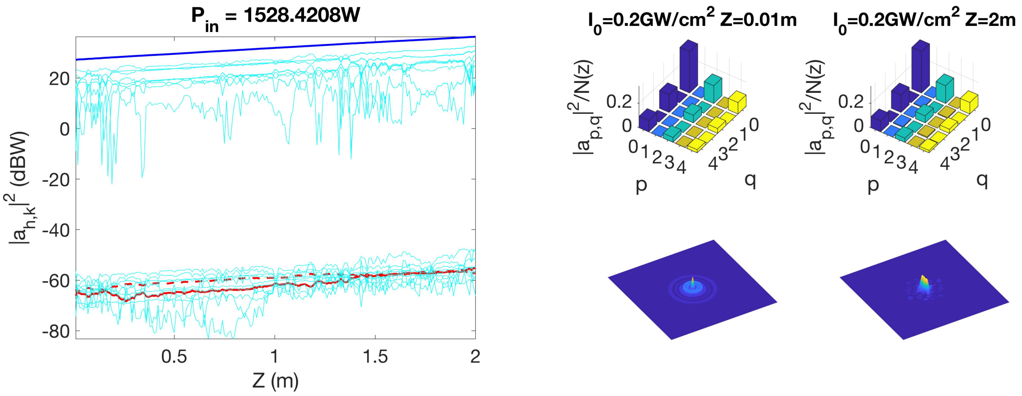

(a) (b)

Figure 6.4: Modal power propagation and power ratio including gain, disorder and saturation, but excluding Kerr: (a) Modal power propagation (b) fraction of modal power at input and output end of fiber length

6.4 Saturated gain and Kerr

Kerr non-linear effect is a factor responsible for mode coupling and beam cleaning in graded index multimode fibers as we have seen in the previous chapter, but the effect of saturated gain was not considered in the coupled mode equation (5.7). Now in 3D NLSE both nonlinear and saturated gain are included, in which the Kerr effect is modelled by:

$$\frac{\partial E_g}{\partial z} = \frac{i\omega n_{2kerr}}{c}(1 - f_r)|E_g|^2 E_g$$

where n_{2kerr} is nonlinear refractive index, for fused silica used to fabricate silica fibers having a value of 3.2×10^{-20} m^2/W, f_r is Raman fraction found to be about 0.18 for silica fibers, and ω is carrier frequency in rad/s. We investigated the effect of Kerr by excluding (including) nonlinear refractive-index from 3D NLSE, but keeping the factors of gain, gain with saturation and disorder in the two cases.

Figures 6.4 and 6.5 illustrates fractional modal power plots in the absence and presence of Kerr nonlinearity respectively. In the presence of Kerr as shown in figure 6.5c, the high order modes (dashed red and solid cyan curves) experience coupling and modes exchange power. On the contrary, smooth evolution of modes is observed in the absence of Kerr as it could be understood from figure 6.4a. The effect of Kerr could clearly be observed more by increasing power at the input side of the fiber length.

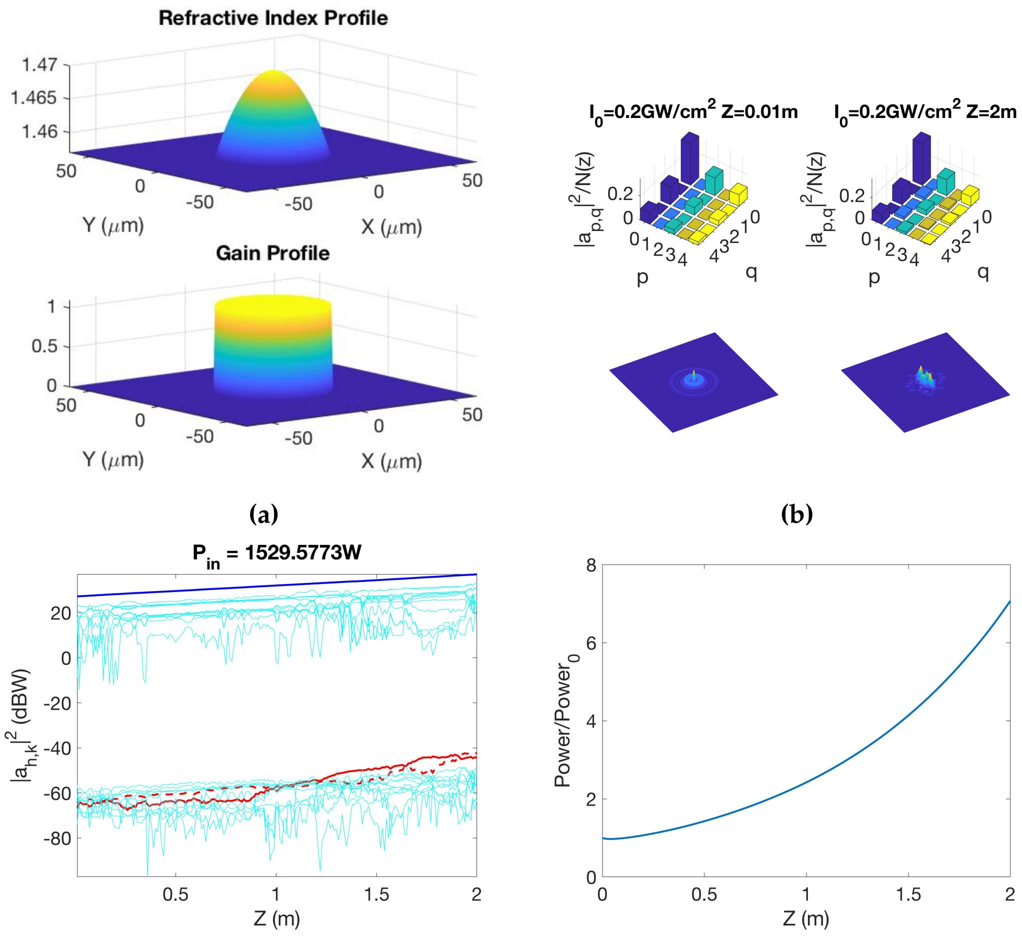

(a)

(b)

(c)

(d)

Figure 6.5: Modal power propagation and power ratio including gain, Kerr and disorder but excluding saturation: (a) Refractive index and gain profile (b) Fraction of modal power in bar plots (c) Modal power propagation (d) Normalized power across propagation distance

6.5 Kerr Beam Self-cleaning

Apart from gain and Kerr nonlinear effects in graded index multimode fibers, we also examined the impact of saturation and disorder using 3D NLSE. The technique of introducing disorder, that causes linear coupling is explained in section 6.2 of this chapter. In this section we will investigate beam cleaning in the presence of Kerr by neglecting disorder (perturbation) at the beginning and introducing the effect of disorder next in active graded index multimode fiber.

Now let's see beam cleaning and mode power evolutions by neglecting the effects of disorder (perturbation) to begin to understand more the beam cleaning technique. numerical simulations are performed using 3D NLSE with gain and Kerr, excluding disorder and saturation, with Gaussian input beam of 10μm radius FWHM, 26μm core radius with 81 total guided modes, and increasing the input power consequentially. It could be seen from figure 6.6b that by excluding linear coupling (disorder) and saturated gain the modal power evolution is smooth (mode coupling is low), with respect to propagation in the presence of disorder. By increasing the input power as it is shown in figure 6.7c, the fact that due to Kerr nonlinear effect the coupling of modes starts to emerge. Increasing the input power further, we can observe from figures 6.7a and 6.7b that the beam cleaning is evident both in the bar graph and intensity profiles plot.

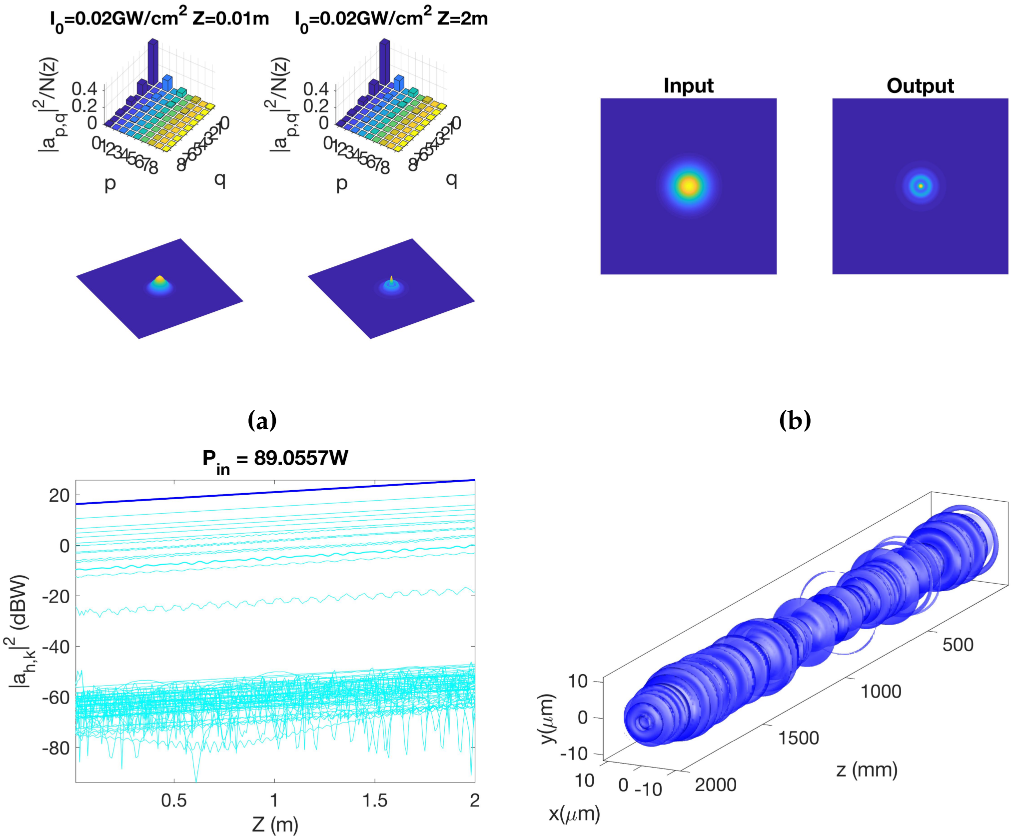

(a) (b) (c) (d)

Figure 6.6: Simulations with Kerr and gain, in the absence of disorder and saturation: (a) Fraction power of modes at beginning and end of fiber length (b) Intensity profile plot of input and output guided modes (c) Fractional power evolution of modes (d) Iso-intensity plot across fiber length

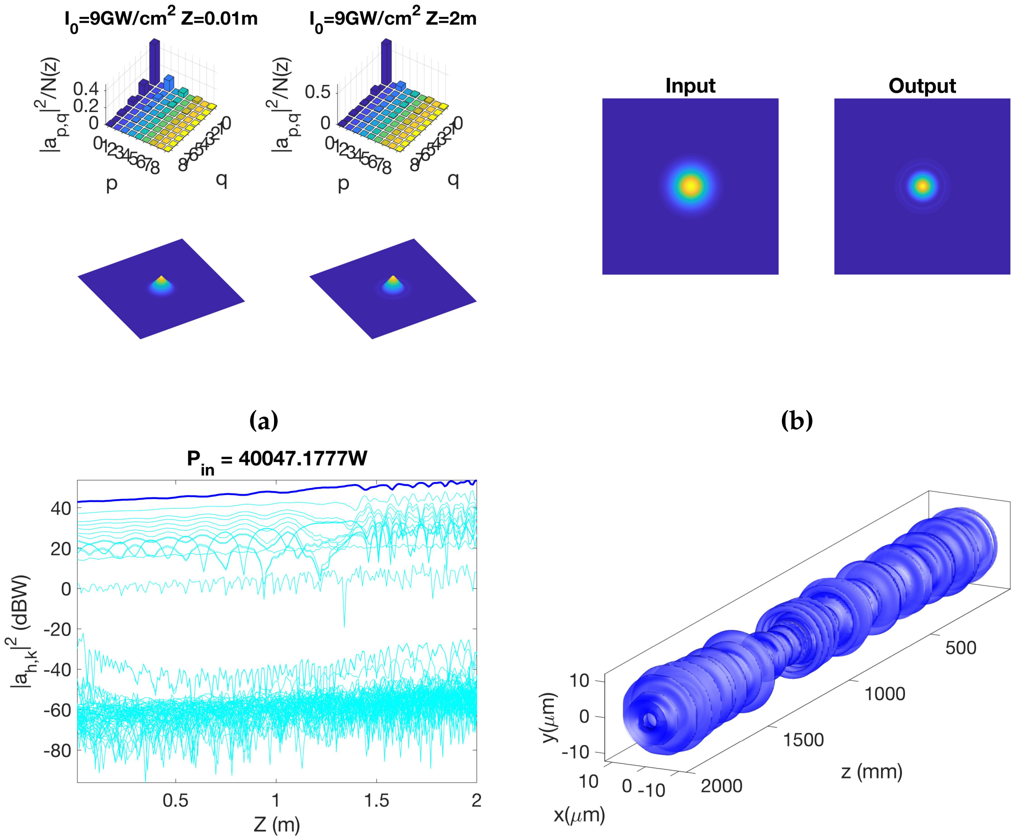

(a) (b)

(c) (d)

Figure 6.7: Simulations with Kerr and gain, in the absence of disorder and saturation: (a) Fraction power of modes at beginning and end of fiber length (b) Intensity profile plot of input and output guided modes (c) Fractional power evolution of modes (d) Iso-intensity plot across fiber length

In the first part of this section we have exploited the 3D NLSE by neglecting the effect of disorder, now let's consider perturbation and explore further the beam cleaning phenomenon. In figure 6.8a, it's shown that at z=0.01m and z=2m the fundamental mode carries a large power fraction, but there are high order modes, as well. It's also observed from the figure 6.9 that along the 2m of fiber the beam width does not change. From the studies on multimode passive fibers, we know that when there is beam cleaning, the output beam width shrinks [33]. On the other hand in figure 6.10a, we can see from the first figure the power fraction of 81 total guided modes at the beginning (z=0.01m) where there are both fundamental as well as high order modes, but at the output end (z=2m) of the fiber only the fundamental mode is observed (the tall blue bar): high order modes are suppressed and a clean beam is obtained. Similarly, in the lower part of figure 6.10a, the beam can be clearly seen reshaping itself after half of the fiber length. Furthermore, the beam at the fiber end (z=2m) have reduced beam width than at the fiber input (z=0m) as it could also be observed from figure (6.11d and 6.11a), which confirms the beam cleaning phenomenon.

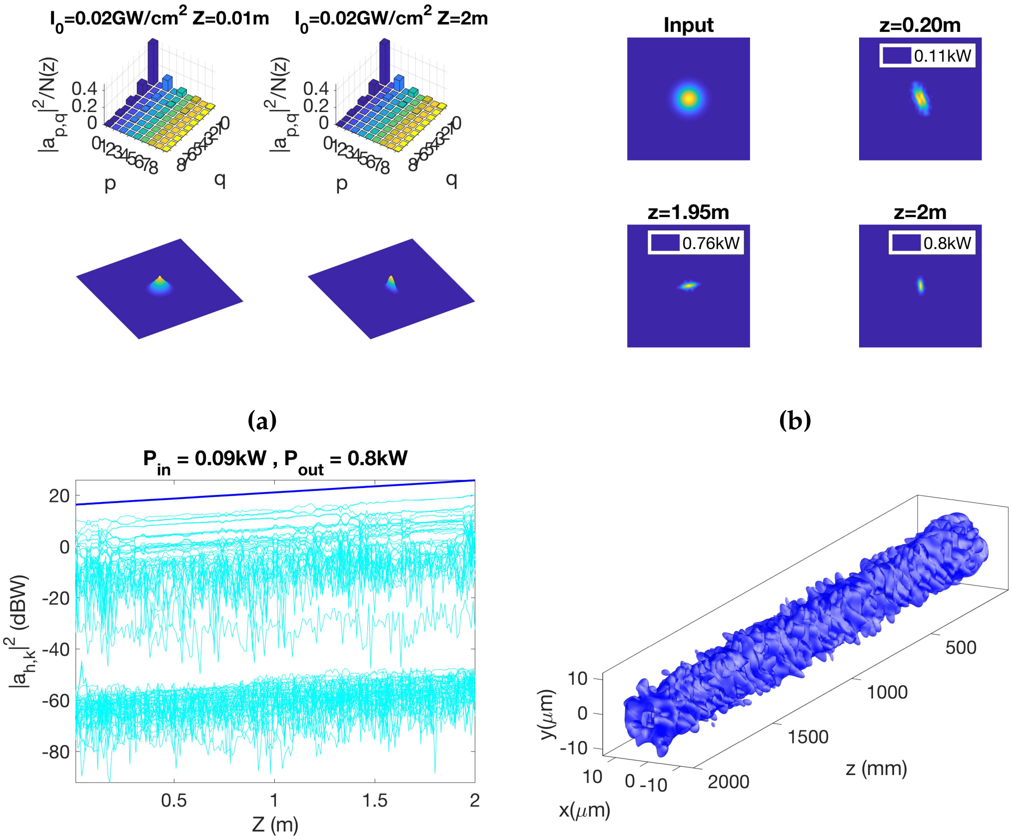

(a) (b)

(c) (d)

Figure 6.8: Kerr, gain and disorder without saturation: (a) Fraction power of modes at beginning and end of fiber length (b) Intensity profile plot of input and output guided modes (c) Power evolution of modes (d) Iso-intensity plot across fiber length

To further realize the beam cleaning phenomena in perturbed multimode fibers we can compare the mode diameter with respect to the input laser. It is verified that the beam cleaning can be confirmed when the beam width is reduced across the fiber length [33], the beam width reduces when beam cleaning takes place. Figures 6.9 and 6.11 show the beam width of the guided input laser at different spatial distances from z=0 to z=2m (fiber end). The beam width is reduced along the propagation distance due to the beam cleaning phenomenon.

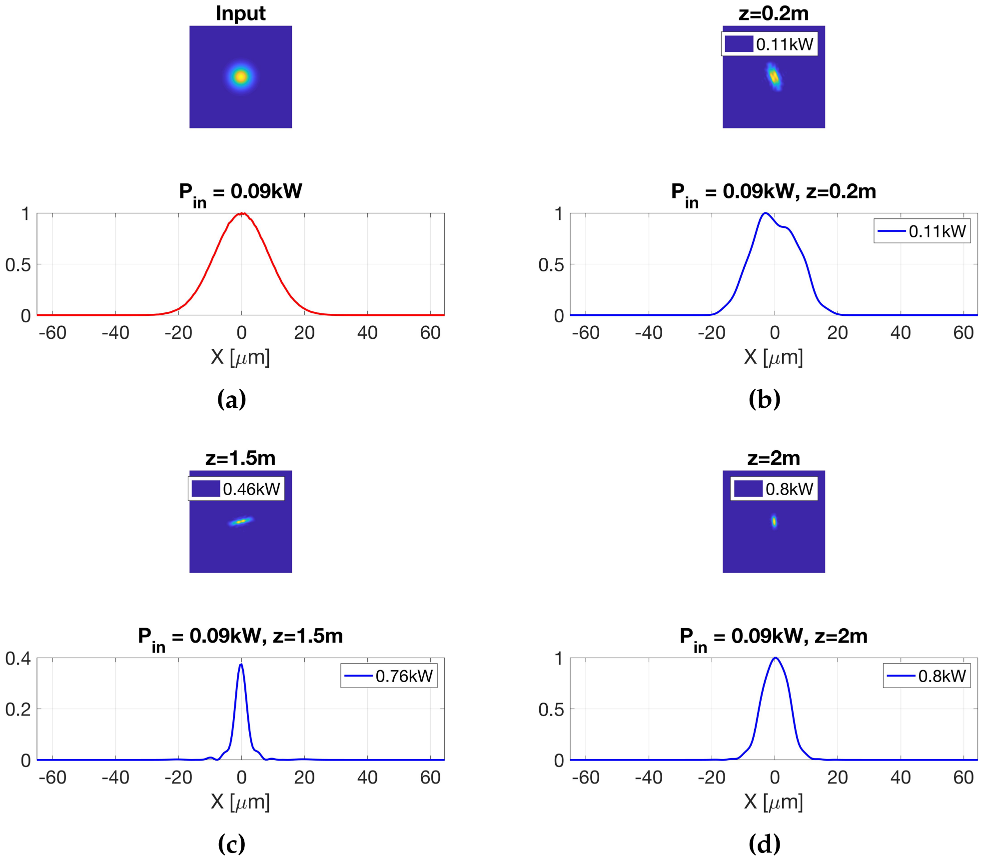

(a) (b) (c) (d)

Figure 6.9: Beam width as a function of input and output power

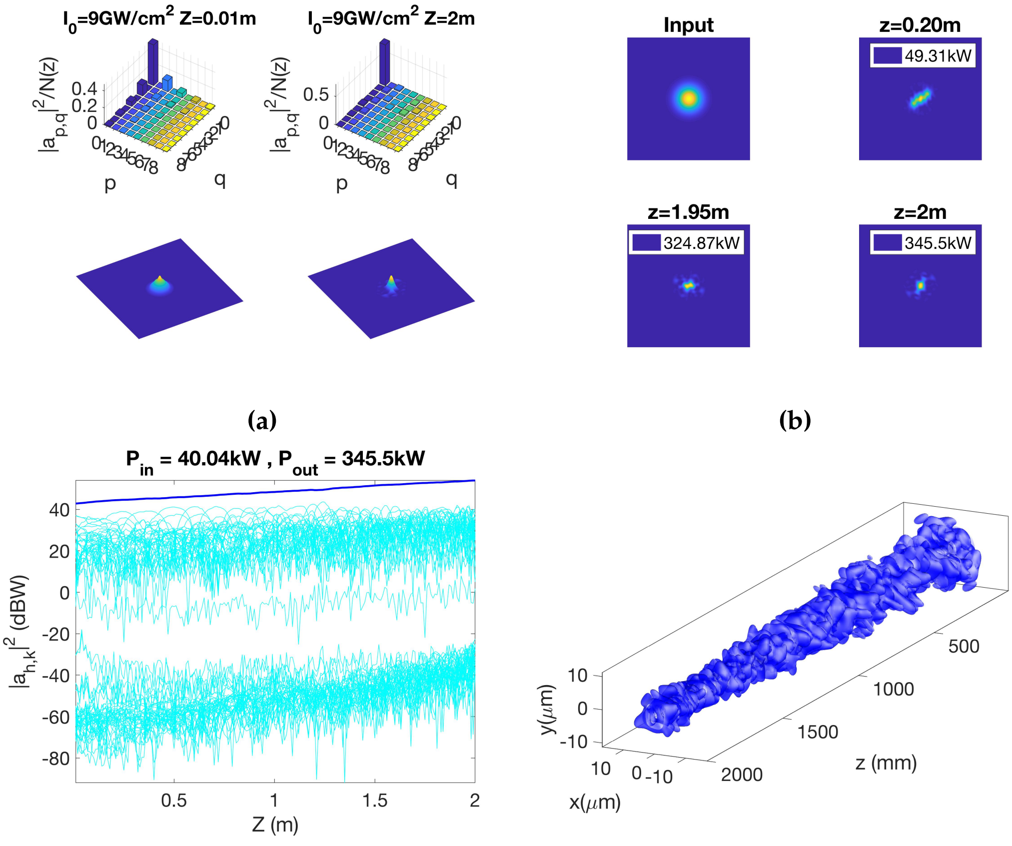

(a) **(b)**

(c) **(d)**

Figure 6.10: Kerr, gain and disorder without saturation: (a) Fraction power of modes at beginning and end of fiber length (b) Intensity profile plot of input and output guided modes (c) Fractional power evolution of modes (d) Iso-intensity plot across fiber length

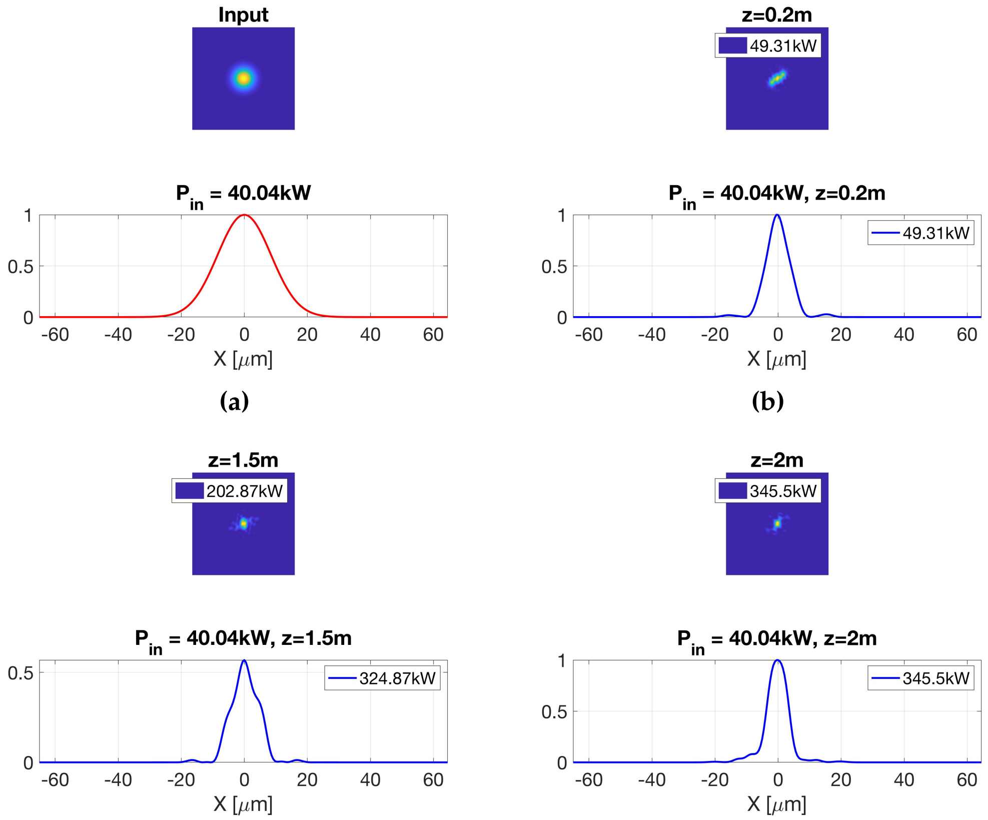

(a) **(b)** **(c)** **(d)**

Figure 6.11: Beam width as a function of input and output power

Figure 6.12 shows FWHMI (Full Width at Half Maximum Intensity) diameter of Gaussian input signal as a function of output power and distance along the propagation direction, where the output power is indicated on the plots of figure 6.13 at each fiber distance z. As it could be observed, the FWHMI diameter decreases from initial 20μm (input Gaussian beam width) down to less than 10μm as the output power increases along the evolution direction. At a fiber length of z=0.7m the power is found to be 85.51kW (figure 6.13a), whereas at z=1.8m the power is 280.1kW (figure 6.13e), and the beam width is significantly reduced than it was at z=0, which clearly shows the beam self-cleaning phenomenon [33]. Similarly, the FWHMI width decreases along the propagation direction as it could be clearly seen in figure 6.12b. In general, the beam width decreases along the fiber propagation direction under the same input power.

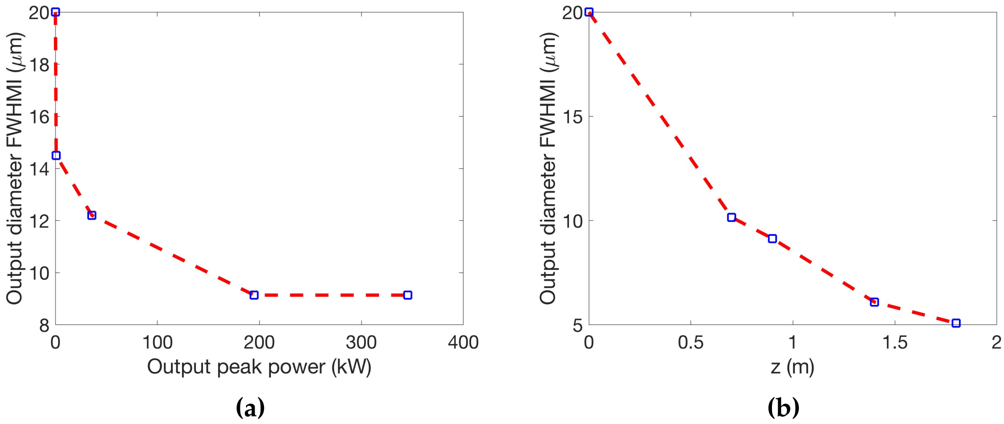

Figure 6.12: FWHMI as a function of output power and distance plot: (a) FWHMI vs output peak power (b) FWHMI vs distance, for the intensity profile plotted in figure 6.13.

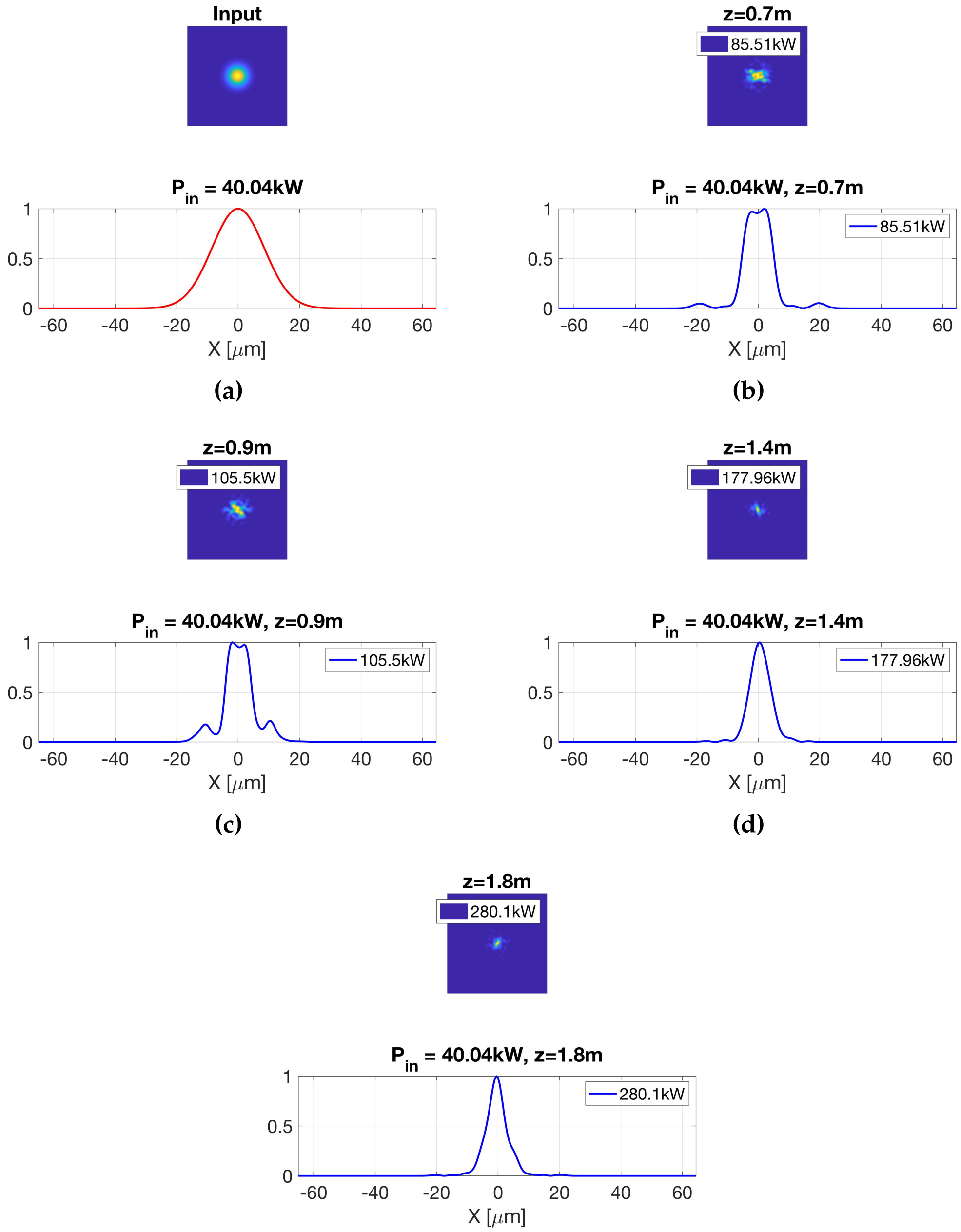

(a) (b) (c) (d) (e)

Figure 6.13: Beam width as a function of input and output power at different distances across fiber propagation

6.6 3D NLSE Coupled with Population Density

Equation (6.1) is a good approximation because it accounts for saturation, nevertheless a more complete model based on the coupling between pump, population in the excited state and electric field envelope can lead to more accurate results. The model presented here is the result of a combination between transversally resolved rate equations including the pump power $P_p(z)$ and propagation equation for the signal electric field $E_g(x,y,z)$. By assuming pumping in the forward direction, the pump evolution is given by:

$$\frac{dP_p}{dz} = \left[(\sigma_{ap} + \sigma_{ep}) \frac{\int_S N_2(x,y,z) ds}{A_{Cl}} - \sigma_{ap} \frac{\int_S N_T(x,y) ds}{A_{Cl}} \right] P_p - \alpha_p P_p \tag{6.6}$$

where σ_{ap} and σ_{ep} are absorption and emission cross sections at the pump wavelength, N_1 (N_2) is the ground (excited) Yb ion density, $N_T = N_1 + N_2$ is the total Yb density, A_{Cl} is the inner cladding area, and α_p is the linear pump absorption. Since we consider that the pump is uniformly distributed (i.e. it does not depend on x, y) in the inner guiding cladding, the pump intensity reads as $I_p(z) = P_p(z)/A_{Cl}$. As the pump power is uniformly distributed inside the inner cladding of radius $150\mu m$ and inner core radius of $26\mu m$, the fiber is cladding pumped with continuous pump power. In equation (3.10) the population varies along longitudinal coordinate z, but in equation 6.6 the density of ions (N_2 and N_1) depends on the three spatial coordinates. Here the populations N_1 and N_2 vary not only along the longitudinal coordinate z but also in the transverse x, y plane, and the two integrals are calculated on the section S where doping is present, as it can be seen in equation (6.6). Even if different doping profiles are possible, there are technological limitations and challenges to manufacture and obtain such fibers in the market, so the easiest and most available doping is where the dopant is uniformly distributed across the core. The pump is continuous wave and we assume a steady state behaviour of the amplification, nevertheless, when writing the rate equations, we must take into account that the signal pulses have a duration τ_{pulse}, a repetition rate T and an intensity which is time dependent $I_s(x,y,z,t)$. This is an approximation in this context, although generally adopted in fiber lasers [54]. We can define the time-average signal intensity as $\bar{I}_s(x,y,z) = 1/T \int I(x,y,z,t)\, dt \simeq \max_t[I(x,y,z,t)]\, \tau_{pulse}/T$. Thanks to the previous approximation the density of excited ions $N_2(x,y,z)$ can be explicitly written as function of pump and signal intensities:

$$N_2(x,y,z) = N_T \frac{\sigma_{ap} I_p(z) + \sigma_{as} \bar{I}_s(x,y,z) \lambda_s/\lambda_p}{(\sigma_{ap} + \sigma_{ep}) I_p(z) + (\sigma_{as} + \sigma_{es}) \bar{I}_s(x,y,z) \lambda_s/\lambda_p + P_\tau} \tag{6.7}$$

where τ is the excited level lifetime and $P_\tau = hc/(\lambda_p \tau)$, where h is the Planck's constant and c the speed of light. It should be noted that the population density equations are different based on the pumping scheme (core or cladding), and based on the pulsed signal approximation techniques. Equation 4.3 and 6.7 are similar, except in the later the signal intensity is given by a time averaged approximation of a pulsed signal intensity. The evolution of the complex envelope of the electric field $E_g(x,y,z)$, normalized in such a way that the intensity is $I(x,y,z) = |E_g(x,y,z)|^2$), is governed by the following equation:

$$\frac{\partial E_g}{\partial z} = \frac{i}{2k_0}\left\{\nabla_\perp^2 E_g + \left[\beta^2 - \beta_0^2\right] E_g\right\} + i\gamma|E_g|^2 E_g - \frac{\alpha_S}{2} E_g + \frac{1}{2}\left[\left(\sigma_{as} + \sigma_{es}\right) N_2 - \sigma_{as} N_T\right] E_g \tag{6.8}$$

where $\beta_0 = 2\pi n_1/\lambda_S$ is the reference propagation constant, $\beta = 2\pi n(x,y)/\lambda_s$ and $n(x,y)$ is the refractive index distribution, which in the case of a GRIN fiber fulfills $n^2(x,y) = n_1^2\left(1 - 2\Delta\frac{x^2+y^2}{a^2}\right)$, where the reference index is the core refractive index n_1 and $\Delta = (n_1^2 - n_2^2)/2n_1^2$. It could be noted that equations (6.8) and (6.1) are the same except introducing the population density (gain term without saturation) and writing the propagation constant in different form in equation (6.8). In equation (6.8) the term in curly brackets describes the guiding structure, the term $i\gamma|E_g|^2 E_g$ is the instantaneous Kerr nonlinearity with $\gamma = \frac{n_{2kerr}\omega}{c}$, α_s is the linear loss of the silica glass host and the last term is the gain $g(x,y,z)$ caused by the population inversion:

$$g(x,y,z) = \frac{1}{2}\left[\left(\sigma_{as} + \sigma_{es}\right) N_2(x,y,z) - \sigma_{as} N_T(x,y,z)\right] \tag{6.9}$$

It is worth observing that even if Kerr coefficient and doping are homogeneous over the fiber cross section, both Kerr term and gain function depend on the transverse coordinates and can lead to an exchange of power among the modes carried by the optical fiber.

We developed our simulations around an ideal sample case whose set of parameter values are summarized for simplicity in table 6.1.

Symbol	Parameter	Value
σ_{ap}	Pump absorption cross section	$2.358 \times 10^{-24} m^2$
σ_{ep}	Pump emission cross section	$2.358 \times 10^{-24} m^2$
σ_{as}	Signal absorption cross section	$5 \times 10^{-27} m^2$
σ_{es}	Signal emission cross section	$2.89 \times 10^{-25} m^2$
λ_p	Pump wavelength	$979 nm$
λ_s	Signal wavelength	$1064 nm$
α_s	Linear absorption (signal)	$1.1 dB/m$
α_s	Linear absorption (pump)	$1.1 dB/m$
τ	Radiative lifetime	$1 ms$
N_T	Yb^{3+} concentration	$9.0 \times 10^{25} m^{-3}$
τ_{pulse}	Signal pulse duration	$500 ps$
T	Signal pulse repetition rate	$250 \mu s$
n_1	Maximum core refractive index	1.47
n_2	Cladding refractive index	1.457
a	Core radius	$26 \mu m$
A_{Cl}	Inner cladding area	$7.06 \times 10^{-8} m^2$
L	Fiber length	$4 m$
n_{2kerr}	Kerr nonlinear coefficient	$2.6 \times 10^{-20} m^2/W$
D_{FWHMI}	Signal beam diameter FWHMI	$40 \mu m$

Table 6.1: Parameters used in modelling and numerical simulations
[19]
.

Whether necessary, in some simulations the parameters are modified (example: suppression of the Kerr effect) and explained in the corresponding sections. The disorder along the propagation, which is responsible for the formation of a speckled pattern in the linear regime and also for the acceleration of the beam-cleaning process in the nonlinear regime [16], is implemented in the GRIN fiber with core radius $a = 26\ \mu$m and $\Delta = 8.8 \times 10^{-3}$.

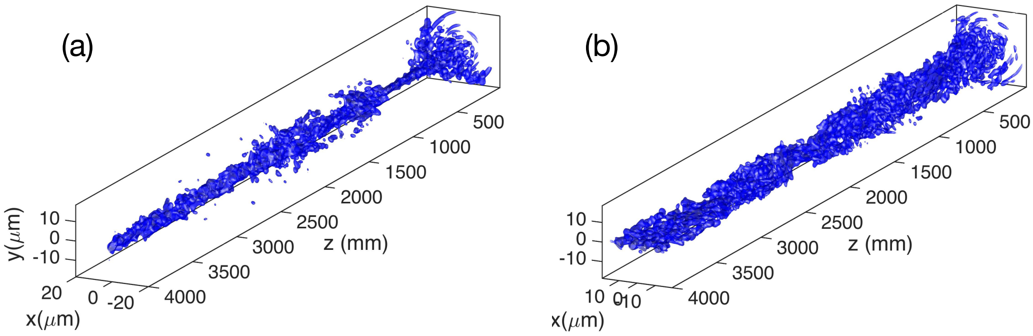

Figure 6.14: Beam cleaning in a nonlinear GRIN fiber. (a) Input signal maximum intensity $5GW/cm^2$. (b) The same as (a), but with input signal maximum intensity $0.5GW/cm^2$.

The numerical simulations confirm that the beam cleaning has a threshold power. A cleaned beam in the case of Fig. 6.14a is obtained with a maximum peak intensity $5GW/cm^2$. Whereas, with ten time less input intensity as shown in Fig. 6.14b the beam cleaning effect is substantially vanished, and it is very similar to the case of propagation in the absence of Kerr nonlinear effect (i.e. $n_{2kerr} = 0$).

We consider now the presence of a uniform doping, keeping the same linear refractive index profile. The active medium is not pumped $P_p(0) = 0$ for this particular situation. Figure 6.15 shows that it is possible to observe an effect of beam cleaning with an input signal maximum intensity of $5GW/cm^2$ (panel (a)). The effect of beam cleaning vanishes when the same simulation is carried out in the absence of Kerr effect ($n_{2kerr} = 0$). Figure 6.16 shows the modal decomposition corresponding to the case of panel (a) of figure 6.15. In particular we observe that all the modes are attenuated by the linear losses in absence of a pump able to invert the population in the active medium. The blue curve shows the power carried by the fundamental mode $\psi_{0,0}$. The red and green curves show the powers carried by the modes $\psi_{0,1}$ and $\psi_{1,0}$. The other modes $\psi_{k,h}$ are shown in grey (we considered the projections with $h, k \in [0, 9]$, a total of 100 modes).

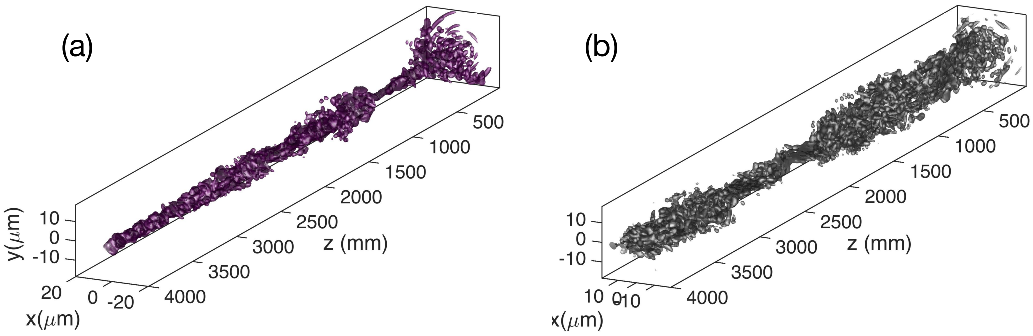

Figure 6.15: (a) Beam cleaning in a nonlinear Yb-doped GRIN fiber, in absence of pump. Input signal maximum intensity $5GW/cm^2$ (b) The same as in panel (a), but without Kerr nonlinearity $n_{2kerr} = 0$.

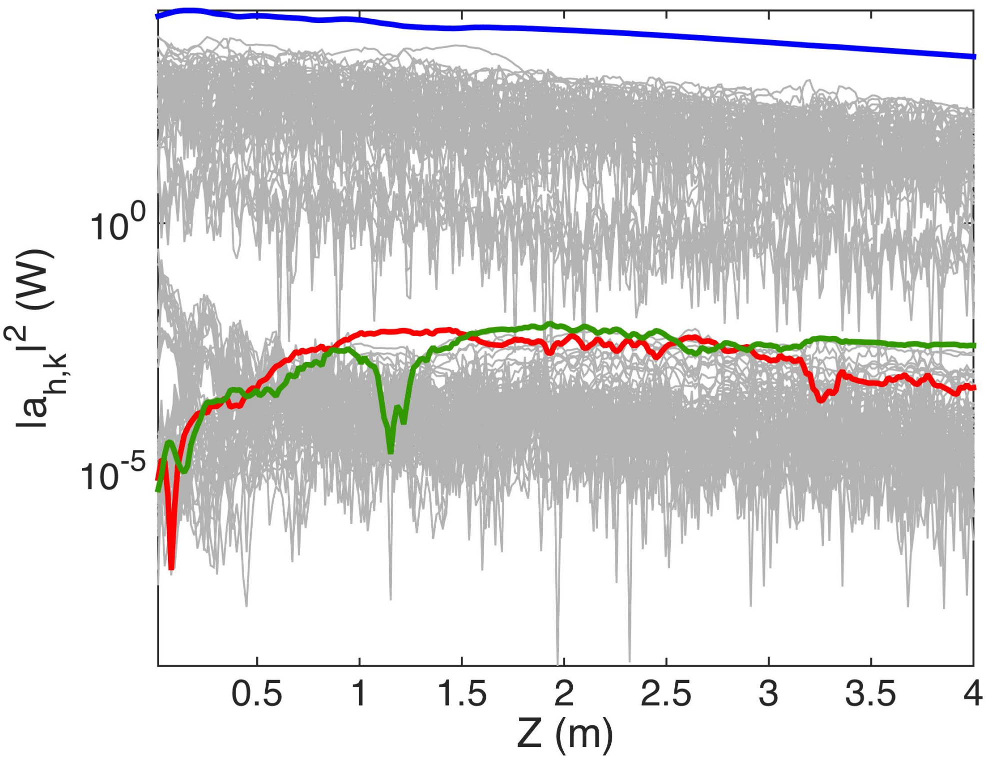

Figure 6.16: Beam cleaning in a nonlinear Yb-doped GRIN fiber in absence of pump: modal evolution. Input signal maximum intensity $5GW/cm^2$

It is also instructive to calculate the corresponding power evolutions, where $P_s(z) = \int_S |E_g(x,y,z)|^2 ds$ is the signal peak power. The nonlinear effect takes place substantially before the signal is attenuated along the propagation.

It is then interesting to observe the beam dynamics when the pump is switched on. The iso-intensity levels are shown in Fig. 6.17: in particular it is possible to observe that with a pump of 20 W, beam-cleaning is obtained with a signal of maximum intensity $0.5GW/cm^2$. Note that with such input signal level was not possible to see beam cleaning in a passive GRIN fiber (see panel (b) of Fig. 6.14). We can confirm numerically the tendency observed in the experiments reported in [46], where the beam cleaning threshold power reduces in an active fiber, owing to the signal amplification along the propagation.

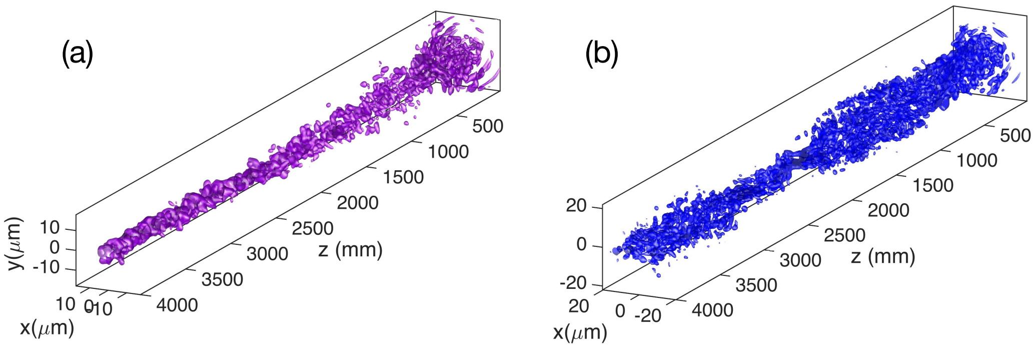

Figure 6.17: (a) Beam cleaning in a nonlinear Yb-doped GRIN fiber. Forward pump of 20W; input signal maximum intensity $0.5GW/cm^2$ (b) The same as in panel (a), but without Kerr nonlinearity $n_{2kerr} = 0$.

The gain g experienced by the complex electric field E_g is neither uniform along the fiber (owing to the progressive pump absorption), nor uniform in the transverse domain, owing to the different population inversion. In particular the effect of gain saturation is more concentrated at the point of minimum waist for the signal beam. The periodic evolution of the beam in a parabolic refractive index profile causes then a periodic fluctuation of the signal intensity and in turn this fact causes a periodic evolution of the inverted fraction $N_2(x, y, z)$ along the coordinate z. To show this effect we present the evolution of $g(x = 0, y = 0, z)$ as defined in equation (6.9), in figure 6.18. The inset shows a detail of the evolution over a shorter scale highlighted by the blue bar.

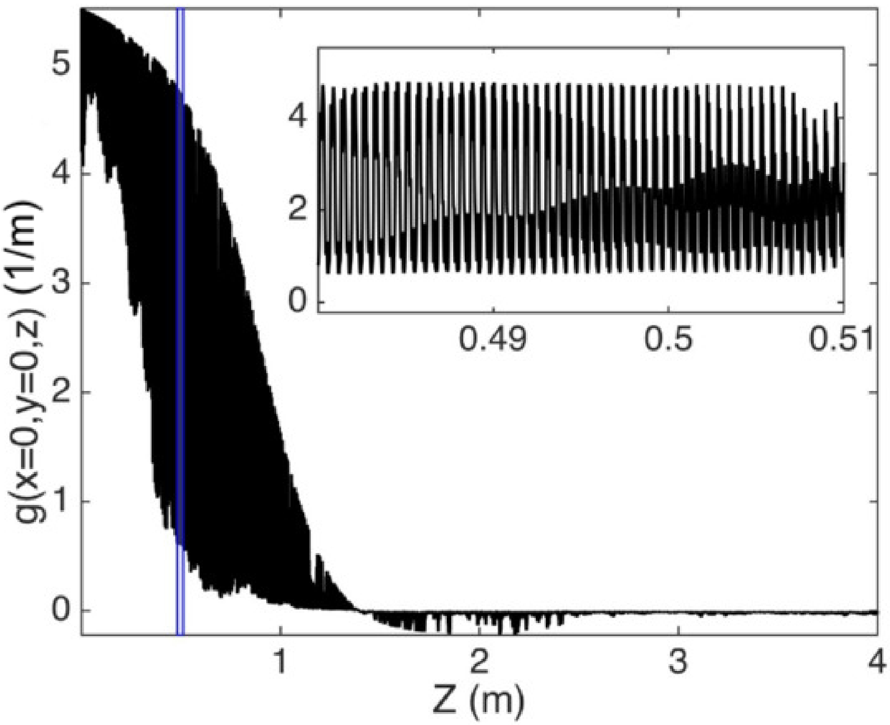

Figure 6.18: Signal gain evolution a nonlinear Yb-doped GRIN fiber. Forward pump of 20W; input signal maximum intensity $0.5 GW/cm^2$

In particular it is possible to observe how the maximum of gain is experienced at the beginning of the propagation and how the gain gradually drops as the pump is absorbed during the propagation. However the evolution is caracterized by a fast varying contribution of submillimetric scale, related to the coherent beating of all the modes.

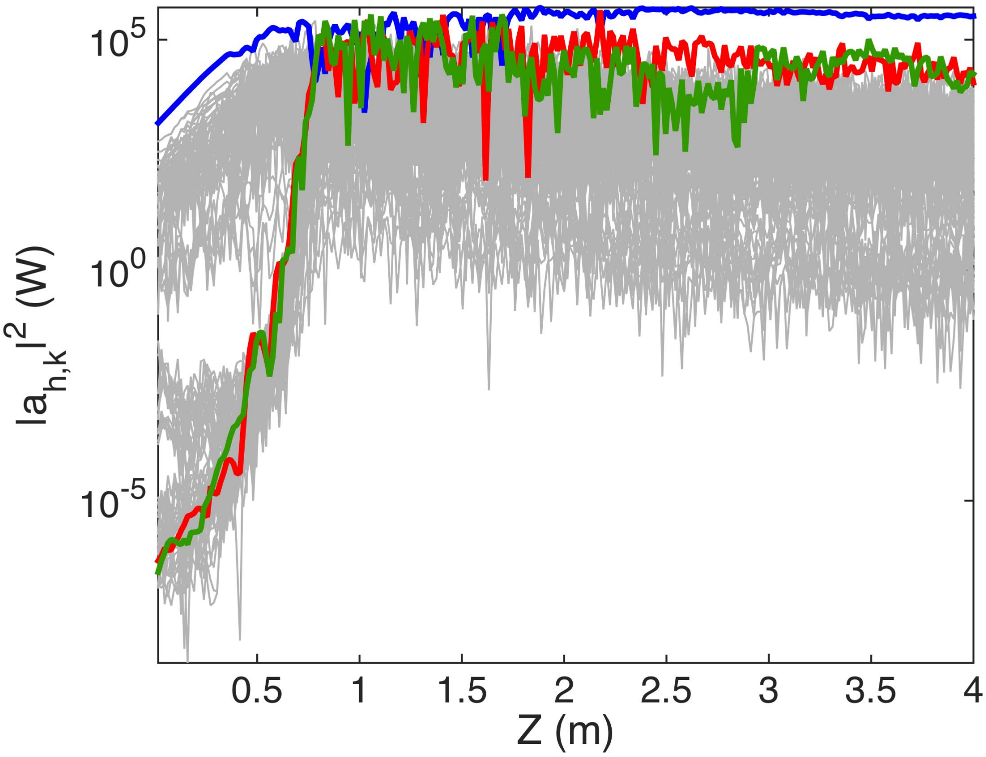

Figure 6.19: Beam cleaning in a nonlinear Yb-doped GRIN fiber: modal evolution. Forward pump of 20W; input signal maximum intensity $0.5GW/cm^2$

It is interesting to observe the evolution of the powers carried by the different modes (see Fig. 6.19). In particular it is possible to observe how all the modes are amplified and how the amplification is not uniformly distributed among the modes. This process culminates in a strong nonlinear shaping nearby z=1 m. After the power carried by the modes vary less than before being at the end nearly constant.

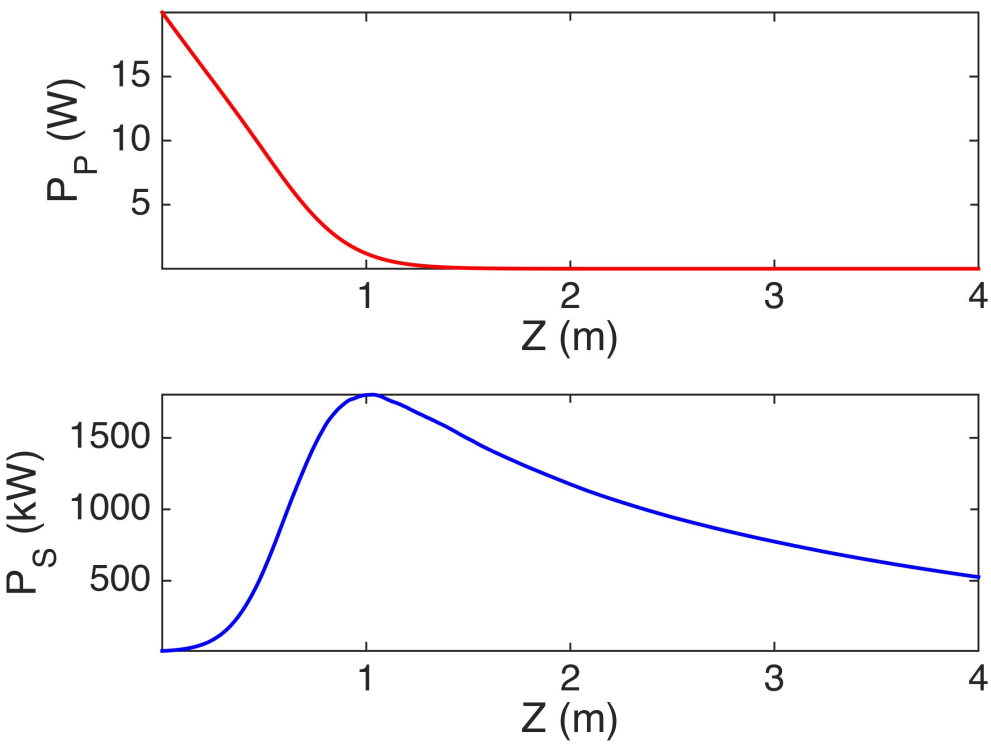

Figure 6.20: Powers of pump and signal evolution along the fiber

The situation can be possibly clarified by inspecting the evolution of powers as reported in figure 6.20. The strong nonlinear reshaping at z=1 m corresponds to the maximum amplification of the signal (here above 1.5MW in peak power). At that distance the pump is entirely absorbed and the remaining part of the propagation reduces the signal power.

6.7 Multimode Active Tapers

Fiber tapers are currently used in amplifiers so it is important to study the nonlinear beam dynamics in optical fibers whose radius $a(z)$ varies significantly along the course of the propagation direction z. Equation (6.1) can be easily extended to tapers, where the radius a(z) varies from a value a_{in} (radius at the beginning side of the taper) to a value a_{out} (taper radius at the end) . For the sake of simplicity we will model the evolution of the core radius by a linear function $a(z) = a_{out} + (z - L)(a_{out} - a_{in})/L$, where L is the taper length. In practical implementations of fiber tapers, the variation upon distance of the core radius is not necessarily linear. We refer here to the case $a_{in} > a_{out}$ (the taper has larger core radius at z=0) so to try to reproduce, in a qualitative way, some of the experimental results reported in [46]. The decrease of core radius upon fiber length causes an acceleration of the nonlinear process along the propagation. Here we considered the pump power is combined with the signal in the forward direction, that is both pump and signal powers are propagating in forward direction. In order to establish a comparative analysis with simulations in constant core radius, we have considered the same set of parameter values used for the case of homogeneous fibers. In order to match some of the features of the taper of [46], we have considered $a_{in} = 61\mu m, a_{out} = 18\mu m$. The cladding radius linearly varies from 350 μm down to 90 μm, the taper length has been extended to L = 9m. Figure 6.21a summarizes the numerical propagation with an input diode pump of 20W in the absence of Kerr effect ($n_{2kerr} = 0$), and the output beam presents a speckled patterns. On the other way, when we add the contribution of the Kerr nonlinear effect the result is qualitatively different, as shown in figure 6.21b; in particular it is possible to see how the beam pattern at the output presents a large spot in the center surrounded by a weak background. In other words, the speckled beam in the absence of Kerr is reshaped and a beam self-cleaning is obtained by introducing Kerr nonlinear effect. Note that in this situation the pump is absorbed in the first meter of propagation and that the signal is later reabsorbed along the propagation. The grey circles represent the local size of the fiber core.

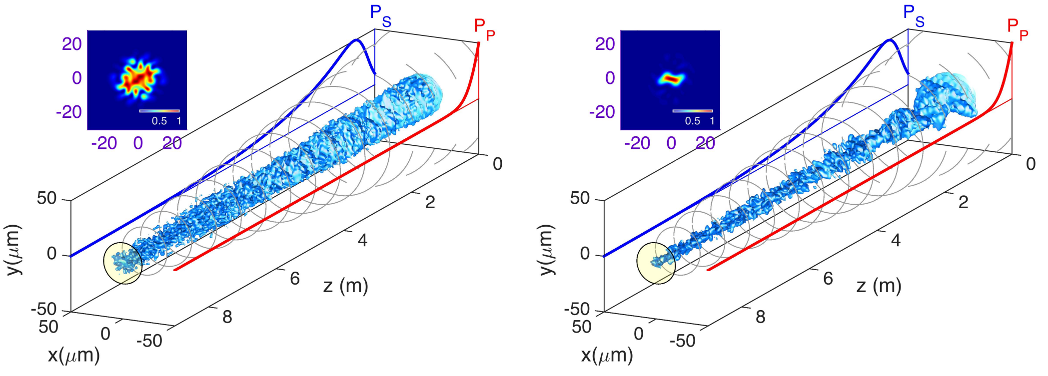

(a) **(b)**

Figure 6.21: Signal power propagation in multimode tapered fiber: (a) Iso-intensity surface at half width of maximum intensity in a Yb-doped active taper fiber in the absence of Kerr effect ($n_{2kerr} = 0$). The blue (red) curve reproduces the qualitative evolution of the signal (pump) power. The grey circles show the local size of the fiber core. The inset shows the output beam pattern. (b) The same as in figure 6.21a, but here in the presence of Kerr nonlinear effect ($n_{2kerr} \neq 0$)

To further strengthen our numerical simulation results on active tapered multimode fibers (Fig. 6.22), we made a comparison with experimental results (Fig. 6.23) which is reported in [46]. Fig. 6.22 shows numerical simulation results of signal power propagation along a 9m tapered multimode fiber by increasing the pump power of wavelength 979 nm from 1W to 31W. The pump and signal powers are configured in co- propagating scheme. With a weak pumping (a) the input signal cannot reach the beam cleaning and the output beam is clearly speckled. Upon increase of the input forward pump, the signal is amplified till the point that the nonlinearity can modify the beam shape. The iso-intensity surface at 50% of the maximum intensity exhibits a gradual contraction upon increase of the input pump power. Notably in panel (c) it is possible to observe a local split of the beam in two lobes. This represents a transient effect and tend to vanish upon further increase of the pump power till the formation of bell shaped beam shown in panel (d). In figure 6.22 the input signal peak power is $P_S(0) = 3.6\,\text{kW}$ for all cases, and the output peak power in each panels are: (a) $P_S(L) = 6.3\,\text{W}$, (b) $P_S(L) = 0.026\,\text{kW}$, (c) $P_S(L) = 0.05\,\text{kW}$, (d) $P_S(L) = 0.2\,\text{kW}$.

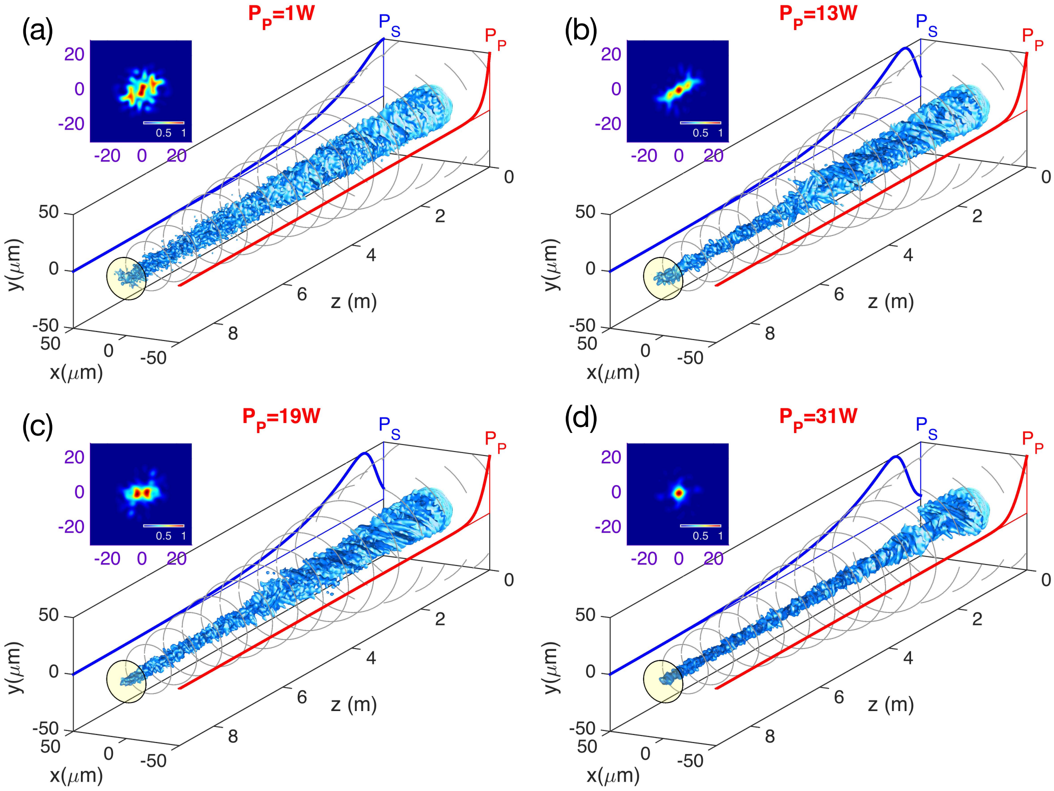

Figure 6.22: Numerical simulation shows signal power propagation for different input pump powers, input signal maximum intensity is 0.2 GW/cm^2, and diameter of 40μm FWHMI: (a) 1 W (b) 13 W (c) 19 W (d) 31 W

For experimental comparison we considered a laboratory activity performed on active tapered multimode fiber and which is described in [46]. In this experiment the beam self-cleaning is investigated by switching on and off the CW laser diode pump source. First, as shown in Fig. 6.23(a) the pump power is switched off. The transverse content of light at the taper output involved a superposition of the fundamental and higher-order modes in this situation, and the speckled beam is visualized at the output end. Next, the laser diode pump is switched on, and gradually increased its power, thus adding a growing amount of gain (G) to the fiber. The gain indicated in Fig. 6.23 corresponds to the ratio between the measured output and input average power of the signal. From Figs. 6.23(b) – 6.23(e), a progressive reshaping of the guided input beam profile into a cleaned beam can be observed. The beam self-cleaning started to form for G = 0.21, and it remained preserved up to G = 1.34, which is the maximum net gain. The limited net gain G is due to pump absorption taking place beyond the first meters of taper, where the laser diode pump has been fully depleted. It should be noted that, these observations clearly shows the signal amplification due to the variation of gain along the active multimode tapered fiber leads to the spatial beam self-cleaning. To recap, the results of both experimental and numerical simulations confirms that, by increasing the pump power or gain, reshaping of the transverse spatial beam pattern at the tapered multimode fiber output is obtained. On the contrary, at lower pump power, the randomly excited fiber modes would lead to a highly speckled or irregular intensity patterns at the fiber output end.

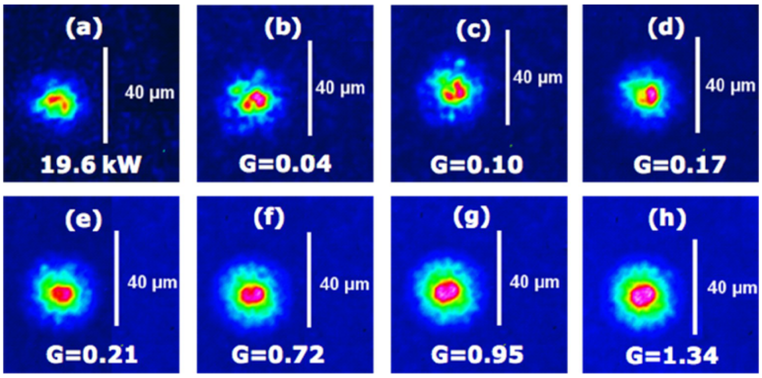

Figure 6.23: Experimental result shows beam reshaping obtained by increasing the gain [46].

Another experimental result reported in [46] [45], discusses the spatial beam self-cleaning with decelerating nonlinearity, that is, by moving from the smaller to larger multimode tapered fiber end. The Kerr nonlinear effect decelerates with increasing mode area as the input signal laser propagates from the smaller core radius size to larger end. In this experiment continuous wave laser diode pump of 10W output power with counter-propagating pump scheme, and uniform core doping profile is considered, but in our numerical simulation the pumping is in forward direction. The main effect of changing the pumping scheme is that of varying the gain, but for a sufficiently high gain (pump power) it is always possible to observe beam reshaping. Figure 6.24 shows the beam self-cleaning phenomenon as a function of input peak power. The input peak power varied progressively from 280W to 51kW, and the beam intensity profile shows distorted output at lower input peak power. When the input power is increased above 20 kW, the output beam spatial pattern self-organises into a bright spot with a bell shape, surrounded by a low-power background, which is a typical manifestation of spatial beam self-cleaning.

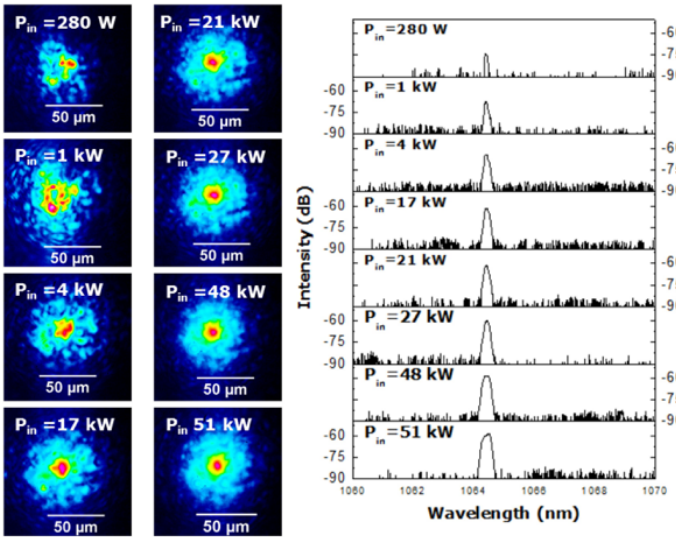

Figure 6.24: Left panel: Near-field spatial field distributions at different input peak powers (P_{in}) for a tapered multimode fiber. [46].

6.8 Chapter Summary

In chapter 5 we have studied the mode coupling inside graded index multimode fiber due to gain and Kerr nonlinear effects using coupled mode equation. In this chapter 3D NLSE is implemented to study modal power propagation and beam cleaning, by considering effects such as disorder, Kerr and gain saturation. Comparison between coupled mode equation and 3D NLSE is also made under the same conditions. Kerr beam self-cleaning phenomenon is analysed and investigated in depth, first we neglected the effects of disorder as its shown in figures 6.6 and 6.7. We then moved on re-introducing the effects of disorder, saturated gain and Kerr by increasing the input power. The beam self-cleaning is then examined by determining the beam width at different power levels, and found out the beam width is reduced when the beam self-cleaning takes place.

Furthermore, we also coupled the population density from the rare-earth dopants into the 3D NLSE to study the beam self-cleaning with different pump configurations. We extended the beam self-cleaning phenomenon in multimode active tapered fiber using the same modelling equation that is, 3D NLSE. Besides, by analysing numerical simulation results, and experimental values, we found out the same trend of beam cleaning phenomenon.

Chapter 7

Conclusion and Future Work

7.1 Conclusion

In this research thesis we have studied nonlinear propagation in graded-index multimode fiber amplifiers. The physics of the rare-earth doped multimode fiber devices has been explored thoroughly and their properties have been investigated in depth. Single-mode high beam quality performance is achieved by exploiting Kerr nonlinearty in active multimode fibers, which is crucial for high power fiber amplifiers and fiber laser production. The high beam quality obtained from multimode fiber is very essential in many applications such as biological imaging, LIDAR (Light Detection and Ranging, that is detection and estimation of distance by light), spectroscopy, microspectroscopy and others.

Self-imaging a property in graded-index multimode fiber which is the exact reproduction of input electromagnetic field at certain distance due to multimodal interference was investigated in the second chapter of our manuscript. Theoretically we studied self-imaging phenomenon by projecting input beam shape into a set of guided modes and then propagating the modes for few millimetres, using modal expansion and propagation approach. A wide and well defined Gaussian input beam causes a periodical evolution with a regular spacing of local peak intensities. If these intensity values will generate nonlinear effects (frequency conversion) a regular series of spots will appear along the fiber longitudinal axis. The distance among these spots is related to the self-imaging period. When the power is large enough to generate spatial beam distortion along the propagation and possibly close to collapse, one can imagine that the beam is no longer Gaussian and self-imaging property is broken. For this reason, it is important to use a low laser power to preserve the beam shape and hence self-imaging in graded index multimode fibers. Furthermore, we have confirmed that the self-imaging period (distance) of longitudinal spatial oscillation determined theoretically, which is related to the core diameter and relative effective index differences among modes, completely agrees with experimental results. We also evaluated the self-imaging period when the input laser beam is inclined from the normal horizontal axis, and found out that the though the beam propagates in zigzag the distance between consecutive spots (period) doesn't change.

Fiber amplifier characteristics, such as the operating wavelength and the gain bandwidth, are determined by dopants rather than by the fiber, which plays the role of a host medium. In this research thesis we have considered ytterbium-doped fiber amplifiers, mainly due to their interesting applications for broad gain bandwidth with excellent beam quality, unique simple energy level structure, high pump absorption and efficiency. In addition to the low quantum defects, and superb spectroscopic characteristics, the capability of generating high powers makes them very attractive. Ytterbium-doped materials have been widely used for high efficiency and high energy laser sources at $1\mu m$ wavelength region because of their very low quantum defect and the unique simple energy level structure. Quantum defect is the energy difference between pump and laser photons. A reduction in the quantum defect may offer significant mitigation of issues associated with fiber heating, and for scaling high-power fiber laser systems [69]. To investigate the input signal and pump power propagation in multimode fiber amplifiers, we applied rate and propagation equations, with different pumping schemes. In both forward and backward pumping schemes, the fiber amplifier is pumped from the initial and the end side of the fiber simultaneously. Furthermore, we have analysed and formulated rate equations for both core and cladding pumping in multimode fibers.

Mode coupling is on of the main occurrences in multimode fibers when each mode have the same propagation constant or effective refractive index. Propagation constants in multimode fiber locally change due to imperfections, bends, local gain, temperature or core radius variation. As a result, it can happen that the modes could have the same propagation constant at a given point and mode coupling occurs. We have studied mode coupling in multimode fibers due to non-uniform and nonlinear effects, using coupled mode equations. Modal expansion approach where the total guided optical field is expressed as the superposition of eigenmode is utilized to simplify the 3D NLSE and develop the coupled mode equation. For non-uniform gain (dopant) distributions in our numerical simulations, we considered parabolic and ring dopant profiles. As a result, our extensive numerical simulations indicates their is selective amplification of the modes in active multimode fibers with non-uniform dopant profiles. In parabolic gain distribution fundamental mode is selectively amplified, whereas the high order modes are suppressed. This is mainly because intensity profile of the fundamental mode overlaps with dopant distribution having the same profile which results in selective amplification. On the contrary, ring dopant profile enables the selective amplification of high order modes, but suppresses that of the fundamental mode. Furthermore, by increasing the input signal power we have discovered that the modes exchange energy, due to Kerr nonlinearity and transfers power to the fundamental mode. This transfer of power from high order modes to the fundamental mode enables beam cleaning in multimode fibers, which is crucial for high power fiber amplifiers and laser.

In addition to the coupled mode equation, we also investigated nonlinear propagation in active multimode fibers by applying 3D NLSE. In this situation the fiber is perturbed, in the sense that we have introduced disorder randomly along the fiber length. In addition to Kerr nonlinear effect, linear coupling, which are, gain saturation and disorders are considered. Our numerical simulation reveals that by increasing the input signal power, the speckled beam reshapes itself after certain fiber distance, into a clean beam close to single mode operation due to Kerr nonlinearity. The beam cleaning phenomenon is further confirmed by examining the beam width at the end of fiber length, which has smaller diameter than the one at the beginning of the fiber. Furthermore, we also extended the 3D NLSE for multimode active tapered fibers, to study the beam self-cleaning. The gain from the pump power is included in the 3D NLSE and beam self-cleaning in active multimode tapered fiber is thoroughly investigated.

Finally, we performed comparison between coupled mode equation and 3D NLSE under the same parameters, but this time only in the presence of Kerr nonlinearity and gain. Due to the complex process in multimode fibers,it's very essential to obtain a computationally efficient numerical modelling and simulation tools to investigate the phenomenon happening inside the core. Coupled mode equations and 3D NLSEs are two of the tools we utilized to perform numerical simulations. We found out that by using proper input beam width and number of guided modes, the two numerical modelling tools perform similarly.

7.2 Future Work

Further investigations would focus on ytterbium-erbium codoped multimode fiber amplifiers and lasers, particularly on numerical simulation tools. The coupled mode equation we explored considers non-uniform gain and Kerr nonlinearity, furthermore it could be extended by considering other factors like disorder and gain saturation. More extension on our already developed numerical simulator could be done with large number of modes, to investigate their effects in energy transfer, beam cleaning and high power fiber amplifiers and lasers production. Moreover, in coupled mode equations, modal power propagation could be studied in depth by identifying the properties of each high order modes, that is which particular modes are responsible for exchange of power towards the fundamental mode and useful for high power fiber amplifiers development. Another possible extension of this thesis work could be, investigating the computational efficiency and performance of coupled mode equations and 3D NLSE's under the same effects, that is by considering disorder and gain saturation in coupled mode equations.

It is necessary if we want to study the propagation of short pulses (as those that can be generated in a mode-locked laser) to include the time domain propagation equations in addition to the spatial domain we explored in depth. For these and related investigations our analysis has to be expanded to include the time domain.

References

[1] KS Abedin et al. “Cladding-pumped erbium-doped multicore fiber amplifier”. In: *Optics express* 20.18 (2012), pp. 20191–20200.

[2] Govind P Agrawal. *Applications of nonlinear fiber optics*. Elsevier, 2001.

[3] Govind P Agrawal. *Fiber-optic communication systems*. Vol. 222. John Wiley & Sons, 2012.

[4] Govind P Agrawal. “Invite paper: Self-imaging in multimode graded-index fibers and its impact on the nonlinear phenomena”. In: *Optical Fiber Technology* 50 (2019), pp. 309–316.

[5] Amira S Ahsan and Govind P Agrawal. “Effect of an input beam’s shape and curvature on the nonlinear effects in graded-index fibers”. In: *JOSA B* 37.3 (2020), pp. 858–867.

[6] P Aschieri et al. “Condensation and thermalization of classsical optical waves in a waveguide”. In: *Physical Review A* 83.3 (2011), p. 033838.

[7] Neng Bai et al. “JL nares, C. Montero, V. Moreno, X. Prieto, V. Tse, KM Chung, APT Lau, H”. In: *Y. Tam, C. Lu, Y. Luo, G.-D. Peng, G. Li, and T. Wang, Opt. Express* 20 (2012), pp. 2668–2680.

[8] Neng Bai et al. “Multimode fiber amplifier with tunable modal gain using a reconfigurable multimode pump”. In: *Optics express* 19.17 (2011), pp. 16601–16611.

[9] Philippe M Becker, Anders A Olsson, and Jay R Simpson. *Erbium-doped fiber amplifiers: fundamentals and technology*. Elsevier, 1999.

[10] S Berdagué and P Facq. “Mode division multiplexing in optical fibers”. In: *Applied optics* 21.11 (1982), pp. 1950–1955.

[11] Mitchell A Cox et al. “The resilience of Hermite–and Laguerre–Gaussian modes in turbulence”. In: *Journal of Lightwave Technology* 37.16 (2019), pp. 3911–3917.

[12] Maryam Eilchi and Parviz Parvin. “Gain saturation in optical fiber laser amplifiers”. In: *Fiber Laser*. InTech, 2016, pp. 297–320.

[13] Andrew D Ellis, Jian Zhao, and David Cotter. “Approaching the non-linear Shannon limit”. In: *Journal of Lightwave Technology* 28.4 (2009), pp. 423–433.

[14] René-Jean Essiambre et al. “Capacity limits of optical fiber networks”. In: *Journal of Lightwave Technology* 28.4 (2010), pp. 662–701.

[15] RJ Essiambre et al. “Space-division multiplexing in multimode and multi-core fibers for high-capacity optical communications”. In: *IEEE Photonics J* 5.2 (2013), p. 071307.

[16] Adrien Fusaro et al. “Dramatic acceleration of wave condensation mediated by disorder in multimode fibers”. In: *Physical Review Letters* 122.12 (2019), p. 123902.

[17] MD Gervaziev et al. “Mode decomposition of multimode optical fiber beams by phase-only spatial light modulator”. In: *Laser Physics Letters* 18.1 (2020), p. 015101.

[18] AJOY AUTOR GHATAK et al. *An introduction to fiber optics*. Cambridge university press, 1998.

[19] Mali Gong et al. "Numerical modeling of transverse mode competition in strongly pumped multimode fiber lasers and amplifiers". In: *Optics Express* 15.6 (2007), pp. 3236–3246.

[20] François Gonthier et al. "Mode coupling in nonuniform fibers: comparison between coupled-mode theory and finite-difference beam-propagation method simulations". In: *JOSA B* 8.2 (1991), pp. 416–421.

[21] DC Hanna et al. "Continuous-wave oscillation of a monomode ytterbium-doped fibre laser". In: *Electronics Letters* 24.17 (1988), pp. 1111–1113.

[22] Tobias Hansson et al. "Nonlinear beam self-imaging and self-focusing dynamics in a GRIN multimode optical fiber: theory and experiments". In: *arXiv preprint arXiv:2005.07280* (2020).

[23] Cesar Jauregui et al. "Optimizing high-power Yb-doped fiber amplifier systems in the presence of transverse mode instabilities". In: *Optics express* 24.8 (2016), pp. 7879–7892.

[24] Hai Ming Jiang and Kang Xie. "Efficient and robust shooting algorithm for numerical design of bidirectionally pumped Raman fiber amplifiers". In: *JOSA B* 29.1 (2012), pp. 8–14.

[25] Z Jiang and JR Marciante. "Impact of transverse spatial-hole burning on beam quality in large-mode-area Yb-doped fibers". In: *JOSA B* 25.2 (2008), pp. 247–254.

[26] William K Johnston III. "The birth of fiberoptics from" light guiding"". In: *Journal of endourology* 18.5 (2004), pp. 425–426.

[27] Joseph M Kahn, Keang-Po Ho, and Mahdieh Bagher Shemirani. "Mode coupling effects in multi-mode fibers". In: *Optical Fiber Communication Conference*. Optical Society of America. 2012, OW3D–3.

[28] Qiongyue Kang et al. "Accurate modal gain control in a multimode erbium doped fiber amplifier incorporating ring doping and a simple LP 01 pump configuration". In: *Optics Express* 20.19 (2012), pp. 20835–20843.

[29] Ido Kelson and Amos A Hardy. "Strongly pumped fiber lasers". In: *IEEE Journal of Quantum Electronics* 34.9 (1998), pp. 1570–1577.

[30] Denis S Kharenko et al. "Mode decomposition of Kerr self-cleaned beams by phase only SLM". In: *Real-time Measurements, Rogue Phenomena, and Single-Shot Applications VI*. Vol. 11671. International Society for Optics and Photonics. 2021, p. 1167105.

[31] Peter M Krummrich. "Spatial multiplexing for high capacity transport". In: *Optical Fiber Technology* 17.5 (2011), pp. 480–489.

[32] Katarzyna Krupa et al. "Multimode nonlinear fiber optics, a spatiotemporal avenue". In: *APL Photonics* 4.11 (2019), p. 110901.

[33] Katarzyna Krupa et al. "Spatial beam self-cleaning in multimode fibres". In: *Nature Photonics* 11.4 (2017), pp. 237–241.

[34] Jesper Lægaard. "Multimode nonlinear simulation technique having near-linear scaling with mode number in circular symmetric waveguides". In: *Optics Letters* 45.15 (2020), pp. 4160–4163.

[35] Jesper Lægsgaard et al. "Static and dynamic mode instabilities in dual-core fiber amplifiers". In: *JOSA B* 36.3 (2019), pp. 757–767.

[36] Jinglin Liu et al. "An improved shooting algorithm and its application to high-power fiber lasers". In: *Optics communications* 283.19 (2010), pp. 3764–3767.

[37] Stefano Longhi. "Modulational instability and space time dynamics in nonlinear parabolic-index optical fibers". In: *Optics letters* 28.23 (2003), pp. 2363–2365.

[38] Haibin Lü et al. "General analysis of the mode interaction in multimode active fiber". In: *Optics express* 20.6 (2012), pp. 6456–6471.

[39] K Lu and Niloy K Dutta. "Spectroscopic properties of Yb-doped silica glass". In: *Journal of applied physics* 91.2 (2002), pp. 576–581.

[40] Arash Mafi. "Pulse propagation in a short nonlinear graded-index multimode optical fiber". In: *Journal of Lightwave Technology* 30.17 (2012), pp. 2803–2811.

[41] Jamal T Manassah, Patrice L Baldeck, and RR Alfano. "Self-focusing and self-phase modulation in a parabolic graded-index optical fiber". In: *Optics letters* 13.7 (1988), pp. 589–591.

[42] Dean E McCumber. "Theory of phonon-terminated optical masers". In: *Physical review* 134.2A (1964), A299.

[43] Mohammad-Ali Miri, Patrik LiKamWa, and Demetrios N Christodoulides. "Large area single-mode parity–time-symmetric laser amplifiers". In: *Optics letters* 37.5 (2012), pp. 764–766.

[44] Elham Nazemosadat and Arash Mafi. "Nonlinear multimodal interference and saturable absorption using a short graded-index multimode optical fiber". In: *JOSA B* 30.5 (2013), pp. 1357–1367.

[45] A Niang et al. "Nonlinear beam cleanup in Yb-doped GRIN multimode fiber taper". In: *Nonlinear Photonics*. Optical Society of America. 2020, NpTh3D–5.

[46] A Niang et al. "Spatial beam self-cleaning and supercontinuum generation with Yb-doped multimode graded-index fiber taper based on accelerating self-imaging and dissipative landscape". In: *Optics express* 27.17 (2019), pp. 24018–24028.

[47] Alioune Niang et al. "Self-cleaning on a higher order mode in Ytterbium-doped multimode fiber with parabolic profile". In: *2019 Conference on Lasers and Electro-Optics (CLEO)*. IEEE. 2019, pp. 1–2.

[48] Rudiger Paschotta et al. "Ytterbium-doped fiber amplifiers". In: *IEEE Journal of quantum electronics* 33.7 (1997), pp. 1049–1056.

[49] Mostafa Peysokhan, Esmaeil Mobini, and Arash Mafi. "Analytical formulation of high-power Yb-doped double-cladding fiber laser". In: *arXiv preprint arXiv:2002.10403* (2020).

[50] Francesco Poletti and Peter Horak. "Description of ultrashort pulse propagation in multimode optical fibers". In: *JOSA B* 25.10 (2008), pp. 1645–1654.

[51] Richard S Quimby et al. "Yb^{3+} Ring Doping in High-Order-Mode Fiber for High-Power 977-nm Lasers and Amplifiers". In: *IEEE Journal of Selected Topics in Quantum Electronics* 15.1 (2009), pp. 12–19.

[52] DJ Richardson, JM Fini, and Lynn E Nelson. "Space-division multiplexing in optical fibres". In: *Nature Photonics* 7.5 (2013), p. 354.

[53] Lorenzo Rosa et al. “Thermal modeling of gain competition in Yb-doped large-mode-area photonic-crystal fiber amplifier”. In: *Optics express* 23.14 (2015), pp. 18638–18644.

[54] Antoine FJ Runge et al. “All-normal dispersion fiber lasers mode-locked with a nonlinear amplifying loop mirror”. In: *Optical Fiber Technology* 20.6 (2014), pp. 657–665.

[55] Kiminori Sato et al. “Optimized graded index two-mode optical fiber with low DMD, large A eff and low bending loss”. In: *Optics express* 21.14 (2013), pp. 16231–16238.

[56] Stefano Selleri, Luca Vincetti, and Annamaria Cucinotta. *Optical and phOtOnic cOmpOnents*. Società Editrice Esculapio, 2015.

[57] Claude E Shannon. “A mathematical theory of communication”. In: *Bell system technical journal* 27.3 (1948), pp. 379–423.

[58] Mahdieh B Shemirani et al. “Principal modes in graded-index multimode fiber in presence of spatial-and polarization-mode coupling”. In: *Journal of lightwave technology* 27.10 (2009), pp. 1248–1261.

[59] Chen Shi et al. “Theoretical study of mode evolution in active long tapered multimode fiber”. In: *Optics express* 24.17 (2016), pp. 19473–19490.

[60] Oleg S Sidelnikov et al. “Random mode coupling assists Kerr beam self-cleaning in a graded-index multimode optical fiber”. In: *Optical Fiber Technology* 53 (2019), p. 101994.

[61] Tom Sperber et al. “Wavefront Shaping of the Pump in Multimode Fiber Amplifiers; The Gain-Dependent Transmission Matrix”. In: *arXiv preprint arXiv:1911.07812* (2019).

[62] Slawomir Sujecki et al. “Comparative modeling of infrared fiber lasers”. In: *Photonics*. Vol. 5. 4. Multidisciplinary Digital Publishing Institute. 2018, p. 48.

[63] Robert W Tkach. “Scaling optical communications for the next decade and beyond”. In: *Bell Labs Technical Journal* 14.4 (2010), pp. 3–9.

[64] Jean-Baptiste Trinel et al. “Theoretical study of gain-induced mode coupling and mode beating in few-mode optical fiber amplifiers”. In: *Optics express* 25.3 (2017), pp. 2377–2390.

[65] Logan G Wright et al. “Multimode nonlinear fiber optics: massively parallel numerical solver, tutorial, and outlook”. In: *IEEE Journal of Selected Topics in Quantum Electronics* 24.3 (2017), pp. 1–16.

[66] Logan G Wright et al. “Self-organized instability in graded-index multimode fibres”. In: *Nature Photonics* 10.12 (2016), pp. 771–776.

[67] Jingwei Wu et al. “Investigation of ion-ion interaction effects on Yb 3+-doped fiber amplifiers”. In: *Optics Express* 27.20 (2019), pp. 28179–28193.

[68] Wen Xiong et al. “Spatiotemporal control of light transmission through a multimode fiber (Conference Presentation)”. In: *Adaptive Optics and Wavefront Control for Biological Systems III*. Vol. 10073. International Society for Optics and Photonics. 2017, p. 1007312.

[69] N Yu et al. “Less than 1% quantum defect fiber lasers via ytterbium-doped multicomponent fluorosilicate optical fiber”. In: *Optics letters* 43.13 (2018), pp. 3096–3099.

[70] Xin Zhong et al. "Influence of finite apertures on orthogonality and completeness of Laguerre-Gaussian beams". In: *IEEE Access* 6 (2018), pp. 8742–8754.

[71] Xiushan Zhu et al. "Detailed investigation of self-imaging in largecore multimode optical fibers for application in fiber lasers and amplifiers". In: *Optics Express* 16.21 (2008), pp. 16632–16645.

Appendix A: List of Publications

M.A. Jima, E. Deliancourt, R. Jauberteau, Y. Leventoux, A. Niang, K. Krupa, T. Mansuryan, M. Fabert, S. Février, A. Tonello, D. Modotto, O. Sidelnikov, S. Wabnitz, A. Barthélémy, V. Kermene, A. Desfarges-Berthelemot, G. Millot, and V. Couderc, "Spatial Beam Evolution in Nonlinear Multimode Fibers," accepted to CLEO: Laser Science to Photonic Applications, San Jose, California United States, 9–14 May 2021.

A.Niang, **M.A.Jima**, D.Modotto, F.Mangini, A.Tonello,U.Minoni,M.Fabert,M.Zitelli, V.Couderc, S.Wabnitz, ”Spatial beam nonlinear control with multimode GRIN fiber amplifiers”, International Society for Optics and Photonics, vol. 11665, pages. 116650L, March 2021.

Patent, “Multimode waveguide configured to generate single-mode radiation from single-mode radiation”, N/Réf.: PAT2604021FR00 / CILAS49 / DAPA /BEHA, fr No. 2012649 of 03 December 2020.

Alioune Niang, Vincent Couderc, Alessandro Tonello, Katarzyna Krupa, **Mesay Addisu Jima**, Raphaël Jauberteau, Marc Fabert, Daniele Modotto, and Stefan Wabnitz, “Self-Cleaning on a Higher Order Mode in Ytterbium-Doped Multimode Fiber with Parabolic Profile,” CLEO: Science and Innovations 2019, San Jose, California United States 5–10 May 2019, p. STh4L.1.

A. Niang, D. Modotto, A. Tonello, F. Mangini, U. Minoni, M. Zitelli, M. Fabert, **M. Jima**, O. Egorova, A. Levchenko, S. Semjonov, D. Lipatov, S. Babin, V. Couderc, and S. Wabnitz, “Nonlinear beam cleanup in Yb-doped GRIN multimode fiber taper,” OSA Advanced Photonics Congress (AP) 2020 (IPR, NP, NOMA, Networks, PVLED, PSC, SPPCom, SOF), paper NpTh3D.5.

A. Niang, D. Modotto, A. Tonello, F. Mangini, U. Minoni, M. Fabert, **M. Jima**, O. Egorova, A. Levchenko, S. Semjonov, D. Lipatov, V. Couderc, and S. Wabnitz, “Beam self-cleaning in tapered Ytterbium-doped multimode fiber with decelerating nonlinearity,” Conference on Lasers and Electro-Optics, OSA Technical Digest (Optical Society of America, 2020), paper SM4P.3.

Alioune Niang, Daniele Modotto, Alessandro Tonello, Fabio Mangini, Umberto Minoni, Mario Zitelli, Marc Fabert, **Mesay Addisu Jima**, ON Egorova, Andrey E Levchenko, et al. “Spatial beam self-cleaning in tapered Yb-doped GRIN multimode fiber with decelerating nonlinearity,” IEEE Photonics Journal, vol. 12, no. 2, pp. 1-8, April 2020.